



저작자표시-비영리-동일조건변경허락 2.0 대한민국

이용자는 아래의 조건을 따르는 경우에 한하여 자유롭게

- 이 저작물을 복제, 배포, 전송, 전시, 공연 및 방송할 수 있습니다.
- 이차적 저작물을 작성할 수 있습니다.

다음과 같은 조건을 따라야 합니다:



저작자표시. 귀하는 원저작자를 표시하여야 합니다.



비영리. 귀하는 이 저작물을 영리 목적으로 이용할 수 없습니다.



동일조건변경허락. 귀하가 이 저작물을 개작, 변형 또는 가공했을 경우에는, 이 저작물과 동일한 이용허락조건하에서만 배포할 수 있습니다.

- 귀하는, 이 저작물의 재이용이나 배포의 경우, 이 저작물에 적용된 이용허락조건을 명확하게 나타내어야 합니다.
- 저작권자로부터 별도의 허가를 받으면 이러한 조건들은 적용되지 않습니다.

저작권법에 따른 이용자의 권리는 위의 내용에 의하여 영향을 받지 않습니다.

이것은 [이용허락규약\(Legal Code\)](#)을 이해하기 쉽게 요약한 것입니다.

[Disclaimer](#)

공학박사학위논문

고 효율 극초음속 풍동 디퓨저에 대한
대체 모델 기반의 민감도 분석 및 설계연구

Surrogate Model based Sensitivity Analysis and Design Study for
High Efficiency Hypersonic Wind Tunnel Diffuser

2023 년 2 월

서울대학교 대학원

항공우주공학과

최 대 산

고 효율 극초음속 풍동 디퓨저에 대한 대체 모델 기반의 민감도 분석 및 설계연구

Surrogate Model based Sensitivity Analysis and Design Study for
High Efficiency Hypersonic Wind Tunnel Diffuser

지도교수 김 규 홍

이 논문을 공학박사 학위논문으로 제출함

2023 년 2 월

서울대학교 대학원

항공우주공학과

최 대 산

최대산의 공학박사 학위논문을 인준함

2023 년 2 월

위 원 장 : ____이__관__중____

부위원장 : ____김__규__홍____

위 원 : ____이__복__직____

위 원 : ____도__형__록____

위 원 : ____나__재__정____

Abstract

The operation of hypersonic wind tunnel (HWT) requires an excessive pressure ratio owing to the excess total pressure loss in the hypersonic environment. Therefore, designing a diffuser that can alleviate this total pressure loss by compressing the hypersonic flow efficiently is essential.

However, research on the design of the HWT diffuser cannot be considered to have been sufficiently conducted, and the disclosure of the research have been limited. Conventional diffuser design methodologies use simplified analysis or rule of thumb, and in most cases, when designing a diffuser, simply referencing the existing diffuser shapes, or relying highly on the researcher's know-how and insights. It can be said that the HWT diffuser derived in this way has a high risk of having too low efficiency or being inoperable.

This study aimed to design an efficient HWT diffuser that enables HWT testing with a large blockage model with limited resources. The conventional consensus required a larger HWT for the test of the large blockage model, which will cause an exponential increase in cost. Therefore, through comprehensive diffuser design research, it was possible to design the diffuser shape that can test the large blockage model. Additionally, the study minimized the cost of constructing and operating a HWT by maximizing the diffuser efficiency.

The efficient HWT diffuser was designed by using a design method that was more sophisticated than the conventional inefficient and high-risk design method. First, the fundamental characteristics of the HWT were analyzed through numerical analysis, and an innovative observation value helpful for effective diffuser design were proposed. After that, a parametric study based design study was conducted. The effect of each design variable on the diffuser efficiency was investigated, and a HWT diffuser that could be

operable even in the presence of a test model with a large blockage ratio was designed.

However, the parametric study based design method is inefficient in terms of time and resource because parametric studies must be repeatedly performed until the design requirements is fulfilled. Therefore, surrogate model based design study was conducted to resolve this inefficiency. First, a framework was established to analyze the diffuser design space systematically and efficiently. The framework consists of a DOE based analysis point sampler, an automated flow analysis and diffuser efficiency evaluation module, a kriging surrogate model generation module, and a sensitivity analysis module. Using this framework, the surrogate models were constructed and the entire design space of the HWT diffuser was quantitatively investigated via sensitivity analysis.

Using the surrogate models, the HWT diffuser shape with higher efficiency than the parametric design method was effectively derived. In addition, considering the on-design condition of Mach 7 flow condition and off-design condition of Mach 4.7 simultaneously, a diffuser shape that can be operable with high efficiency under the wide range of flow conditions was derived.

Finally, important design considerations obtained through this design are presented. Considerations included essential flow characteristics and guidelines to increase stability and efficiency of the HWT. The on-design flow conditions in this study are reservoir pressure of 28.6 bar, total temperature of 2,216 K, and hypersonic flow of 2 kg/s through a Mach 7 nozzle. This condition corresponds to a MW-class large-capacity HWT with a capacity of 13 MW. It is hoped that this study will be useful data when designing a diffuser in an environment where research on HWT diffusers is limited.

Keyword: Hypersonic wind tunnel, Diffuser, Design, CFD, Surrogate model, Sensitivity analysis

Student Number: 2017-36984

Name: Daesan Choi

Contents

Abstract.....	i
LIST OF FIGURES.....	vii
LIST OF TABLES	xii
NOMENCLATURE	xiv
CHAPTER 1 INTRODUCTION.....	1
1.1. Background	1
1.1.1. Hypersonic Wind Tunnel	1
1.1.2. Hypersonic Wind Tunnel Diffuser	2
1.1.3. Previous Research on HWT and HWT Diffuser	3
1.2. Motivation and Objectives.....	6
1.2.1. Large Blockage Model Test in Hypersonic Flow	6
1.2.2. Considering Diffuser as Optimization Target.....	8
1.2.3. Sophisticate and Efficient Design Procedure.....	10
1.3. Outline of Dissertation	13
CHAPTER 2 HYPERSONIC WIND TUNNEL DIFFUSER	14
2.1. Overview	14
2.2. Current Status of HWT	15
2.3. Type of HWT.....	17
2.4. Characteristics of HWT Diffuser	18
2.5. Performance of Diffuser.....	20
2.5.1. Diffuser Operability	20
2.5.2. Diffuser Efficiency	22

CHAPTER 3 METHODOLOGY	2 3
3.1. Overview	2 3
3.2. Flow Analysis	2 4
3.2.1. Governing Equations	2 4
3.2.2. Modeling of Thermal and Chemical Equilibrium	2 5
3.2.3. Modeling of Turbulence	2 7
3.2.4. Numerical Schemes	2 8
3.3. Surrogate Model	2 9
3.3.1. Surrogate Modeling	2 9
3.3.2. Design of Experiments	3 0
3.3.3. Kriging Model	3 1
3.3.4. Assessment of Surrogate Model	3 3
3.4. Sensitivity Analysis	3 6
3.4.1. Global Sensitivity Analysis	3 6
3.4.2. Linear Regression Theory	3 8
3.4.3. Variance based SA – Sobol’ indices	4 1
 CHAPTER 4 GENERAL ASPECTS OF HWT	 4 7
4.1. Overview	4 7
4.2. Innovative Observation Variables Proposed	4 9
4.3. Computational Domain and Boundary Conditions	5 4
4.4. Grid Convergence Study	5 6
4.5. Flow Characteristics of HWT	5 9
4.5.1. Flow Variation along HWT	5 9
4.5.2. Starting Characteristics with Different Back–pressure	6 0
4.5.3. Hysteresis in Starting Process	6 2
 CHAPTER 5 PARAMETERIZATION AND DESIGN OBJECTIVES	 6 4
5.1. Overview	6 4

5.2. HWT Diffuser Shape Parameters	6 5
5.3. Design Objectives and Constraints.....	6 7
5.4. Baseline Configuration and its Performance	6 8
5.4.1. Baseline Configuration of Diffuser	6 8
5.4.2. Performance Analysis of Baseline Diffuser	7 0
CHAPTER 6 PARAMETRIC STUDY BASED DESIGN...	7 3
6.1. Overview	7 3
6.2. Calculation Setup	7 5
6.2.1. Computational Domain.....	7 5
6.2.2. Boundary Conditions	7 5
6.3. Effect of a Blockage Model	7 7
6.4. Diffuser Converging Section	8 1
6.5. Cross Sectional Area of the Diffuser Throat	8 5
6.6. Axial Length of the Diffuser Throat.....	9 2
6.7. Diffuser Diverging Section.....	9 6
6.8. Diffuser Shape Derived from Parametric Study	9 8
CHAPTER 7 SURROGATE MODEL BASED DESIGN.	1 0 1
7.1. Overview	1 0 1
7.2. Framework.....	1 0 3
7.3. Kriging Model	1 0 4
7.3.1. Design Space Feasibility Study	1 0 4
7.3.2. Generation of Kriging Model.....	1 0 6
7.3.3. Reliability Assessment of Kriging Model.....	1 0 8
7.3.4. Kriging Response Surface and Design Space Exploration	1 1 1
7.3.5. HWT Diffuser Design using Kriging Model	1 1 6
7.4. Design considering Off–design Condition.....	1 2 0
7.4.1. Motivation	1 2 0
7.4.2. On–design and Off–design Condition	1 2 0

7.4.3. Design Objectives.....	1 2 2
7.4.4. Optimization Procedure.....	1 2 3
7.4.5. HWT Diffuser Design considering Off–design Condition.	1 2 8
7.4.6. Summary of Derived Designs	1 2 9
CHAPTER 8 SENSITIVITY ANALYSIS	1 3 1
8.1. Overview	1 3 1
8.2. Deduction of Sensitivity Indices	1 3 3
8.2.1. Calculation of Sobol’ Indices.....	1 3 3
8.2.2. Convergence of Variance based Sensitivity Indices	1 3 4
8.3. SA for HWT Diffuser Performance	1 3 7
8.3.1. General Procedure of SA	1 3 7
8.3.2. SA for Operability of HWT Diffuser.....	1 3 8
8.3.3. SA for Efficiency of HWT Diffuser	1 4 0
CHAPTER 9 CONCLUSION	1 4 6
9.1. Summary	1 4 6
9.2. Design Considerations for HWT diffuser design	1 4 9
9.3. Limitations and Future Works	1 5 1
BIBLIOGRAPHY	1 5 9
국문 초록	1 6 5

LIST OF FIGURES

Fig. 1. Schematic of a hypersonic wind tunnel.....	2
Fig. 2. Schematics of conventional design process for HWT diffuser	5
Fig. 3. Configuration of NASA Langley AHSTF (dimension unit converted from (Witte et al., 2004))	9
Fig. 4. Schematics of parametric study based design process for HWT diffuser.....	1 1
Fig. 5. Schematics of surrogate model based design process for HWT diffuser.....	1 2
Fig. 6. Outline of the dissertation.....	1 3
Fig. 7. Worldwide MW class large–capacity hypersonic wind tunnels (Borrelli & Martucci, 2011).....	1 5
Fig. 8. Country wise breakdown of hypersonic wind tunnels (Shams et al., 2020)	1 6
Fig. 9. Capabilities of aerothermal facility (modified from (Shams et al., 2020)).....	1 7
Fig. 10. Pressure contour difference according to Reynolds number (modified from (Savino et al., 1999)).....	1 9
Fig. 11. Schematics of operable (up) and inoperable (down) state of diffuser.....	2 1
Fig. 12. Concept of krigng model	3 1
Fig. 13. Pressure distributions of configuration A (inefficient diffuser) and B (efficient diffuser)	5 1
Fig. 14. Diffuser wall pressure distribution of configuration A (inefficient diffuser) and B (efficient diffuser)	5 2
Fig. 15. Centerline Mach number distribution of configuration A (inefficient diffuser) and B (efficient diffuser)	5 2
Fig. 16. Average total pressure and average static pressure along the axial direction of configuration A (inefficient diffuser) and B	

(efficient diffuser).....	5 3
Fig. 17. Configuration of computation domain and boundary conditions applied.....	5 5
Fig. 18. Shock wave configurations at front section of domain with various grid levels.....	5 7
Fig. 19. Average static pressure distributions for various grid levels	5 8
Fig. 20. Average Mach number distributions for various grid levels	5 8
Fig. 21. Flow distributions and trends of pressure, Mach number, and total pressure	6 0
Fig. 22. Pressure distribution at different back–pressures.....	6 2
Fig. 23. Static pressure at test section ($x = 0.5$ m) based on different back–pressures applied.....	6 3
Fig. 24. Different pressure and Mach number distribution at back–pressure of 5,000 Pa.....	6 3
Fig. 25. Shape parameters of the diffuser	6 5
Fig. 26. Pressure distribution of the test section and initial part of the diffuser of baseline configuration A and B.....	7 0
Fig. 27. Pressure distribution and terminal shock location of baseline configuration B with different back–pressures.....	7 1
Fig. 28. Average static pressure along the axis of baseline configuration B with different back–pressures.....	7 2
Fig. 29. Average Mach number along the axis of baseline configuration B with different back–pressures.....	7 2
Fig. 30. Computational domain and boundary conditions.....	7 6
Fig. 31. Pressure distribution of the test section and initial part of the diffuser with different model blockage ratios.....	7 8
Fig. 32. Average total pressure along the axial direction with different blockage ratios	8 0
Fig. 33. Pressure distribution of the initial part of the diffuser with different converging shapes and back–pressures	8 3
Fig. 34. Average total pressure along the axial direction for different converging shapes and back–pressures.....	8 4
Fig. 35. Intermediate result of pressure distribution with area ratio (AR) of 400 at a back–pressure of 5,500 Pa	8 8
Fig. 36. Pressure distribution and terminal shock location with different values of area ratio (AR) at a back–pressure of 5,500	

Pa	8 9
Fig. 37. Average Mach number along the axial direction for different values of throat area ratio (AR) at a back-pressure of 5,500 Pa	9 0
Fig. 38. Average total pressure along the axial direction for different values of area ratio (AR) at a back-pressure of 5,500 Pa	9 0
Fig. 39. Pressure distribution and terminal shock location with different values of L/Dt2 at a backpressure of 5,500 Pa	9 4
Fig. 40. Average total pressure along the axial direction with different values of L/Dt2	9 5
Fig. 41. Streamline and axial velocity distribution in the diffuser diverging section with different diverging half-angles	9 7
Fig. 42. Average static pressure along the axis for the designed diffuser with different backpressures.....	1 0 0
Fig. 43. Average Mach number along the axis for the designed diffuser with different backpressures.....	1 0 0
Fig. 44. Flow-chart and framework of the study	1 0 3
Fig. 45. Operability of the Sampled configurations of the HWT diffuser.....	1 0 5
Fig. 46. The shape variables of the existing HWT diffusers and the shape variables calculated by the conventional design method, together with the design variable range of present study..	1 0 6
Fig. 47. Leave-one-out-cross-validation result of the constructed kriging model for maximum operable back-pressure	1 0 9
Fig. 48. Convergence history of determination coefficient of linear regression between kriging prediction and CFD calculation in LOOCV	1 0 9
Fig. 49. Convergence history of NRMSE between kriging prediction and CFD calculation in LOOCV	1 1 0
Fig. 50. Convergence history of MAE between kriging prediction and CFD calculation in LOOCV	1 1 0
Fig. 51. Kriging response surface (left) and slice chart (right) for maximum back-pressure according to design variables AR and Lsep	1 1 2
Fig. 52. Kriging response surface (left) and slice chart (right) for maximum back-pressure according to design variables AR and Din	1 1 2
Fig. 53. Kriging response surface (left) and slice chart (right) for	

maximum back–pressure according to design variables AR and Lcs	1 1 3
Fig. 54. Kriging response surface (left) and slice chart (right) for maximum back–pressure according to design variables AR and α	1 1 3
Fig. 55. Kriging response surface (left) and slice chart (right) for maximum back–pressure according to design variables Din and AR	1 1 4
Fig. 56. Kriging response surface (left) and slice chart (right) for maximum back–pressure according to design variables AR and L/D	1 1 4
Fig. 57. Kriging response surface (left) and slice chart (right) for maximum back–pressure according to design variables AR and β	1 1 5
Fig. 58. Kriging response surface (left) and slice chart (right) for maximum back–pressure according to design variables AR and Dexit	1 1 5
Fig. 59. Pressure distribution and terminal shock location of diffuser from surrogate model with different back–pressures.....	1 1 8
Fig. 60. Average static pressure along the axis for the designed diffuser from surrogate model with different back–pressures. 1	1 9
Fig. 61. Average Mach number along the axis for the designed diffuser from surrogate model with different back–pressures. 1	1 9
Fig. 62. Distribution of predicted performance function values according to terms constituting the performance function (blue symbol represent inoperable designs).....	1 2 5
Fig. 63. Distribution of predicted performance fuction according to NPBs	1 2 5
Fig. 64. Distribution of predicted performance fuction according to NPB7.0 and NSIZE	1 2 6
Fig. 65. Distribution of predicted performance fuction according to NPB7.0 and NSIZE	1 2 6
Fig. 66. Configurations of designed diffusers and NASA AHSTF (rescaled x to y ratio to be 20 % for clarity)	1 3 0
Fig. 67. Convergence history of total Sobol’ indices for HWT diffuser operability	1 3 5

Fig. 68. Convergence history of first order Sobol' indices for HWT diffuser operability	1 3 5
Fig. 69. Convergence history of total Sobol' indices for HWT diffuser maximum operable back-pressure	1 3 6
Fig. 70. Convergence history of first order Sobol' indices for HWT diffuser maximum operable back-pressure	1 3 6
Fig. 71. Correlation coefficient between shape design variables and operability / maximum operable back-pressure.....	1 3 9
Fig. 72. Relative contribution of each variable on the variance of operability from variance based sensitivity analysis	1 4 0
Fig. 73. Correlation coefficient between shape design variables and operability / maximum operable back-pressure (identical figure to Fig. 71)	1 4 1
Fig. 74. Relative contribution of each variable on the variance of maximum operable back-pressure from variance based sensitivity analysis.....	1 4 2
Fig. 75. Scatterplot between separation length and maximum operable back-pressure	1 4 3
Fig. 76 Scatterplot between inlet diameter and maximum operable back-pressure	1 4 3
Fig. 77 Scatterplot between catch-cylinder length and maximum operable back-pressure	1 4 3
Fig. 78 Scatterplot between converging angle and maximum operable back-pressure	1 4 4
Fig. 79 Scatterplot between throat area ratio and maximum operable back-pressure	1 4 4
Fig. 80 Scatterplot between the length to diameter ratio of diffuser throat and maximum operable back-pressure	1 4 4
Fig. 81 Scatterplot between diverging angle and maximum operable back-pressure	1 4 5
Fig. 82 Scatterplot between exit diameter and maximum operable back-pressure	1 4 5

LIST OF TABLES

Table 1. Comparison of specifications between CIRA' s SCIROCCO and GHIBLI HWT (Borrelli & Martucci, 2011; Purpura et al., 2007)	7
Table 2. Difference between general SWT and PWT.....	1 8
Table 3. Various reliability assessment metrics of surrogate model	3 4
Table 4. Comparison of various GSA techniques.....	3 8
Table 5 Diffuser shape parameters and pressure recovery of low and high efficient configurations (Detailed descriptions for each shape parameter is given in Chapter 5).....	5 1
Table 6. Flow properties at nozzle inlet and exit.....	5 5
Table 7. Node dimensions of each grid level	5 6
Table 8. Description of each design parameter (PBD: Parametric study based design, SBD: Surrogate model based design)	6 6
Table 9. Design parameters and pressure recovery performance of baseline diffuser	6 9
Table 10. Flow properties at the reservoir and nozzle exit.....	7 6
Table 11. Diffuser shape parameters and pressure recovery in parametric study for converging section.....	8 2
Table 12. Diffuser shape parameters and pressure recovery in the parametric study for the diffuser throat area.....	8 7
Table 13. Diffuser shape parameters and pressure recovery for the parametric study of throat length.....	9 3
Table 14. Diffuser shape parameters and pressure recovery in the parametric study for diverging half-angle	9 6
Table 15. Design variables and performance of HWT diffuser determined via conventional and parametric study-based design procedures.....	9 9
Table 16. Design space determined.....	1 0 5

Table 17. Coefficients for the constructed kriging model for operability and maximum operable back-pressure	1 0 7
Table 18. Design variables and performance of HWT diffusers determined via various design procedures.....	1 1 7
Table 19. Reservoir conditions and calculated nozzle exit flow variables of NASA Langley AHSTF according to inflow Mach number	1 2 1
Table 20. Predicted values and CFD analysis values for the maximum backpressure for design candidates.....	1 2 7
Table 21. Design variables and performance of HWT diffusers	1 2 8
Table 22. Normalized variance decomposition based sensitivity indices (Sobol' indices) for operability and maximum operable back-pressure	1 3 3
Table 23. Reservoir and nozzle exit flow conditions of NASA Langley AHSTF according to inflow Mach number (including mass flow rate)	1 5 4

NOMENCLATURE

Part of Flow Analysis

x	: Axial displacement
y	: Radial displacement
Q	: Conservative variable vector
E	: Convective flux vector in axial direction
F	: Convective flux vector in radial direction
E_v	: Diffusive flux vector in axial direction
F_v	: Diffusive flux vector in radial direction
H	: Additional convective source vector describing axisymmetric flow
H_v	: Additional diffusive source vector describing axisymmetric flow
ρ	: density
u	: Axial velocity
v	: Radial velocity
e_t	: Total energy
p	: Pressure
h	: Enthalpy
τ	: Stress tensor
μ	: Viscosity coefficient
λ	: Second viscosity coefficient
μ_l	: Molecular viscosity coefficient
μ_t	: Eddy viscosity coefficient
\dot{q}	: Heat transfer rate
Pr	: Prandtl number
κ	: Thermal conductivity

γ	: Specific heat ratio of thermal and chemical equilibrium gas (air)
k	: Turbulent kinetic energy
ε	: Turbulent dissipation rate
\vec{V}	: Velocity vector
$\bar{\bar{E}}$: Strain rate tensor
P_0	: Total pressure
T_0	: Total temperature
\dot{m}	: Mass flow rate
M	: Mach number

Part of Surrogate Modeling

y	: Objective function value
\hat{y}	: Predicted value of objective function
\bar{y}	: Mean of sample's objective function values
μ	: Global trend model
ε	: Local deviation from the global model
x^i	: i th sample
\mathbf{x}	: Vector of sample
σ	: Standard deviation of local deviation
$\hat{\mu}$: Estimated global mean of ordinary kriging
$\hat{\sigma}$: Estimated standard deviation of local deviation
$\mathbf{1}$: Unit diagonal matrix
\mathbf{R}	: Spatial covariance matrix of local deviation
d	: Gaussian distance function
\mathbf{y}	: Vector of objective function value
n	: Total number of samples
$\hat{\boldsymbol{\mu}}$: Vector of estimated global mean value
θ_k	: Kriging coefficient of k -th parameter
i, j	: index of samples
k	: index of parameter
m	: Total number of parameters

\mathbf{r}	: Spatial correlation vector
Ln	: Likelihood function

Part of Sensitivity Analysis

n	: Number of samples
r	: Number of trajectories in Morris screening
m	: Number of factors
σ^2	: Population variance
V, s^2	: Sample variance
σ	: Population standard deviation
s	: Sample standard deviation
σ_{xy}	: Population covariance
s_{xy}	: Sample covariance
ρ	: Population correlation coefficient
R	: Sample correlation coefficient
R^2	: Determination coefficient
$f(\mathbf{x})$: Model, dependent variable
x_i	: <i>i th</i> input variable
f_0	: Global mean
f_i	: Main effect of <i>i th</i> variable
f_{ij}	: Interaction effect of <i>i and j th</i> variables
$f_{1,2,\dots,m}$: Interaction effect of all variables
V_i	: Partial variance term of <i>i th</i> variable
V_{ij}	: Partial variance term of interaction of <i>i and j th</i> variables
V_{T_i}	: Total variance term of <i>i th</i> variable
S_i	: First order sensitivity indices of <i>i th</i> variable
S_{ij}	: Interaction sensitivity indices of interaction of <i>i and j th</i> variables
S_{T_i}	: Total sensitivity indices of <i>i th</i> variable
$\sim i$: All possible cases except <i>i th</i> variable

CHAPTER 1

INTRODUCTION

1.1. Background

1.1.1. Hypersonic Wind Tunnel

Over the years, hypersonic applications have been extensively studied using plasma or hypersonic wind tunnels. Studies related to scramjet (Rabadan Santana & Weigand, 2021; Riehmer et al., 2014; Saravanan et al., 2021), ablation and re-entry (Gardi et al., 2011; Noh & Kim, 2019; Saccone et al., 2016), and heat transfer at hypersonic flow (Gonzales et al., 2021) have been actively conducted. Moreover, research on hypersonic wind tunnels has been conducted (Agostinelli et al., 2020; Shams et al., 2020; Solomon, 2021).

Hypersonic wind tunnel (HWT) is a device simulating hypersonic and high-enthalpy flow environments on the ground. In general, these facilities comprise a plasma generator or heater, nozzle, test section, diffuser, heat exchanger, and vacuum facility (Fig. 1). The plasma generator generates a high-enthalpy gas and the nozzle accelerates the heated gas, resulting in the hypersonic and high-enthalpy flow in the test section. The gas passes through the test section, diffuser, and heat exchanger before entering the vacuum facility.

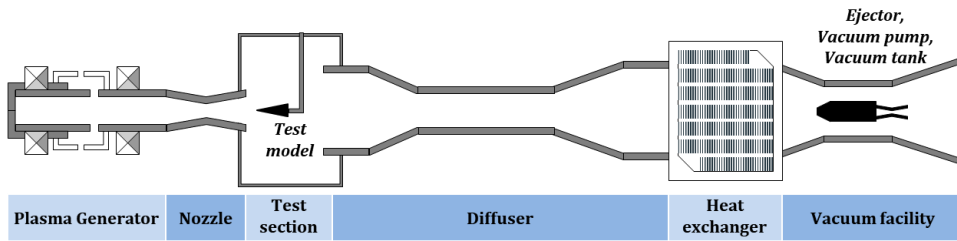


Fig. 1. Schematic of a hypersonic wind tunnel

In comparison with the construction and operation of conventional supersonic wind tunnel, those of HWT is more challenging. A HWT requires a high-pressure ratio between the test section and diffuser exit for its operation (Savino et al., 1999) and is typically intended for continuous long-term operations (R.S Pugazenthil & Andy C. McIntosh, 2011). Furthermore, the test model generates an additional total pressure loss in the test section and an increased risk of spillage of the deflected flow into the test section. Therefore, a hypersonic wind tunnel requires a large-scale pressure tank, vacuum facility, and plasma generator with high power. The cost of constructing and operating these facilities is considerably high, rendering the construction of the required hypersonic wind tunnel difficult.

1.1.2. Hypersonic Wind Tunnel Diffuser

HWT diffuser is used to address the problems mentioned in the previous section. The hypersonic / supersonic flow in the diffuser decelerates to a subsonic flow during the total pressure loss caused by the shock wave, friction, heat transfer, and other factors. An efficient diffuser can achieve a high pressure recovery to reduce the required total pressure ratio by minimizing the loss in the diffuser. Additionally, an appropriately designed diffuser can prevent blockage and spillage by capturing and passing the flow from the nozzle.

However, designing an efficient diffuser for a HWT is more challenging than designing that of a supersonic wind tunnel. The flow in a HWT exhibits a high temperature and low Reynolds number,

resulting in a dominant viscous effect that renders the flow different from that of a supersonic wind tunnel (Monti et al., 2001; Savino et al., 1999). This is particularly true when the duct of a HWT is small, with a diameter of the nozzle exit of the order of a few centimeters. Under these conditions, complex flow structures, such as thick boundary layers and strong shock–boundary–layer interactions occur, and the total pressure loss is substantially higher than that of a general supersonic wind tunnel diffuser (Monnerie, 1967; Savino et al., 1999). Moreover, the HWT requires additional components, such as a heater or plasma generator, heat exchanger, and vacuum facility, which complicate the designing of a diffuser further. Especially, the performance capabilities of the vacuum facility must be considered in the diffuser designing.

1.1.3. Previous Research on HWT and HWT Diffuser

Several studies (Brune et al., 2019; Monti et al., 2001; Savino et al., 1999) have reported that the design of HWT diffusers has not been investigated extensively. Previous studies have primarily focused on exploring experimental methods of designing the diffusers. Wegener et al. conducted an experimental study on the diffuser performance by varying the diffuser throat configuration (Wegener & Lobb, 1953). Hanus et al. investigated the influence of the blockage ratio of a model and diffuser throat length (HANUS et al., 1991). Additionally, Monnerie et al. presented a simple theoretical prediction based on various shape parameters of the diffuser and conducted comparative studies using experimental data (Monnerie, 1967). However, owing to the fundamental limitations of the experiments, the aforementioned studies did not investigate the various diffuser shapes and their flows sufficiently.

Furthermore, numerical studies have investigated the internal flow of the HWT diffuser, and the performance of HWTs has been evaluated by estimating the maximum operable back–pressure condition. Savino et al. studied the effect of a low Reynolds number

inside a hypersonic wind tunnel and evaluated the diffuser performance considering various back-pressure conditions (Savino et al., 1999). Monti et al. investigated the flow in a diffuser with different back-pressures in a subscale model of a hypersonic wind tunnel (Monti et al., 2001). Agostinelli et al. evaluated the performance of a HWT diffuser along with an ejector system and presented a detailed description of the computational fluid dynamics procedure (Agostinelli et al., 2020). Brune et al. executed the flow analysis and performance evaluation of a HWT diffuser under various conditions and conducted studies on diffuser boundary conditions, non-equilibrium influence, and diffuser cooling systems (Brune et al., 2019).

Several studies have focused on the design of HWT diffusers. Pugazenthi et al. presented a design methodology and thumb rules of design for each part of the diffuser and predicted its performance using numerical simulations. However, the diffuser shape was not optimized, and the presented design methodology was primarily aimed at a preliminary configuration of the diffuser (R.S Pugazenthi & Andy C. McIntosh, 2011). Agostinelli et al. had confronted an unstaring problem of HWT, and successfully solved the unstaring problem by redesigning the diffuser based on the shape of the existing HWT diffusers (Agostinelli et al., 2019). Similarly, HWT diffusers have been designed based on design thumb rules or existing shapes; however, this design can generate inefficient or inoperable diffusers. As a preceding study of this study, an efficient diffuser shape was designed based on a parametric study using CFD analysis (Choi et al., 2021), or an idea for improving diffuser performance was presented (Sol Baek et al., 2022), but it is difficult to say that related research has been sufficiently conducted.

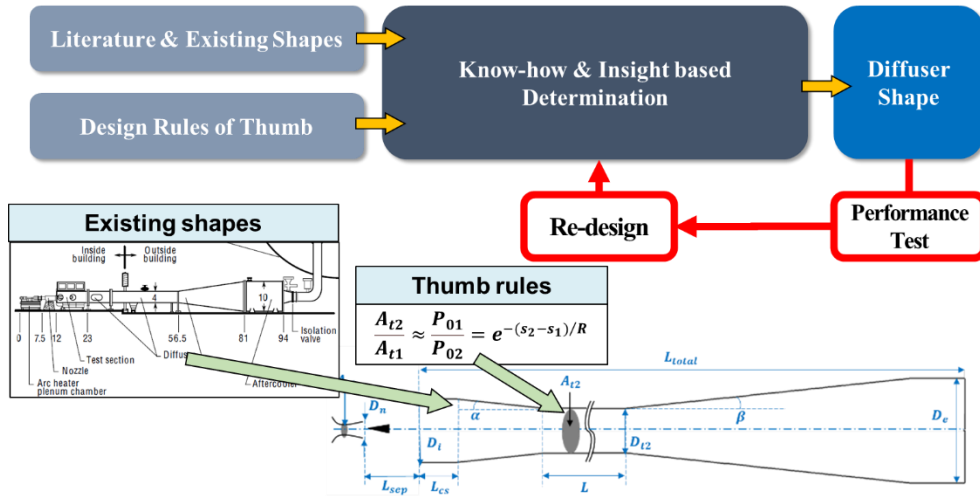


Fig. 2. Schematics of conventional design process for HWT diffuser

1.2. Motivation and Objectives

1.2.1. Large Blockage Model Test in Hypersonic Flow

One of the hardest difficulties of this study was a highly challenging design objective. As will be described later, one of the most important goals of this study was to derive a diffuser shape that can test a model with a blockage ratio of 40% in the hypersonic flow of Mach 7. Considering that the design of an operable HWT have been considered to be highly difficult (Monti et al., 2001; Savino et al., 1999; Shams et al., 2020), and some inoperability were reported even in freejet condition where a model did not exist in test section (Agostinelli et al., 2019), including the model made this design objective much challenging.

The consensus in wind tunnel testing has been that test models should be manufactured according to the scale of wind tunnel, and if it is necessary to test a large-size model, it requires a larger wind tunnel. This is a safe decision, although it will incur excessive cost. In general, HWTs at Mach number 7 have been tested with a blockage ratio of about 10 to 20%, and a blockage ratio higher than that range has been considered virtually difficult to test. In the case of the experimental literature with similar inflow conditions to present study, it was confirmed that the HWT test was difficult from about 10% of blockage at Mach 7 (Austin, 1966).

However, when trying to increase the size of a HWT in proportion to the size of a test model in the conventional way, an exponential increase in cost will occur. For example, as in this study, if trying to increase the test model size to 4 times the general level, the duct area of the nozzle and diffuser should be approximately 16 times larger. Since this duct needs to be filled with flow, the power consumption for a gas generator will increase exponentially. Likewise, the required power of the heat exchanger and vacuum facility will increase exponentially, rendering a rapid increase in cost.

The rapid increase in required power can also be confirmed through the examples of SCIROCCO and GHIBLI HWTs in CIRA, Italy.

SCIROCCO is, to the author's best knowledge, the world's largest HWT, and GHIBLI is SCIROCCO's scaled-down wind tunnel. It is known that a reduced-scale wind tunnel called GHIBLI was created because it is unnecessarily expensive to test small-sized models with SCIROCCO (Purpura et al., 2007). As shown in the Table 1, SCIROCCO can test a model of about 600 mm, and GHIBLI can test a model of 80 mm. Looking at the power of the arc heater required, it is 70:2, which is about 35 times the difference. In terms of multipliers, the required power is about the 1.8 power of the model size ratio, and it seems that the required power varies considerably depending on the size of the wind tunnel.

Table 1. Comparison of specifications between CIRA's SCIROCCO and GHIBLI HWT (Borrelli & Martucci, 2011; Purpura et al., 2007)

	SCIROCCO	GHIBLI	Multiple
Arc Heater Power (max) [MW]	70	2	35.0
Gas Mass Flow Rate (max) [kg/s]	5	0.6	8.3
High Temperature Simulation	~10,000K	~1300kW/m ²	-
Nozzle Exit Diameter [mm]	~1950	152	12.8
Mach Number	12	10	1.2
Max Model Size [mm]	600	80	7.5
Max Blockage Ratio	9%	28%	-

Therefore, it was judged that the design method of simply increasing the size of HWT for the test of a large model was a quit inefficient approach, and above all, it was a method that could not be used in this study, which had considerably limited resources. In this study, prior to the design of the diffuser, the reservoir condition, the shape and size of the nozzle, and the specifications of the vacuum facility were limited for practical reasons such as cost.

Under these circumstances, this study aimed to make the hypersonic test with the large blockage model possible by focusing on designing the diffuser innovatively. It was highly challenging design objective to enable the test of a considerably large blockage model of 40% in a fixed reservoir condition and vacuum facility by designing only the shape of the diffuser.

1.2.2. Considering Diffuser as Optimization Target

Until now, HWT diffusers have been just subject to simply sizing, but in this study, the diffuser was more elaborately designed and optimized to enable large-size model tests under quit challenging design constraints. In addition, by maximizing the efficiency of the diffuser, the construction and operational cost were reduced as much as possible.

Fig. 3 shows the configuration of NASA Langley's AHSTF (Witte et al., 2004). The reservoir conditions in this study were determined identical to those of the AHSTF. The front of the HWT diffuser of AHSTF is simply composed of a cylindrical shape with a large diameter and a conical subsonic diffuser at the rear. A large duct size may have the advantage of reducing the risk of spillage of the flow ejected from the nozzle even in various models and various flow conditions, and preventing the risk of not passing the entire flow rate due to choking that may occur in the diffuser.

However, as will be described in detail later, when considering the efficiency of the diffuser, the cylinder diameter of the diffuser was judged to be excessively large, which resulted in severely adverse effect on the diffuser efficiency. The size of the subsonic diffuser is also judged to be excessive and can be a factor that increases the construction cost.

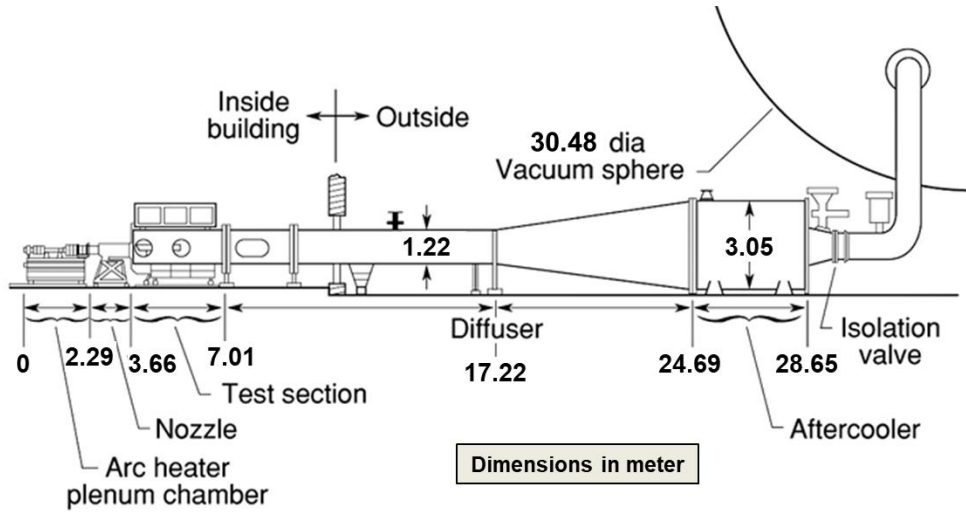


Fig. 3. Configuration of NASA Langley AHSTF (dimension unit converted from (Witte et al., 2004))

What should be noted in Fig. 3 is the large-scale vacuum tank with a diameter of more than 30 m. It is judged that the performance of these vacuum facilities would have made it possible to successfully test even with the quit inefficient diffuser shape. In other words, the major advanced countries in aerospace fields, which are relatively free in terms of cost and space, would be easy to build and operate large-scale HWTs. Rather than the need for challenging efforts to design and increase the efficiency of diffusers, it is judged that the advanced countries has been focusing on stable test even if excessive costs would be incurred.

Therefore, an efficient diffuser design study to enable a test in challenging circumstances (requiring larger model test, limited reservoir conditions, wind tunnel size, vacuum facility specifications) has not be sufficient performed. However, as will be shown in this study, well-designed diffusers can enable tests under challenging conditions that were conventionally considered impossible and maximize diffuser efficiency to reduce construction and operation costs.

The present study primarily focused on the operability of diffuser, and reducing total pressure loss, in other words, improving the efficiency of the diffuser. Thereby this study relieved the required

pressure ratio and designing a HWT diffuser for a large-sized model test under restrictive conditions. For this objective, the conventional design method could not be used, and a more sophisticated design method was used as described in following section. Valuable design considerations were introduced in the process of successfully deriving a high efficiency diffuser that can operate under severe conditions.

1.2.3. Sophisticate and Efficient Design Procedure

As mentioned in *1.1. Background* section, in the background of the fatal limitations of the conventional design method and the quite insufficient HWT diffuser related research, it will be difficult to derive an efficient diffuser shape using the conventional method. Above all, there is a high risk of deriving an inoperable or highly inefficient diffuser shape from the conventional design. The present study tried to resolve this problem and the problem that the conventional design relies on the insights or know-how of researchers.

Efficient HWT diffuser was designed by using a design method that was more sophisticated than the conventional method. The first method was parametric study based design, and the second method was surrogate model based design. Before design study, the fundamental characteristics of the HWT were analyzed through numerical analysis, and an innovative observation value useful for effective diffuser design were newly proposed.

In the parametric study based design (Fig. 4), a parametric study was performed through numerical analysis for each design variable. The effect of each design variable on the diffuser efficiency was investigated. This study primarily focused on reducing total pressure loss, in other words, improving the pressure recovery or the efficiency of the diffuser, thereby relieving the required pressure ratio and designing a HWT diffuser for a large-sized model test under restrictive conditions.

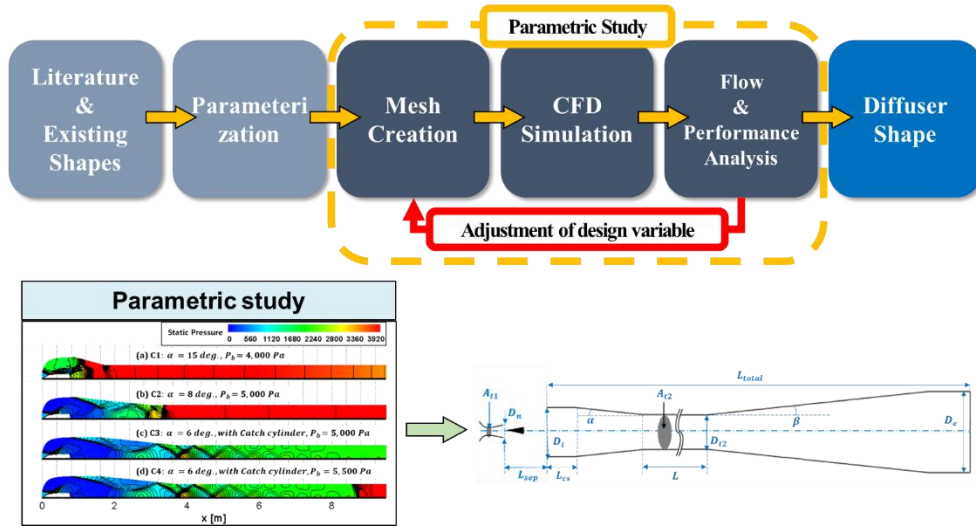


Fig. 4. Schematics of parametric study based design process for HWT diffuser

However, the parametric study based design method is inefficient in terms of time and resource because parametric studies must be repeatedly performed until the design requirements are satisfied. Therefore, surrogate model based design study (Fig. 5) was conducted to resolve this inefficiency. In this design method, once a reliable surrogate model was established, the diffuser performance according to the shape of the diffuser could be immediately derived, so it was used for diffuser design and sensitivity analysis effectively.

First, a framework was established to analyze the diffuser design space systematically and efficiently. The framework consists of a DOE based analysis point sampler, an automated flow analysis and diffuser efficiency evaluation module, a kriging surrogate model generation module, and a sensitivity analysis module. Using this framework, the present study thoroughly evaluate the HWT diffuser design space by using surrogate model without excessive numerical analysis. The influence of each variable on the diffuser performance was quantitatively and comprehensively investigated.

Using the constructed surrogate model, the diffuser shape of the hypersonic wind tunnel with higher efficiency at Mach 7 was derived. This shape had higher efficiency than the shape from the parametric

based design method. Subsequently, as a further study assuming a more general situation, a diffuser with high efficiency not only in the on-design Mach 7 flow condition but also in the off-design Mach 4.7 flow condition (that is, to cover a wide range of flow condition and achieve high efficiency) was derived.

The results of the study could serve as a guide for achieving higher pressure recovery of a HWT diffuser. In addition, owing to the limited related studies in current literature, it is expected that this study could be a reference for designing a HWT diffuser.

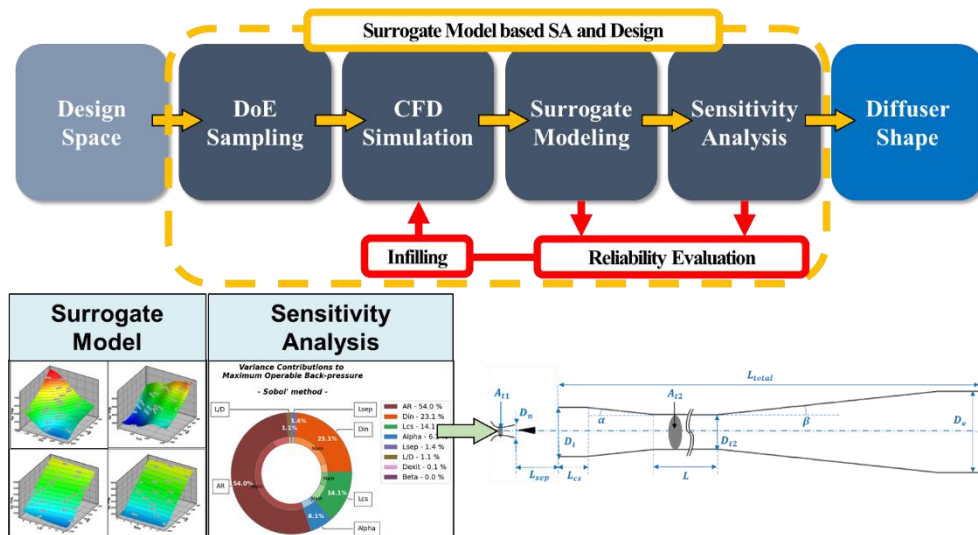


Fig. 5. Schematics of surrogate model based design process for HWT diffuser

1.3. Outline of Dissertation

The outline of this dissertation is shown in Fig. 6. After explaining the background and motivation of this study in Chapter 1, Chapter 2 deals with the core concept of the HWT diffuser, the subject of this study. In Chapter 3, the theories used in the design study were described in detail. In Chapter 4, the flow characteristics of HWT were analyzed through CFD analysis. After that, the contents of design study appear. In Chapter 5, the diffuser shape is defined as a parameter and the design problem is defined. Chapter 6 for parametric study based design, and Chapters 7 and 8 for surrogate model-based design and sensitivity analysis are structured in parallel. This is followed by the conclusion of Chapter 9.

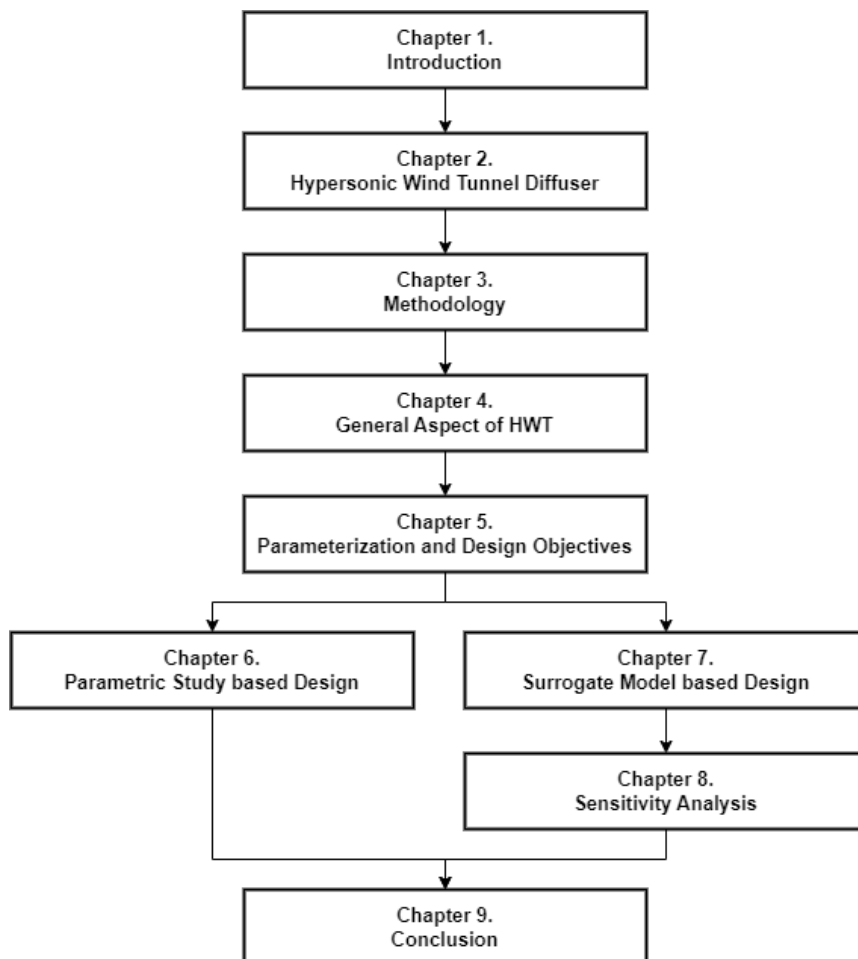


Fig. 6. Outline of the dissertation

CHAPTER 2

HYPersonic WIND TUNNEL DIFFUSER

2.1. Overview

This chapter deals with the core concept of the HWT diffuser. Briefly review the current status of HWT constructed worldwide, classify HWT into “hot wind tunnel” and “cold wind tunnel,” and describe each characteristic. The operating conditions of this study belong to the “cold wind tunnel.” After that, the general characteristics of the internal flow of the HWT were examined from previous studies. It was confirmed that these general characteristics make it difficult to analyze the diffuser and predict its performance. Finally, the performance of the diffuser, which will be the objective function values throughout the study, was examined by dividing it into two aspects: operability and efficiency.

2.2. Current Status of HWT

In the world, major advanced countries built not only small-scale hypersonic facilities, but also MW-class large-capacity HWT (Fig. 7), and actively conducted research through these HWT. These useful facilities are mainly concentrated in major advanced countries (Fig. 8). These facilities are not available to other countries, because related information or data of HWT is of secret nature. Therefore, it is judged that the construction of hypersonic facilities in each country is necessary for effective research in the aerospace field.

In South Korea, several experimental studies have been conducted using small scale HWT existing at Chonbuk National University (M. Kim et al., 2013), but large capacity HWT construction and research on it have not yet been sufficiently conducted.

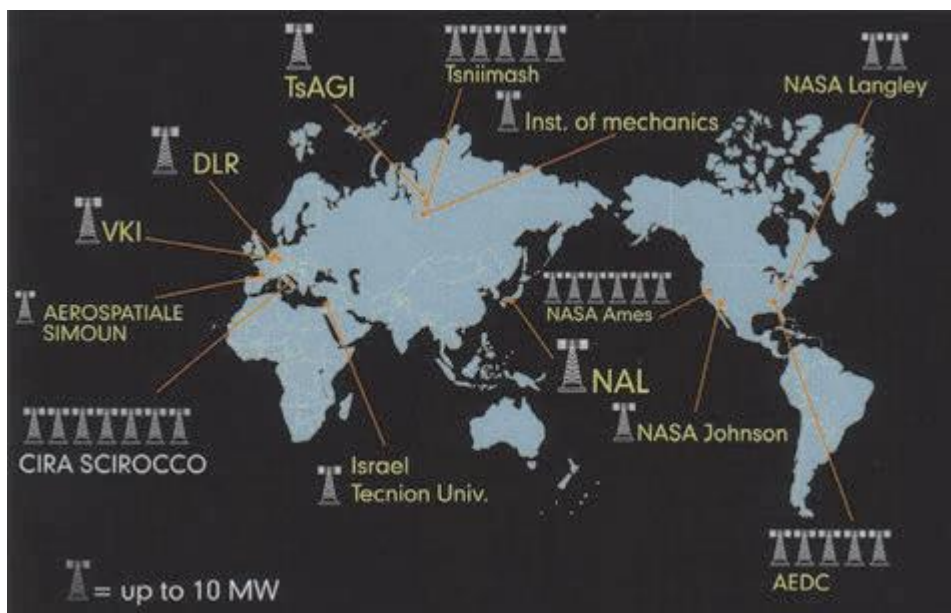


Fig. 7. Worldwide MW class large-capacity hypersonic wind tunnels (Borrelli & Martucci, 2011)

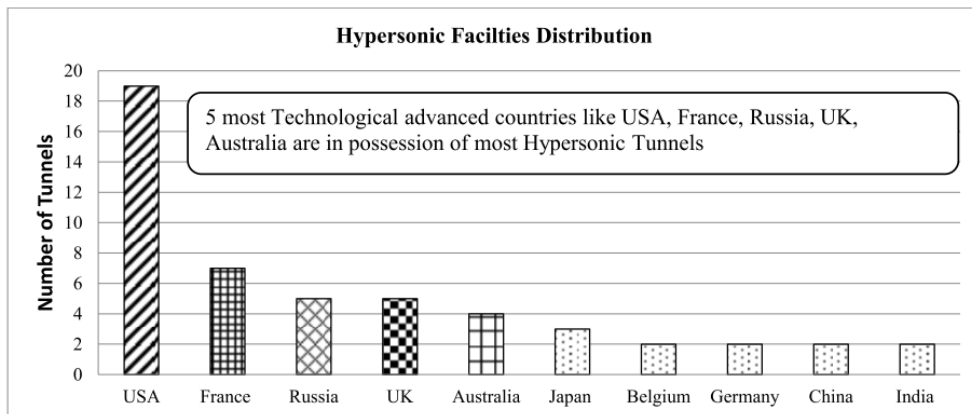


Fig. 8. Country wise breakdown of hypersonic wind tunnels (Shams et al., 2020)

2.3. Type of HWT

Fig. 9 shows the operational area of the ground test facilities. HWT can be divided into two categories. First, in the case of a “Hot wind tunnel,” the heater heats the gas up to 10,000 K, which will require arc-heater. This wind tunnel is mainly used for reentry or ablation research, and simulates the high enthalpy, high temperature, and chemical reaction.

Next, in the case of a “Cold wind tunnel,” it is operated at a relatively low temperature about 2,000 K, where the heater heats the gas just enough to prevent liquefaction of gas during the high Mach expansion. In general, it simulates the Mach number and is mainly used for high-speed vehicles and ramjet/scramjet test.

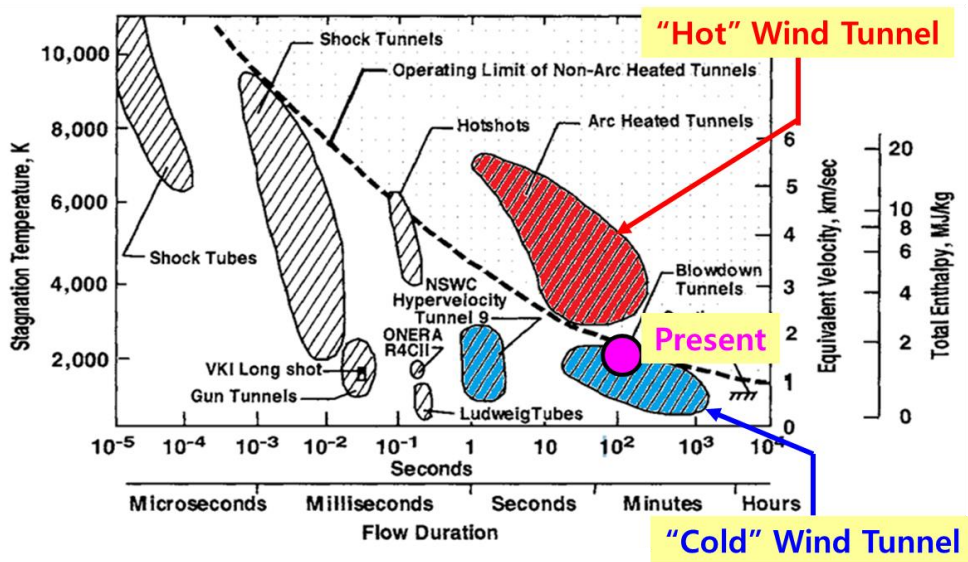


Fig. 9. Capabilities of aerothermal facility (modified from (Shams et al., 2020))

2.4. Characteristics of HWT Diffuser

HWT exhibits several characteristics compared to normal supersonic wind tunnel (SWT). Table 2 summarizes the comparison between HWT and SWT. All the features described here are what makes a high efficiency diffuser even more important in HWT.

First, the HWT must transport the flow at high speed, so a severe total pressure loss occurs in this process. Therefore, a high pressure ratio corresponding to this pressure loss is required.

Next, HWT is characterized by a particularly long test time in the case of an ablation test. Therefore, the cost burden required for operation of HWT is far greater than that of SWT, where the efficient diffuser becomes more important.

Finally, even in the case of a cold wind tunnel, HWT has much higher temperature distribution than SWT. So, HWT is characterized by a low Reynolds number due to their high temperature and relatively small duct size. Fig. 10 shows the shock wave configuration according to the Reynolds number. A low Reynolds number makes the shock wave damped due to the high viscous effect, which causes a greater entropy rise (pressure loss). This feature not only makes flow analysis and performance prediction difficult, but also adversely affects the burden of high pressure ratio required for wind tunnel operation.

Table 2. Difference between general SWT and PWT

	Pressure Ratio	Test Duration [sec.]	Reynolds Number ($Re_D = \frac{\rho_\infty V_\infty D}{\mu_\infty}$)
SWT	$10^0 \sim 10^2$	$10^1 \sim 10^2$	$10^5 \sim 10^7$
HWT	$10^2 \sim 10^3$	$10^0 \sim 10^3$	$10^2 \sim 10^5$ (Present 2×10^4)

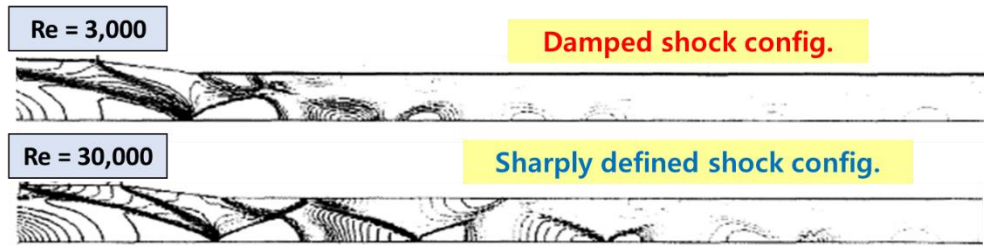


Fig. 10. Pressure contour difference according to Reynolds number (modified from (Savino et al., 1999))

2.5. Performance of Diffuser

2.5.1. Diffuser Operability

One of the important performance variables in this study was operability. At the initial stage of driving HWT, the pressure ratio of the wind tunnel increases and flow occurs inside the wind tunnel. As the pressure ratio increases further, a shock wave is generated at the nozzle throat. To start the wind tunnel, higher pressure ratio must be required to push this initial shock wave up to the diffuser throat. If a sufficient pressure ratio is not secured, or if the wind tunnel design is incorrect, such as not passing the mass flow rate, the wind tunnel will not start. Since HWT requires a high pressure ratio and strong shock waves are generated inside, this operability becomes more important issue (Agostinelli et al., 2019, 2020) and should be closely monitored compare to SWT.

Fig. 11 shows the inoperable state and operational state of the diffuser. First, inoperable state occurs when a shock wave is generated in the test section or when the diffuser fails to pass all the flow ejected from the nozzle. In this case, the back-pressure should be lowered or the design of the diffuser should be adjusted. This inoperable state is also called unstating state, and the flow at the nozzle exit becomes over-expanded because the test section pressure is high.

In operable state, the diffuser can swallow the initial shock wave and pass all the flow ejected from the nozzle. The high velocity flow is decelerated creating gradual shock waves within the diffuser. This state is also called the starting state, and the flow at the nozzle exit is under-expanded because the test section pressure is sufficiently low. In this state, desired test environment can be created, and the hypersonic test would be possible by mounting the test model.

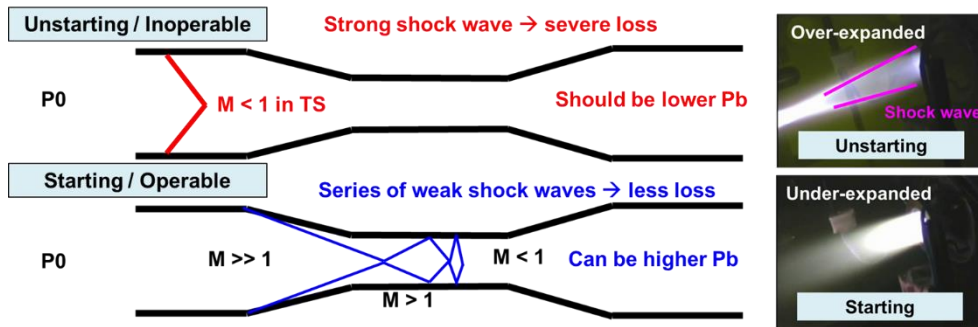


Fig. 11. Schematics of operable (up) and inoperable (down) state of diffuser

2.5.2. Diffuser Efficiency

Once HWT can be operable, it becomes highly important how efficiently and economically wind tunnel testing can be performed. A high pressure ratio is required to operate a wind tunnel, which requires a gas generator and vacuum facilities with high performance and capacity. If the diffuser is inefficient, the cost will increase significantly because high-spec facilities will be required when constructing a wind tunnel. Furthermore, high costs will be required to maintain a high pressure ratio during wind tunnel operation. In particular, since HWT requires a much higher pressure ratio than SWT and requires higher-spec facilities, the diffuser efficiency becomes much more important.

Having high diffuser efficiency implies achieving high pressure recovery. In other words, it means that a diffuser can transport the high-speed flow to the exit of the diffuser while minimizing the total pressure loss, and the back-pressure at the diffuser exit can be increased to a high level as much as the total pressure loss is minimized.

In this regard, the diffuser efficiency can be evaluated based on the operable maximum back-pressure for each diffuser shape. The diffuser efficiency can be calculated using Eq. (1) (Savino et al., 1999), where $p_{0,e}$, $p_{0,n}$, and p_b denote the total pressure at the diffuser exit, total pressure at the nozzle exit, and backpressure of the diffuser, respectively. p_{02}/p_{01} represents the ratio of total pressure before and after the normal shock wave at the reference Mach number.

In this study, the nozzle exit Mach number of 7 was selected as the reference Mach number based on the same criteria reported in previous studies (Agostinelli et al., 2019; Brune et al., 2019; Savino et al., 1999).

$$\eta = \frac{\text{Diffuser pressure ratio}}{\text{Normal shock pressure ratio}} = \frac{p_{0,e}/p_{0,n}}{p_{02}/p_{01}} \approx \frac{p_b}{p_{02}} \quad (1)$$

CHAPTER 3

METHODOLOGY

3.1. Overview

In this chapter, theoretical backgrounds used in the study are described in detail. In *3.2. Flow Analysis* section deals with the theory of computational fluid analysis performed throughout the study. The modeling methods of internal fluid of HWT and numerical methods are described. In *3.3. Surrogate Model*, various techniques used when developing the surrogate model based framework are described in detail. It deals with the DoE (Design of Experiments) based effective simulation points sampling technique, kriging model used as a surrogate model, and the reliability evaluation of the constructed surrogate model. In *3.4. Sensitivity Analysis*, the concept and types of sensitivity analysis were briefly introduced, and sensitivity analysis based on linear regression theory and variance decomposition was described. Practical elements related to how each theory is implemented are not covered in this chapter, but can be found in subsequent chapters.

3.2. Flow Analysis

3.2.1. Governing Equations

The governing equations used in the study were the axisymmetric compressible Reynolds Averaged Navier–Stokes (RANS) equations, as follows:

$$\frac{\partial Q}{\partial t} + \frac{\partial E}{\partial x} + \frac{\partial F}{\partial y} + H = \frac{\partial E_v}{\partial x} + \frac{\partial F_v}{\partial y} + H_v \quad (2)$$

$$Q = \begin{bmatrix} \rho \\ \rho u \\ \rho v \\ \rho e_t \end{bmatrix} \quad (3)$$

$$E = \begin{bmatrix} \rho u \\ \rho u^2 + p \\ \rho uv \\ (\rho e_t + p)u \end{bmatrix}, F = \begin{bmatrix} \rho v \\ \rho uv \\ \rho v^2 + p \\ (\rho e_t + p)v \end{bmatrix}, H = \frac{1}{y} \begin{bmatrix} \rho v \\ \rho uv \\ \rho v^2 \\ (\rho e_t + p)v \end{bmatrix} \quad (4)$$

$$E_v = \begin{bmatrix} 0 \\ \tau_{xx} \\ \tau_{xy} \\ u\tau_{xx} + v\tau_{xy} - q_x \end{bmatrix}, F_v = \begin{bmatrix} 0 \\ \tau_{xy} \\ \tau_{yy} \\ u\tau_{xy} + v\tau_{yy} - q_y \end{bmatrix}, H_v = \begin{bmatrix} 0 \\ (h_v)_2 \\ (h_v)_3 \\ (h_v)_4 \end{bmatrix} \quad (5)$$

$$(h_v)_2 = \tau_{xy} - \frac{2}{3} \frac{\partial}{\partial x} \left(\mu \frac{v}{y} \right) \quad (6)$$

$$(h_v)_3 = \tau_{yy} - \tau_{\theta\theta} - \frac{2}{3} \left(\mu \frac{v}{y} \right) - \frac{2}{3} y \frac{\partial}{\partial y} \left(\mu \frac{v}{y} \right) \quad (7)$$

$$(h_v)_4 = u\tau_{xy} + v\tau_{yy} + \frac{\mu}{\text{Pr}(\gamma - 1)} \frac{\partial T}{\partial y} - \frac{2}{3} \left(\mu \frac{v^2}{y} \right) - \frac{2}{3} y \frac{\partial}{\partial y} \left(\mu \frac{v^2}{y} \right) - \frac{2}{3} y \frac{\partial}{\partial y} \left(\mu \frac{uv}{y} \right) \quad (8)$$

The stress tensor and heat transfer rate are expressed as follows:

$$\tau_{ij} = \mu \left(\frac{\partial u_i}{\partial x_j} + \frac{\partial u_j}{\partial x_i} \right) + \lambda \left(\frac{\partial u_k}{\partial x_k} \right) \delta_{ij}, \quad \begin{cases} i = x, y \\ j = x, y \end{cases}, \quad \lambda = -\frac{2}{3}\mu \quad (9)$$

$$\tau_{\theta\theta} = \mu \left[-\frac{2}{3} \left(\frac{\partial u}{\partial x} + \frac{\partial v}{\partial y} \right) + \frac{4}{3} \frac{v}{y} \right] \quad (10)$$

$$\mu = \mu_l + \mu_t \quad (11)$$

$$\dot{q}_i = -\kappa \frac{\partial T}{\partial x_i} \quad (12)$$

$$\kappa = \kappa_l + \kappa_t \quad (13)$$

The second viscosity coefficient λ was determined based on Stokes' hypothesis.

3.2.2. Modeling of Thermal and Chemical Equilibrium

In the case of frozen air, where the air temperature is distributed below 600 K, the following calorically perfect gas equation shown in Eq. (14) becomes the equation of state with a constant specific heat ratio γ , and the viscosity coefficient is typically calculated based on Sutherland's law, as shown in Eqs. (15)–(16) (Sutherland, 1893):

$$p = \rho \left[e_t - \frac{1}{2} (u^2 + v^2) \right] (\gamma - 1) = \rho e (\gamma - 1) \quad (14)$$

$$\frac{\mu}{\mu_{ref}} = \left(\frac{T}{T_{ref}} \right)^{\frac{3}{2}} \frac{T_{ref} + S}{T + S}, \mu_{ref} = 1.716 \times 10^5 \text{ kg/m} \cdot \text{s} \quad (15)$$

$$T_{ref} = 273.15 \text{ K}, \quad S = 110.4 \text{ K} \quad (16)$$

When the air temperature reaches 600 K or higher, a vibrational excitation of air molecules occurs; meanwhile, when the temperature

reaches 2,000 K or higher, a chemical reaction occurs in the air (J. D. Anderson, 2006). In this high-temperature region, the state equation of a calorically perfect gas is no longer valid. In other words, the specific heat ratio γ is no longer constant, and it is a function of the two flow variables, as follows:

$$\tilde{\gamma} = \tilde{\gamma}(\rho, T) = \tilde{\gamma}(\rho, p) = \tilde{\gamma}(p, T) \quad (17)$$

In the present study, the flow temperature was distributed up to 2,500 K. It was essential for considering the vibrational energy and chemical reaction to achieve an accurate calculation. Hence, the air was modeled as a chemically reacting gas, where it was assumed to be in a state of thermal and chemical equilibrium.

To model the equilibrium state of gas, the thermodynamic properties (e.g., pressure, temperature, and enthalpy) and transport properties (e.g., viscosity and thermal conductivity) should be calculated appropriately. In general, to calculate the equilibrium properties above regardless of the gas type, calculations are to be performed based on statistical thermodynamics. However, in the case of air, it is convenient to use the established equilibrium state data. In this study, the equilibrium properties were calculated using pre-established polynomial-type fitting equations.

First, the thermodynamic properties were calculated using Eqs. (18)–(20). Pressure p is expressed as a function of density and internal energy, whereas temperature T is expressed as a function of pressure and density. Enthalpy h is expressed as a function of pressure and density (Srinivasan et al., 1181).

$$p = p(e, \rho) = \rho e(\tilde{\gamma} - 1) \quad (18)$$

$$T = T(p, \rho) \quad (19)$$

$$h = h(p, \rho) = \frac{p}{\rho} \left(\frac{\tilde{\gamma}}{\tilde{\gamma} - 1} \right) \quad (20)$$

Subsequently, the transport properties can be calculated via a similar procedure using previously established data (Gupta et al., 1991). The equilibrium transport properties were calculated using the polynomial correlation formulas shown in Eqs. (21)–(23). Each coefficient of the polynomials is tabulated based on the pressure and temperature range, as follows:

$$\mu = A_\mu + B_\mu\chi + C_\mu\chi^2 + D_\mu\chi^3 + E_\mu\chi^4 + F_\mu\chi^5 \quad (21)$$

$$k = \exp[A_K\chi^4 + B_K\chi^3 + C_K\chi^2 + D_K\chi + E_K] \quad (22)$$

$$Pr = A_{Pr} + B_{Pr}\chi + C_{Pr}\chi^2 + D_{Pr}\chi^3 + E_{Pr}\chi^4 + F_{Pr}\chi^5 \quad (23)$$

3.2.3. Modeling of Turbulence

For turbulence modeling, the standard $k - \varepsilon$ turbulence model (Jones & Launder, 1972) was used, and the relevant equations are as follows:

$$\frac{\partial(\rho k)}{\partial t} + \nabla \cdot (\rho k \vec{V}) = \nabla \cdot \left[\left(\mu_l + \frac{\mu_t}{\sigma_k} \right) \nabla k \right] - \rho \varepsilon + 2\mu_t \bar{\bar{E}} \cdot \bar{\bar{E}} \quad (24)$$

$$\begin{aligned} \frac{\partial(\rho \varepsilon)}{\partial t} + \nabla \cdot (\rho \varepsilon \vec{V}) \\ = \nabla \cdot \left[\left(\mu_l + \frac{\mu_t}{\sigma_\varepsilon} \right) \nabla \varepsilon \right] + C_1 \frac{\varepsilon}{k} 2\mu_t \bar{\bar{E}} \cdot \bar{\bar{E}} - C_2 \rho \frac{\varepsilon^2}{k} \end{aligned} \quad (25)$$

$$\mu_t = C_\mu \frac{\rho k^2}{\varepsilon} \quad (26)$$

where the typical values for the turbulent constants were used, i.e., $\sigma_k = 1.00$, $\sigma_\varepsilon = 1.30$, $C_1 = 1.44$, $C_2 = 1.92$, and $C_\mu = 0.09$. This model is suitable for a wall-bounded flow with a low Reynolds number, as in a hypersonic wind tunnel (R.S Pugazenth & Andy C. McIntosh, 2011).

3.2.4. Numerical Schemes

The governing equations were discretized using a finite volume method. The convective flux and diffusion terms were discretized using the AUSMPW+ scheme (K. H. Kim et al., 2001) and a central difference scheme, respectively. A total variation diminishing (TVD) scheme with a minmod limiter was used to achieve high-order spatial accuracy (Sweby, 1984). Furthermore, pseudo-time integration was performed to achieve convergence using the lower-upper symmetric Gauss-Seidel scheme (Yoon & Jameson, 1988). The iterations were performed until the mass flow imbalance between the inlet and exit of the diffuser was less than 1%.

3.3. Surrogate Model

3.3.1. Surrogate Modeling

Surrogate modeling (Meta modeling) technique can be considered a series of mathematical and statistical techniques that substitute a real model using the results obtained from physical or numerical experiments. In general, the real model is impossible to observe for all regions of interest, and it requires high cost and time to derive observation values, whereas the surrogate model economically and immediately predicts the value of the real model at the expense of some accuracy.

Initially, it was used only to make empirical relations from observations through physical experiments. However, it has become widely used in real model prediction, design space exploration, sensitivity analysis, and design optimization. As a related technique, a polynomial form such as RSM (Response Surface Method) or a form using a statistical method such as the kriging method exist.

To build a surrogate model, observations that are appropriately distributed in the region of interest are required, and the observations are usually calculated through experiments or numerical simulations. DoE (Design of Experiments) can be utilized to effectively determine experimental or numerical simulation points (samples). A surrogate model is created through the observations at well-selected analysis points, and it is important to select an appropriate surrogate model considering the characteristics of the problem. The reliability and efficiency of the surrogate model is highly important and must be carefully evaluated, since the prediction of real model, design space exploration, and sensitivity analysis may use the surrogate model.

3.3.2. Design of Experiments

The predictive capability and efficiency of a surrogate model is highly influenced by the distribution of sampling points (Madsen et al., 2000). Sample points should be distributed throughout the design space, and the number of samples should be appropriately determined. A larger number of samples would be better for predictive capability. However, in practice, number of samples may be limited owing to the experimental and computational expense. Therefore, a proper strategy for sampling, such as Design of Experiments (DoE) is necessary.

DoE is a rational approach to which sampling points in the design space should be explored. DoE can be divided into a factorial-based traditional method and the modern probabilistic method. The classical DoE methods were originally developed for real experiments. These methods mainly focus on elimination of random variations, regular distribution, and the boundary of the design space with overlooking the local features of the design space to some extent. The modern DoE methods usually focus on spreading the samples throughout the design space for computer simulation. The samples extracted randomly and it is efficient to explore unknown and complicate design space. In modern DoE, Monte Carlo (Hastings, 1970), LHS (Latin Hypercube Sampling) (McKay et al., 2000), etc. exist.

LHS is a stratified sampling technique in which the range of each design variable is divided into n (number of samples) parts with equal probability. And, n samples are randomly distributed into the divided parts without reduplication in any design variable. It can guarantee the same accuracy with fewer samples compared to the Monte Carlo method, and widely used for generation of surrogate model (Stein, 1987).

3.3.3. Kriging Model

The present study adopted the kriging model as a surrogate model. The kriging model was firstly developed in geostatistics (Krige, 1951), and has been widely used in various field including fluid mechanics (Ku & Jeong, 2018; Lu et al., 2018; Model & Calibration, 2021; Raul & Leifsson, 2021). The kriging model is known for being quite accurate and efficient in dealing with nonlinear and high-dimensional problems (Lu et al., 2018).

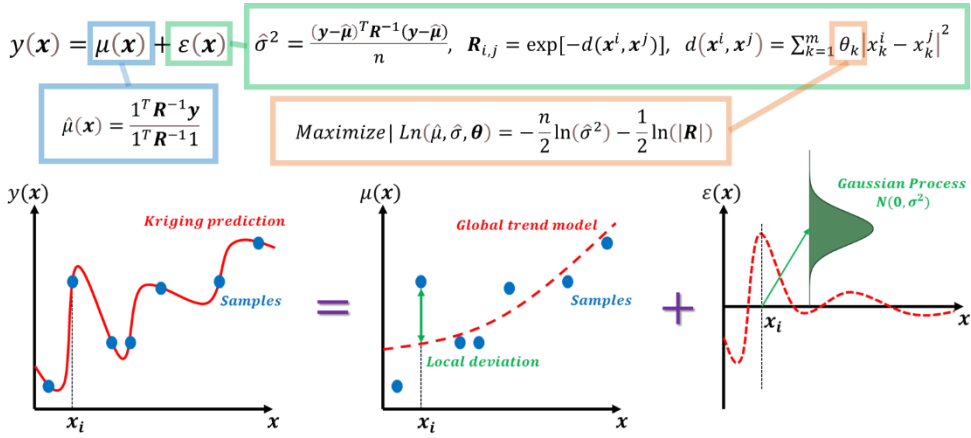


Fig. 12. Concept of kriging model

Kriging model approximates an unknown objective function at unsampled location, $y(\mathbf{x})$ by combination of a global trend model, $\mu(\mathbf{x})$ and a local deviation from the global trend, $\varepsilon(\mathbf{x})$ as follows:

$$y(\mathbf{x}) = \mu(\mathbf{x}) + \varepsilon(\mathbf{x}) \quad (27)$$

The global trend model, $\mu(\mathbf{x})$ could be constant value or response surface model depending on the type of kriging model. In the study, ordinary kriging was used and $\mu(\mathbf{x})$ was estimated value as follows:

$$\hat{\mu}(\mathbf{x}) = \frac{\mathbf{1}^T \mathbf{R}^{-1} \mathbf{y}}{\mathbf{1}^T \mathbf{R}^{-1} \mathbf{1}} \quad (28)$$

The local deviation, $\varepsilon(\mathbf{x})$ is defined as a Normalized Gaussian distribution with zero mean and the standard deviation of σ as Eq. (29). This local deviation term calibrates the local deviation from the global trend model, and can represent multiple local extrema, which makes the kriging model suitable to a complicated and non-linear design space.

$$\hat{\sigma}^2 = \frac{(\mathbf{y} - \hat{\boldsymbol{\mu}})^T \mathbf{R}^{-1} (\mathbf{y} - \hat{\boldsymbol{\mu}})}{n} \quad (29)$$

$$\mathbf{y} = [y(\mathbf{x}^1), y(\mathbf{x}^2), \dots, y(\mathbf{x}^n)] \quad (30)$$

$$\hat{\boldsymbol{\mu}} = [\hat{\mu}(\mathbf{x}^1), \hat{\mu}(\mathbf{x}^2), \dots, \hat{\mu}(\mathbf{x}^n)] \quad (31)$$

\mathbf{R} represents spatial correlation between samples. In the case of n sample points, \mathbf{R} is the $n \times n$ matrix whose (i, j) element is as follows:

$$\mathbf{R}_{i,j} = \text{Corr}[\varepsilon(\mathbf{x}^i), \varepsilon(\mathbf{x}^j)] \quad (32)$$

The elements of the covariance matrix consist of the correlation function as follows:

$$\text{Corr}[\varepsilon(\mathbf{x}^i), \varepsilon(\mathbf{x}^j)] = \exp [-d(\mathbf{x}^i, \mathbf{x}^j)] \quad (33)$$

The Gaussian distance function, d is as Eq. (34), and it has been commonly used in many applications. For each parameter, the coefficient, θ_k and the square of the distance, $|x_k^i - x_k^j|^2$ are multiplied. The smaller the distance between samples, the larger the correlation coefficient.

$$d(\mathbf{x}^i, \mathbf{x}^j) = \sum_{k=1}^m \theta_k |x_k^i - x_k^j|^2 \quad (34)$$

As a result, the ordinary kriging prediction is as follows:

$$\hat{y}(\mathbf{x}) = \hat{\mu}(\mathbf{x}) + \mathbf{r}^T \mathbf{R}^{-1}(\mathbf{y} - \hat{\boldsymbol{\mu}}) \quad (35)$$

\mathbf{r} is consist of the spatial correlation between unknown point and sample point as follows:

$$r_i(\mathbf{x}) = \text{Corr}[\varepsilon(\mathbf{x}), \varepsilon(\mathbf{x}^i)] \quad (36)$$

To calculate kriging prediction of Eq. (35), the kriging coefficients, $\boldsymbol{\theta}$ should be calculated to maximize the following likelihood function as Eq. (37) given the constraints $\boldsymbol{\theta} \geq 0$.

$$\text{Ln}(\hat{\mu}, \hat{\sigma}, \boldsymbol{\theta}) = -\frac{n}{2} \ln(\hat{\sigma}^2) - \frac{1}{2} \ln(|\mathbf{R}|) \quad (37)$$

Maximizing the likelihood function is an m-dimensional unconstrained nonlinear optimization problem. The present study used genetic algorithm (GA) (Golberg, 1989), one of global optimization methods, to solve this optimization problem.

3.3.4. Assessment of Surrogate Model

The surrogate model was evaluated to satisfy two aspects of criteria. First, for the accuracy of the surrogate model, the difference between the prediction value of surrogate model and the actual observation value was confirmed using Leave-One-Out Cross Validation (LOOCV). LOOCV remain single observation as a validation test sample point, and the other observations are used as training sample points. A surrogate model is created using these training points, and the discrepancy between surrogate model prediction and remaining test sample point is calculated. This process is repeated so that all other observations become the test point.

Based on these differences, the accuracy or error of the

surrogate model can be evaluated. Table 3 lists various commonly used matrices related to accuracy of surrogate model. In this study, RRMSE was used to evaluate the overall accuracy of the surrogate model, and RMAE was used for local evaluation.

Table 3. Various reliability assessment metrics of surrogate model

Measuring Target	Metric	Representation
Global	Mean Squared Error (RSE)	$\sum_{i=1}^n (y^i - \hat{y}^i)^2 / n$
	Normalized Root Mean Squared Error (NRMSE)	$\frac{\sqrt{\sum_{i=1}^n (y^i - \hat{y}^i)^2 / n}}{y_{max} - y_{min}}$
	Relative Root Mean Squared Error (RRMSE)	$\frac{\sqrt{\sum_{i=1}^n (y^i - \hat{y}^i)^2 / n}}{\sqrt{\sum_{i=1}^n (y^i - \bar{y})^2 / (n - 1)}}$
	Relative Average Absolute Error (RAAE)	$\frac{\sum_{i=1}^n (y^i - \hat{y}^i)^2 / n}{\sqrt{\sum_{i=1}^n (y^i - \bar{y})^2 / (n - 1)}}$
	Determination coefficient (R^2)	$1 - \frac{\sum_{i=1}^n (y^i - \hat{y}^i)^2}{\sum_{i=1}^n (y^i - \bar{y})^2}$
Local	Mean Absolute Error (MAE)	$\sum_{i=1}^n y^i - \hat{y}^i / n$
	Relative Maximum Absolute Error (RMAE)	$\max \left[\frac{ y^i - \hat{y}^i }{\sqrt{\sum_{i=1}^n (y^i - \bar{y})^2 / (n - 1)}} \right]$

As the second aspect of criteria, the convergence of the surrogate model according to the number of training points should be closely observed. This convergence evaluation is important, because (1) the convergence is a necessary for the accuracy and reliability of the surrogate model, and (2) the number of required training points can be determined based on convergence, not an arbitrary large number, to prevent wasting analysis resources and time. Specifically, the study confirmed the convergence of the accuracy metric value of the surrogate model presented above, and the convergence of the configuration of surrogate model was also confirmed by visualizing

the surrogate model as a surface. Additionally, the convergence of the sensitivity index of each design variable calculated from derived surrogate model was confirmed.

3.4. Sensitivity Analysis

3.4.1. Global Sensitivity Analysis

Sensitivity analysis is the study of how uncertainty in the output of a model (numerical or otherwise) can be apportioned to different sources of uncertainty in the model input factors (Saltelli et al., 2010). Sensitivity analysis can be divided into Local Sensitivity Analysis (LSA) and Global Sensitivity Analysis (GSA). LSA is a method of searching around a point of interest, and it is a method of observing output variables while changing only some of the entire design variables. Analysis mainly focuses on the slope at the point, and a parametric study can be said to be a type of LSA. On the other hand, GSA is interested in the entire input space, not a specific point, and observes changes in output variables according to changes in all input variables. GSA includes regression method, screening method, and variance decomposition based method.

SA is widely used in the engineering design. A design variable as an input variable and an objective function value as an output variable are generally used. Through sensitivity analysis, it is possible to identify which design variable is influential, and according to the influence on the objective function, it ranks the importance of the design variable and quantitatively evaluates the sensitivity. Conversely, it is possible to identify which variables are marginal, which are just as important as identifying influencing factors. The current design problem has a relatively large number of design variables, which increases the complexity of the model. This is the curse of dimensionality, and if too many variables are considered, the cost of the design increases, and accuracy problems such as over-parameterization may occur (van Griensven et al., 2006). Therefore, it would be essential to simplify the model by fixing the marginal factors based on SA.

The Table. 3 shows a comparison of characteristics for representative GSA methods mainly used in design. The linear regression method is a method that can be performed under the

assumption that the design variable (input variable) and the objective function value (output variable) are linear. Simple implementation is possible, calculation is fast, and sensitivity can be estimated by the slope of the derived linear regression function. However, it has the disadvantage that it is not suitable for dealing with interactions or nonlinearity between variables.

The screening method can derive the sensitivity rank of many design variables, and there is a typical Morris screening method. It can be applied to models with interactions or nonlinearity, and has the advantage that the computation cost is lower than the variance-based SA method. However, there is a disadvantage that the sensitivity cannot be quantified.

Variance based GSA calculates the sensitivity by decomposing the variance of the model. The Sobol method (I.M. Sobol, 2001) is widely used as a variance based GSA. Variance based GSA can be applied to complex and nonlinear models, and it can evaluate interaction effects between variables as well as effect of one variable. Quantitative evaluation is possible by calculating sensitivity indices. However, in order to calculate the sensitivity indices, it is necessary to perform numerous calculations on many sample points. In order to compensate for this disadvantage, various efficient sampling methods have been proposed, but the computational cost is still high compared to other methods. As can be seen from the Table. 4, as the number of input variables increases, the required calculation cost increases proportionally.

Surrogate model based GSA first constructs a surrogate model that can replace the actual model. Since the surrogate model can predict the output value at many sample points almost immediately, once the surrogate model is constructed, various sensitivity methods can be used very efficiently. Because of these advantages, many studies have been conducted using surrogate model, recently (Song et al., 2015). For classification, the method that does not use the surrogate model and obtains it through direct calculation is called the sampling based Sobol method, and the method that uses the predicted value of the surrogate model is sometimes called the surrogate model

based Sobol method.

In this study, surrogate model based GSA was used. Through this, it was possible to efficiently derive quantitative analysis and high-reliability sensitivity results even in complex models with acceptable cost. A surrogate model with high reliability was derived, and Sobol' sensitivity indices were calculated based on the immediate prediction value of this surrogate model.

Table 4. Comparison of various GSA techniques

	Linear regression	Screening	Variance base	Surrogate model base
Sampling strategy	Monte Carlo	Morris one-at-a-time sampling	Quasi-random sampling, LHS, FAST sampling	Monte Carlo, LHS, Sobol' sequence
Computational cost	n	$r(n + 1)$	$n(m + 2)$ $\sim n(2m + 2)$	n
Characteristics of Sensitivity	Quantitative	Qualitative Screening	Quantitative	Quantitative
Reliability	High	$\sim R^2$	High	High ($\sim R^2$)
Coping with interaction effect	X	0	0	0
Coping with nonlinearity	X	0	0	0

3.4.2. Linear Regression Theory

Linear regression is a useful theory (Montgomery et al., 2021) that can be applied simply under the assumption of linearity, where the distribution of dependent variable with respect to independent variable is linear.

In this study, some matrices based on the simple regression theory were used. First, in the SA, the correlation coefficient between each design variable and objective variable was calculated to check the directions of variation of objective variables with

variation of design variables. The linearity between a design variable and an objective variable was confirmed based on the coefficient of determination (R^2). Next, when evaluating the reliability of a surrogate model through the LOOCV, the degree of agreement between the predicted value of the surrogate model and the actual analysis value (goodness-of-fit) was confirmed through the coefficient of determination.

As will be discussed in detail later, the simple regression method used in this study is used for the purpose of quickly confirming the design space characteristics limitedly. Quantitative analysis in the presence of nonlinearity and multivariate will be dealt with in the next *Section, 3.4.3. variance based SA – Sobol’ indices.*

First, one tries to identify the characteristics of the population (real performance) through samples (sampled performance). The average of the samples is as follows:

$$\bar{y} = \frac{1}{n} \sum_{i=1}^n y_i \quad (38)$$

Variance is a measure of how spread out the samples are from the mean. However, the sample variance is mainly used because the population variance cannot be obtained until a fully investigations. The standard deviation is the square root of the variance, and there are also a population standard deviation and a sample standard deviation. Population variance, sample variance, population standard deviation, and sample standard deviation are sequentially expressed as follows:

$$\sigma^2 = \frac{1}{n} \sum_{i=1}^n (y_i - \mu)^2 \quad (39)$$

$$V = s^2 = \frac{1}{n-1} \sum_{i=1}^n (y_i - \bar{y})^2 \quad (40)$$

$$\sigma = \sqrt{\frac{1}{n} \sum_{i=1}^n (y_i - \mu)^2} \quad (41)$$

$$s = \sqrt{\frac{1}{n-1} \sum_{i=1}^n (y_i - \bar{y})^2} \quad (42)$$

The following is a theory on the correlation between independent and dependent variables. Again, although this method is useful for quickly identifying key characteristics of a population, it only shows the relationship between one independent variable and one dependent variable, and it has a limitation in that it is a method based on a linear assumption.

One of the indicators of correlation is covariance. Eq. (43) and (44) represent the population covariance and the sample covariance, respectively. As can be seen from the equation, if the direction of change of the independent variable and the direction of change of the dependent variable coincide with the mean, the term in sigma becomes a positive value. Conversely, if the direction of change is opposite, the term becomes a negative value. That is, if this covariance is positive, it explains a positive correlation between the two variables, and if it is negative, it explains a negative correlation. However, it cannot be used to compare the relative magnitude of correlation due to non-normalized characteristics.

$$\sigma_{xy} = \frac{\sum_{i=1}^n (x_i - \mu_x)(y_i - \mu_y)}{n} \quad (43)$$

$$s_{xy} = \frac{\sum_{i=1}^n (x_i - \bar{x})(y_i - \bar{y})}{n-1} \quad (44)$$

The correlation coefficient was devised to compensate for the limitation that covariance does not explain the magnitude of the correlation. Since the correlation coefficient is obtained by normalizing the covariance by the product of the standard deviation

of each variable, the relative magnitude of correlation can be compared using correlation coefficient. The population correlation coefficient and the sample correlation coefficient are expressed as Eq. (45) and (46), respectively. The correlation coefficient has a value between -1 and 1 , and when the coefficient value is -1 or 1 , it means that the two variables have a perfect linear relationship, and when it is 0 , there is no linear correlation. However, since correlation means linear correlation here, non-linearity cannot be captured.

$$\rho = \frac{\sigma_{xy}}{\sigma_x \sigma_y} \quad (45)$$

$$R = \frac{s_{xy}}{s_x s_y} \quad (46)$$

Normalization allows a measure of a correlation coefficient to be used for relative comparison between two correlation coefficients, but the absolute value of the correlation coefficient itself does not explain anything.

Therefore, the coefficient of determination was devised, which can indicate the magnitude of how linearly the independent variable explains the dependent variable. In addition, it can be used to evaluate the goodness-of-fit of the linear regression. The coefficient of determination is expressed as the ratio of the variation explained by the linear regression to the total variation as shown in Eq. (47). It is possible to check how much influence the independent variable has on the dependent variable. It can be interpreted that the closer to 1 , the greater the linear correlation.

$$R^2 = \frac{\sum_{i=1}^n (\hat{y}_i - \bar{y})^2}{\sum_{i=1}^n (y_i - \bar{y})^2} = 1 - \frac{\sum_{i=1}^n (y_i - \hat{y}_i)^2}{\sum_{i=1}^n (y_i - \bar{y})^2} \quad (47)$$

3.4.3. Variance based SA – Sobol' indices

A variance based global sensitivity analysis (or Sobol's SA method) (I.M. Sobol, 2001) is start from decomposition of a model

into summands of increasing dimensionality as follow:

$$y = f(\mathbf{x}) = f(x_1, x_2, \dots, x_m) \quad (48)$$

$$f(x_1, x_2, \dots, x_m) = f_0 + \sum_{i=1}^m f_i(x_i) + \sum_{i=1}^m \sum_{i < j}^m f_{ij}(x_i, x_j) + \dots + f_{1,2,\dots,m}(x_1, x_2, \dots, x_m) \quad (49)$$

Eq. (49) is called ANOVA (Analysis of Variable) representation (I.M. Sobol, 2001) given that input variables are independently and evenly distributed in a unit hypercube, and all terms in this decomposition are square integrable and orthogonal as follows:

$$\int_0^1 f_{i_1, i_2, \dots, i_s}(x_{i_1}, x_{i_2}, \dots, x_{i_s}) dx_{i_w} = 0, \quad 1 \leq i_1 < i_2 < \dots < i_s \leq m \quad (50)$$

The total number of summands in this decomposition is 2^m . f_0 represents global mean, and f_i represents the main effect of each input variables. Similarly, $f_{i,j}$ represents the combined effect or interaction effect of two input variables. The higher-dimensional terms can be explained similarly, and finally $f_{1,2,\dots,m}$ represents the interaction effect of all input variables. Each term can be calculated as follows:

$$f_0 = E(y) \quad (51)$$

$$f_i = E(y|x_i) - f_0 \quad (52)$$

$$f_{ij}(x_i, x_j) = E(y|x_i, x_j) - f_0 - f_i - f_j \quad (53)$$

The higher order interaction terms can be calculated recursively with similar way.

From the square integrable characteristics previously assumed, ANOVA decomposition can be squared and integrated over the whole

domain to give as follows:

$$\int f^2(\mathbf{x})d\mathbf{x} - f_0^2 = \sum_{s=1}^m \sum_{i_1 < \dots < i_s}^m \int f_{i_1 \dots i_s}^2 dx_{i_1} \dots dx_{i_s} \quad (54)$$

The left hand side is equal to the total variance of a model, $y = f(\mathbf{x})$, and the right hand side consists of the sum of each variance terms. So, rewriting the equation, we get the expression of the variance decomposition as follows:

$$V = Var(y) = \sum_{i=1}^m V_i + \sum_{i < j}^m V_{ij} + \dots + V_{12 \dots m} \quad (55)$$

Each term can be calculated as follows, and the higher order interaction terms can be calculated recursively with similar way.

$$V_i = Var_{x_i}[E_{x_{\sim i}}(y|x_i)] \quad (56)$$

$$V_{ij} = Var_{x_{ij}}[E_{x_{\sim ij}}(y|x_i, x_j)] - V_i - V_j \quad (57)$$

Eq. (55) shows that total variance of a model can be decomposed by the terms attributable to each input, and the interaction effects between them, under the conditions for the model to be ANOVA (Analysis of Variable) representation.

Sensitivity index can be calculated as follows by dividing the variance term of each input and interaction by the total variance. This allows us to quantify how much the variance of each factor affects the variance of the overall model.

$$S_i = \frac{V_i}{V} = \frac{Var_{x_i}[E_{x_{\sim i}}(y|x_i)]}{Var(y)} \quad (58)$$

$$S_{ij} = \frac{V_{ij}}{V} = \frac{Var_{x_{ij}}[E_{x_{\sim ij}}(y|x_i, x_j)] - V_i - V_j}{Var(y)} \quad (59)$$

In this way, higher order sensitivities can also be calculated. In addition, the sensitivity index naturally holds the following relation.

$$\sum_{i=1}^m S_i + \sum_{i < j}^m S_{ij} + \dots + S_{12\dots m} = 1 \quad (60)$$

However, calculating all sensitivity indices in the above method is not efficient, especially when there are many input variables. This is because, as mentioned above, since the total number of terms is 2^m , the number of terms to be calculated increases exponentially as the index order increases. First order sensitivity index requires the calculation of m terms, second order sensitivity index requires the calculation of $m(m-1)/2$ terms, and so on. Finally, $2^m - 1$ terms should be calculated.

To overcome this inefficiency, the total sensitivity was devised. This sensitivity evaluates all the influences including main effect of a variables, and all the interaction effects. The calculation can be done as follows:

$$S_{T_i} = \frac{E_{\mathbf{x}_{\sim i}}[\text{Var}_{\mathbf{x}_i}(Y|\mathbf{x}_{\sim i})]}{\text{Var}(y)} = 1 - \frac{\text{Var}_{\mathbf{x}_i}[E_{\mathbf{x}_i}(y|\mathbf{x}_{\sim i})]}{\text{Var}(y)} \quad (61)$$

In this way, interaction effects are naturally counted in duplicate, and in general, the sum of total sensitivity indices may be greater than 1. In the case of a purely additive model, the sum of total indices will be 1.

$$\sum_{i=1}^m S_{T_i} \geq 1 \quad (62)$$

The method of calculating the sensitivity indices depend on the characteristics of a model. First, if an analytical representation is known, it can be calculated through integration algebraically as follows:

$$f_0 = \int f(\mathbf{x}) d\mathbf{x} \quad (63)$$

$$f_i(x_i) = \int f(x) \prod_{k \neq i} dx_k - f_0 \quad (64)$$

$$f_{ij}(x_i, x_j) = \int f(x) \prod_{k \neq i, j} dx_k - f_0 - f_i(x_i) - f_j(x_j) \quad (65)$$

$$V = \int f^2(x) \prod_{k \neq i, j} dx_k - f_0^2 \quad (66)$$

$$V_i = V - \frac{1}{2} \int [f(x) - f(x_i, x'_{\sim i})]^2 dx dx_{\sim i} \quad (67)$$

$$V_{Ti} = \frac{1}{2} \int [f(x) - f(x'_i, x_{\sim i})]^2 dx dx_{\sim i} \quad (68)$$

However, there are not many cases where an accurate functional representation of the model is obtained. In this case, it can be estimated via random sampling based method as follows:

$$f_0 \approx \frac{1}{n} \sum_{k=1}^n f(\mathbf{x}_k) \quad (69)$$

$$f_i(x_i) \approx \frac{1}{n} \sum_{k \neq i} f(\mathbf{x}_k) - f_0 \quad (70)$$

$$f_{ij}(x_i, x_j) \approx \frac{1}{n} \sum_{k \neq i, j} f(\mathbf{x}_k) - f_0 - f_i - f_j \quad (71)$$

$$V \approx \frac{1}{n} \sum_{k=1}^n f^2(\mathbf{x}_k) - f_0^2 \quad (72)$$

$$V_i \approx V - \frac{1}{2n} \sum_{k=1}^n [f(\mathbf{x}_k) - f(x_{ik}, x'_{\sim ik})]^2 \quad (73)$$

$$V_{T_i} \approx \frac{1}{2n} \sum_{k=1}^n [f(\mathbf{x}_k) - f(\mathbf{x}'_{ik}, \mathbf{x}_{\sim ik})]^2 \quad (74)$$

The above equations are general forms, and there are various estimation methods for calculating these values. In order to efficiently derive the sensitivity indices in an accurate and converged form even with a small number of samples, various sampling techniques and estimation methods have been proposed. In this study, the sensitivity was calculated based on Sobol' sampling (Sobol sequence).

However, as shown in Table 4, the computational expense to calculate these indices cannot be considered efficient. Computational cost will increase drastically when the number of input variables increases and trying to compute higher-order indices. Therefore, recently, sensitivity analysis based on the surrogate model has been actively studied, and in this study, the sensitivity was calculated based on the predicted value of the surrogate model.

CHAPTER 4

GENERAL ASPECTS OF HWT

4.1. Overview

Prior to deal with the design of HWT diffuser, this chapter investigates the main aspects of HWT internal flow. Flow analysis was performed for the nozzle and diffuser of HWT, and internal flow characteristics were analyzed comprehensively.

The main points derived from this section are as follows.

(1) Prior to numerical analysis of a diffuser, the mass flow rate weighted average total pressure was proposed as an important observation variable. This observation variable was an important finding, because this variable was able to show the superiority and inferiority of the various diffuser shapes in efficiency.

(2) Through the grid convergence study, a grid that secured both accuracy and efficiency was derived. This grid later served as a reference when generating numerous calculation grids for various diffuser shapes.

(3) The nozzle–diffuser system at various back–pressures was analyzed, and axial variation of Mach number, static pressure, and total pressure were investigated.

(4) By decreasing and increasing the back–pressure step by step, the non–operational state before starting, operational state, and

the non-operational state after test was simulated. This is a typical starting process of a wind tunnel, and the hysteresis phenomenon occurred during this process was analyzed.

(5) For efficient calculation, subsequent flow analyzes in the design stage were performed by initializing with the state after the starting of the diffuser, excluding the nozzle.

4.2. Innovative Observation Variables Proposed

To derive a diffuser shape with high pressure recovery performance, the total pressure loss must be reduced across the entire diffuser. To identifying the variation of total pressure, the mass flow rate weighted average of the total pressure was proposed. Eq. (75) represents the mass flow rate weighted average of the total pressure, where ρ, u, A, P_t, \dot{m} denote the density, axial velocity, cross-sectional area, total pressure, and mass flow, respectively.

$$P_{t,avg} = \frac{1}{\int \rho u dA} \int P_t \rho u dA = \frac{1}{\dot{m}} \int P_t \rho u dA \quad (75)$$

The weighting was determined considering the essential characteristic that the diffuser flow is internal flow and the mass flow must be preserved across a duct. The average total pressure indicated the overall trend of the total pressure along the axial direction clearly and proved useful in the design stage.

Conversely, the non-averaged total pressure or the local flow variables exhibited local extrema and complicated variations. Therefore, the present study mainly used the average total pressure to find the point at which the total pressure loss was severe or negligible and the method to reduce the total pressure loss. Other averaged values, such as the average static pressure and average Mach number, were calculated with the same weightage as Eq. (76).

$$\Phi_{avg} = \frac{1}{\int \rho u dA} \int \Phi \rho u dA = \frac{1}{\dot{m}} \int \Phi \rho u dA, \quad \Phi = P_t, P, T, M, \dots \quad (76)$$

To explain the usefulness of this weighted average in more detail, in HWT, the flow ejected from the nozzle passes through the test section and model, and flows into the diffuser. A series of oblique shock waves are generated in the diffuser converging section and throat, and finally, a normal shock wave is generated and the flow becomes subsonic. The flow then exits the diffuser. Through this

process, the initially low static pressure will be recovered to a high level.

$$\frac{P_0}{P} = \left(1 + \frac{\gamma - 1}{2} M^2\right)^{\frac{\gamma}{\gamma - 1}} \quad (77)$$

Eq. (77) is an expression for the relationship between total pressure, static pressure, and Mach number in compressible flow. When the Mach number becomes 0, the static pressure equals the total pressure. Therefore, the total pressure of flow can be thought as the maximum pressure that the flow can reach at that moment. Therefore, it is important to preserve the total pressure as high as possible up to the diffuser exit for higher back-pressure. Therefore, in the HWT diffuser design, it is essential to mainly observe the total pressure.

Nevertheless, in most previous studies related to HWT diffuser, (1) internal flow pressure distribution and contour (Fig. 13), and (2) static pressure at the diffuser wall and Mach number along the axis (Figs. 14, 15) were mainly observed. In Fig. 14, Config A is a shape with low diffuser efficiency, and Config B is a shape with high diffuser efficiency. (Table. 5) The maximum back-pressure of Config A is 3,200 Pa, and the maximum back-pressure of Config B is 7,400 Pa. Although the efficiency difference is more than twice, it is difficult to capture why Config B attained high efficiency and where inefficiency occurred in Config A through the two graphs in Figs. 14, 15.

On the other hand, Fig. 16 shows the mass flow rate weighted average of the total pressure. This variable is not only intrinsic, but the variation is always in a decreasing trend, and since it is monotonous compared to the traditional observation variables, it was easier to interpret. In this graph, it was easy to capture the difference in total pressure loss between the two shapes, where the difference occurred at $x=1.5$ m in the axial direction. This mass flow weighted average variable enabled an explanatory analysis of the diffuser efficiency and allowed the focus of performance improvement works around this position.

Table 5 Diffuser shape parameters and pressure recovery of low and high efficient configurations
(Detailed descriptions for each shape parameter is given in Chapter 5)

Parameters \ Configuration		A	B
Test section	D_n [m]	0.396	0.396
	L_{sep} [m]	0.871	1.0
	Blockage [%]	40	40
Converging section	D_i [m]	1.3	1.2
	L_{cs} [m]	None	0.7
	α [deg.]	5	6
Throat	D_{t2} [m]	0.873	0.730
	L/D_{t2}	15.0	11.0
	A_{t2}/A_{t1}	700	489
Diverging section	β [deg.]	3	10
	D_e [m]	1.0	2.0
Operability		O	O
Pressure recovery	$p_{b,max}$ [Pa]	3,200	7,200
	η [%]	9.5	21.4
	Difference [%]	125	

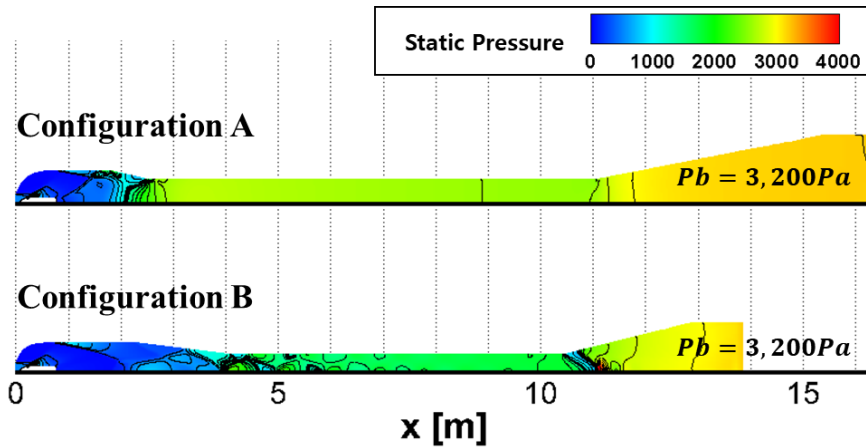


Fig. 13. Pressure distributions of configuration A (inefficient diffuser) and B (efficient diffuser)

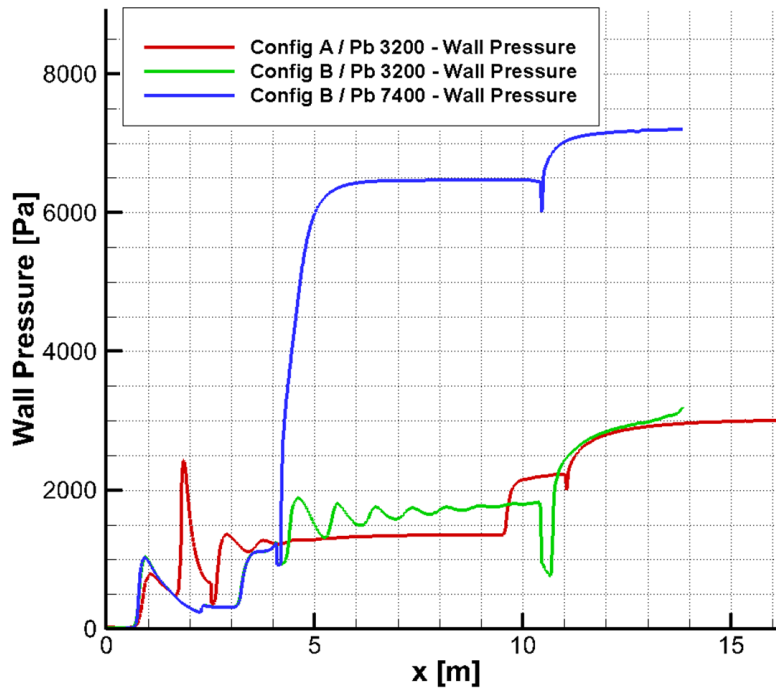


Fig. 14. Diffuser wall pressure distribution of configuration A (inefficient diffuser) and B (efficient diffuser)

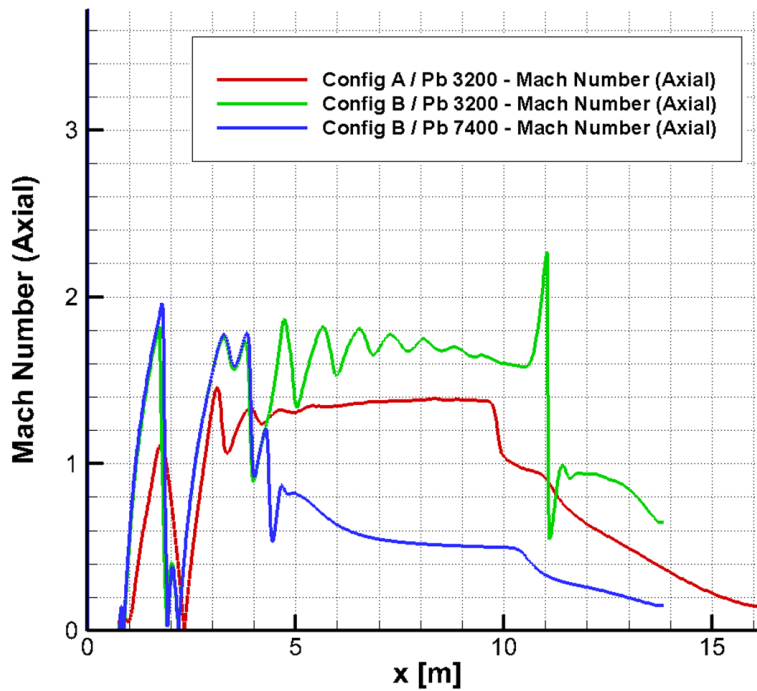


Fig. 15. Centerline Mach number distribution of configuration A (inefficient diffuser) and B (efficient diffuser)

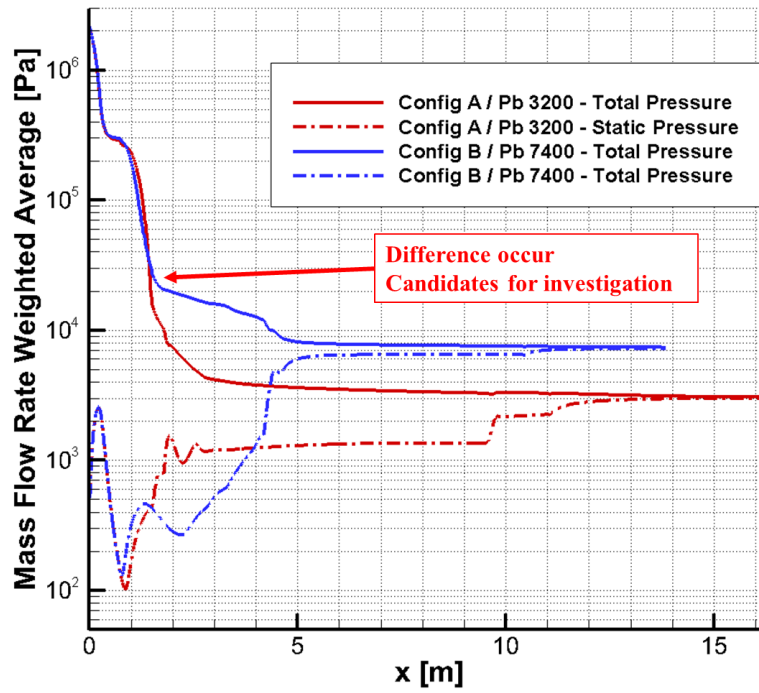


Fig. 16. Average total pressure and average static pressure along the axial direction of configuration A (inefficient diffuser) and B (efficient diffuser)

4.3. Computational Domain and Boundary Conditions

In this chapter, a flow analysis of the nozzle, test section, and diffuser of the hypersonic wind tunnel was conducted to investigate general characteristics of HWT. The length from the nozzle inlet to the exit of the diffuser was approximately 20 m, and the maximum diameter of the diffuser cross-section was 2 m. Fig. 17 illustrates the calculation domain and applied boundary conditions. The domain of the test section was set to include the outermost streamline of the ejected flow from the nozzle, wherein the flow was not affected by the test section domain despite the under-expanded condition.

The inflow conditions were determined based on the reservoir conditions of the 13 MW arc-heated scramjet test facility (AHSTF) at the NASA Langley Research Center (Witte et al., 2004). Among various reservoir conditions in the literature, the reservoir condition of Mach 7 based on flight enthalpy were used. It was assumed that the total pressure and total temperature of the reservoir were the same as those of the nozzle inlet; meanwhile, the total pressure, total temperature, and mass flow rate were calculated under this assumption and assigned as inflow conditions, as listed in Table 6.

Considering the cooling system of the hypersonic wind tunnel, a temperature wall boundary condition of 300 K was applied to the test section and diffuser wall. The back-pressure condition was applied to the diffuser exit on the far right of the domain. By controlling it, the pressure ratio of the wind tunnel was controlled.

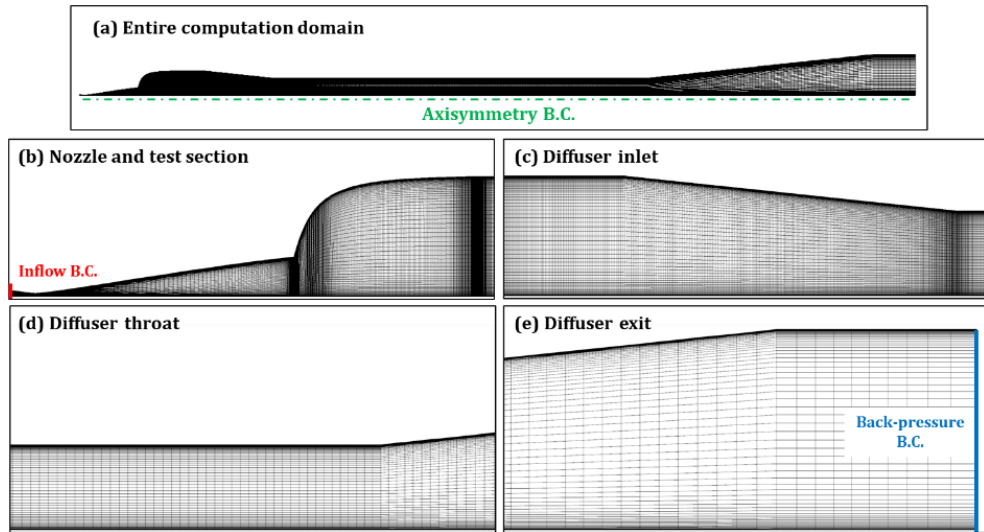


Fig. 17. Configuration of computation domain and boundary conditions applied

Table 6. Flow properties at nozzle inlet and exit

Nozzle inlet (Inflow B.C.)	P_0	28.6 bar
	T_0	2216 K
	\dot{m}	2.04 kg/s
Nozzle exit	M	7.0

4.4. Grid Convergence Study

Several grid levels were considered to determine the appropriate grid level. Through preliminary analysis, regions with large gradients of flow variables were identified, and the grid was densely distributed in these regions. The resulting grid was a coarse grid. Subsequently, a uniform refinement of the grid twice in each direction was repeated to obtain medium, fine, and very fine grids. The node dimensions of each grid are presented in Table 7.

By performing a flow analysis based on each grid, the shock wave structure, Mach number, and pressure were confirmed. As shown in Fig. 18, the shock wave structure was damped when a coarse grid was used; however, the difference in the shock wave structure was not significant when a fine grid or higher was used. Figs. 19, 20 shows the axial static pressure and Mach number for various grid levels, respectively. When the coarse grid was used, the distribution differed significantly; however, when a fine grid or higher was used, no significant difference was observed. Therefore, in this study, the fine grid level was selected considering the grid independence and computational efficiency. At this level, the y^+ of the first mesh based on the diffuser throat diameter was distributed at less than one. Computational grids in the subsequent design study were created based on the fine grid.

Table 7. Node dimensions of each grid level

Grid level	Node dimension
Coarse	378×23
Medium	756×46
Fine (selected)	1511×91
Very fine	3021×181

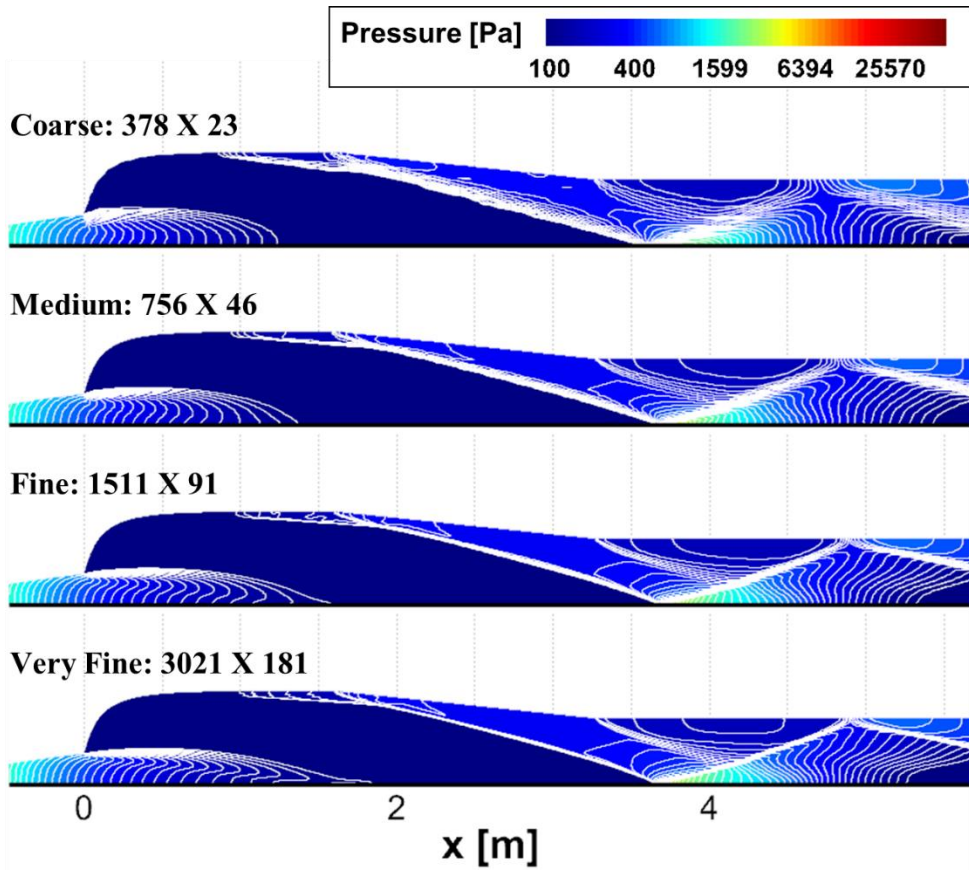


Fig. 18. Shock wave configurations at front section of domain with various grid levels

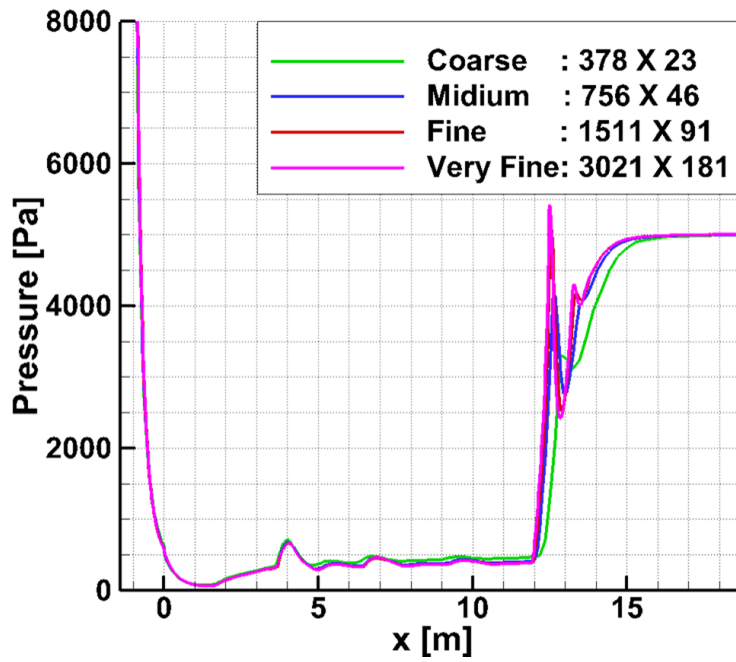


Fig. 19. Average static pressure distributions for various grid levels

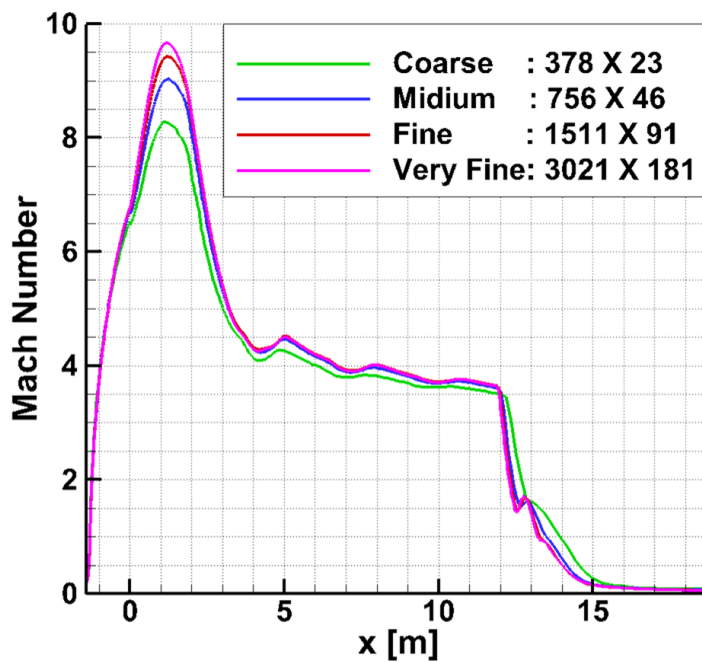


Fig. 20. Average Mach number distributions for various grid levels

4.5. Flow Characteristics of HWT

4.5.1. Flow Variation along HWT

The internal flow of HWT was analyzed under operational state. Fig. 21 shows the flow characteristics in the nozzle, test section, and diffuser at operational state with a back-pressure of 5,000 Pa. The contour at the bottom of the figure shows the distributions of the static pressure and Mach number. The flow expanded through the nozzle, and a Mach number of 10 or higher was distributed in the test section. Subsequently, a series of oblique shock waves (shock-train) was generated in the diffuser; finally, the flow became subsonic as it passed through a terminal shock wave.

The red, blue, and black lines in Fig. 21 indicates the trends of the static pressure, Mach number, and total pressure, respectively. As shown by the contour, the flow expanded through the nozzle and test section, and then compressed through the diffuser. It is noteworthy that the initially high value of the total pressure diminished rapidly as the flow passed through the HWT. Especially, a significant total pressure loss occurred owing to the first oblique shock wave generated at the inlet of the diffuser, and a rapid loss in the total pressure occurred in the terminal shock wave generated at the end of the shock-train. Subsequently, the back-pressure and total pressure became almost identical at the diffuser exit. The total pressure was additionally diminished in the nozzle and test sections owing to the boundary and shear layers. Meanwhile, the degree of total pressure loss was marginal in the subsonic region in the latter section of the diffuser.

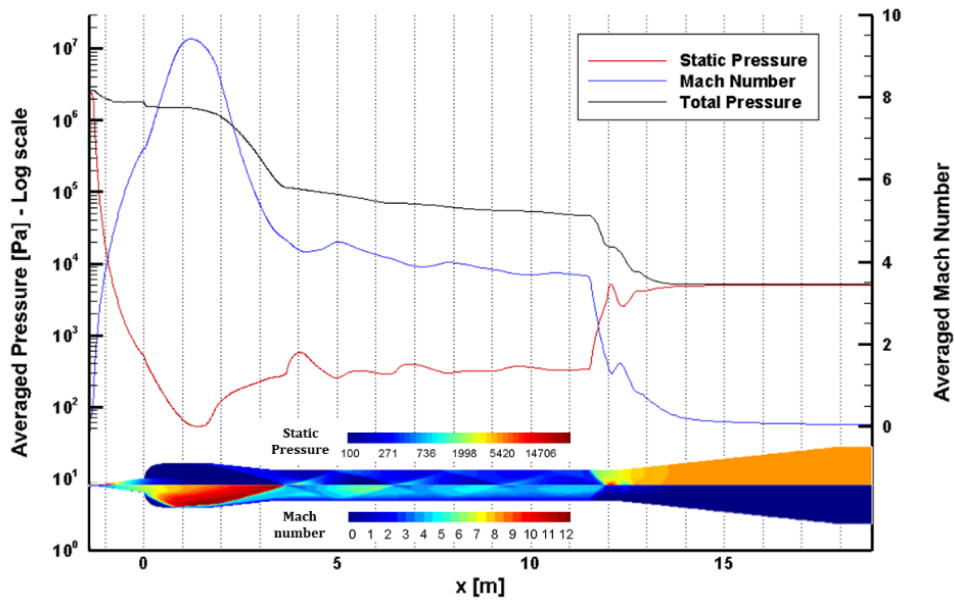


Fig. 21. Flow distributions and trends of pressure, Mach number, and total pressure

4.5.2. Starting Characteristics with Different Back-pressure

As the pressure ratio of the wind tunnel increases, in other words, as the back-pressure decreases in a fixed reservoir condition, flow occurs inside the wind tunnel. As the pressure ratio increases further, a shock wave is generated at the nozzle throat and choking occurs at the nozzle throat. To start the wind tunnel, higher pressure ratio must be required to push this initial shock wave past the test section and up to the diffuser throat. This is because the cross-sectional area of the duct will become larger at test section and diffuser compare to the nozzle, rendering internal flow expands to higher Mach number, and the shock waves at higher Mach numbers will generate higher losses. The pressure ratio must be provided to compensate this loss for wind tunnel starting.

To analyze the starting characteristics, a flow analysis was performed while changing the back-pressure step by step. Because the characteristic time of the back-pressure change is several orders of magnitude larger than the characteristic flow time, the time-dependent starting procedures can be investigated based on a

number of steady calculations (Savino et al., 1999). First, the calculation converged at a high back-pressure and then converged in stages as the back-pressure reduced until the wind tunnel started. Hence, the starting back-pressure can be determined. After the wind tunnel started, the back-pressure was increased gradually to obtain the maximum operable back-pressure.

Fig. 22 shows the pressure distribution inside the HWT for various back-pressures. Figs. 22 (a)–(d) show the results of sequential convergence while the back-pressure was decreasing; it was observed that the wind tunnel started when the back-pressure was 4,000 Pa. Subsequently, the results of sequential convergence while the back-pressure was increasing after the wind tunnel was started are presented in (e) and (f).

When the back-pressure was 10,000 Pa, a shock wave was located inside the nozzle, and as the back-pressure decreased gradually, the initial shock wave was pushed downstream. When the back-pressure was 5,000 Pa, a shock wave was generated in the test section, and the flow at the nozzle exit was not sufficiently under-expanded. Subsequently, when the back pressure reached 4,000 Pa, the shock wave was swallowed into the diffuser throat; at this time, the nozzle exit flow was completely under-expanded, and the test section pressure was maintained at a low level (wind tunnel starting state).

Once the shock wave was swallowed into the diffuser and the wind tunnel started, the wind tunnel began to be maintained even after the back-pressure was increased. As shown in Fig. 22. (f), the terminal shock wave was located inside the diffuser throat even when the back-pressure was increased to 5,600 Pa. As such, a history-dependent phenomenon appeared before and after wind tunnel starting, which is known as “hysteresis”. As shown in Figs. 22 (c) and (e), different results were obtained at the same back-pressure.

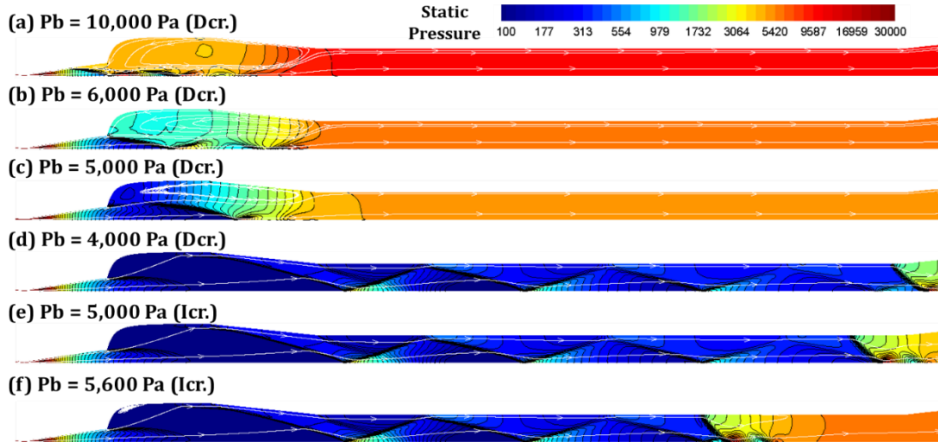


Fig. 22. Pressure distribution at different back-pressures

4.5.3. Hysteresis in Starting Process

Fig. 23 shows the test-section pressure history with respect to the various back-pressures. The result obtained while decreasing the back pressure is represented by a red line with symbols, and the result obtained by increasing the back pressure is represented by a green line with symbols. Each state in Fig. 23 is marked with a label. As shown in Fig. 23, when the back-pressure was reduced before starting, the wind tunnel started when the back-pressure was at least 4,200 Pa. After starting, it was confirmed that the starting of the wind tunnel remained even when the back-pressure was increased to 5,600 Pa. Fig. 24 clearly shows the different flow distributions before and after starting at the same back-pressure of 5,000 Pa.

As such, hysteresis occurred before and after the start of HWT. It was assumed that this occurred because when the initial shock wave was swallowed into the diffuser and a series of shock waves was generated, rendering a lower total pressure loss. As the total pressure loss reduced, the wind tunnel was able to maintain the starting state even when the back-pressure was increased. By contrast, before the wind tunnel started, a strong shock wave was generated in the test section, resulting in a relatively severe total

pressure loss and requiring a lower back-pressure to start the wind tunnel.

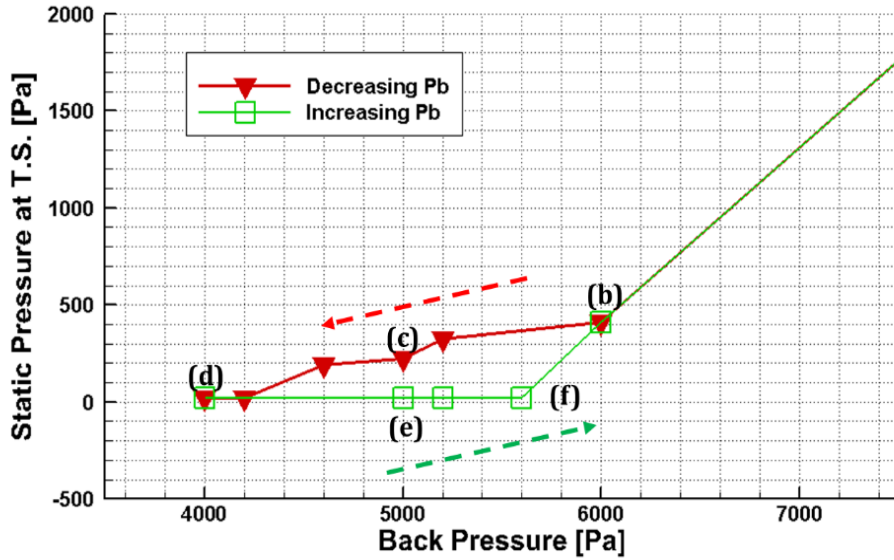


Fig. 23. Static pressure at test section ($x = 0.5$ m) based on different back-pressures applied

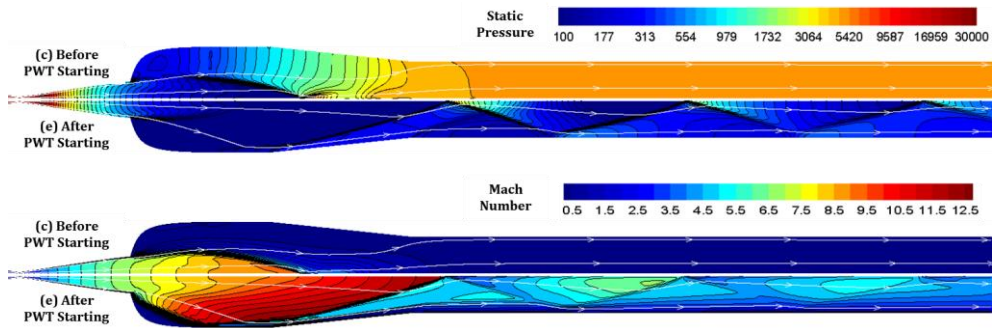


Fig. 24. Different pressure and Mach number distribution at back-pressure of 5,000 Pa

CHAPTER 5

PARAMETERIZATION AND DESIGN OBJECTIVES

5.1. Overview

In this chapter, parameterization was performed to define the shape of the HWT diffuser, and the design objectives and constraints of the diffuser design were described. The baseline diffuser shape was determined as a benchmark for performance comparison to the parametric study based diffuser design shape and the surrogate model based diffuser design shape. This baseline shape was derived by the conventional design method, and the maximum operable back-pressure was 4,000 Pa, rendering low efficiency.

5.2. HWT Diffuser Shape Parameters

Parameterization was performed to define the shape of the diffuser before designing the diffuser. Fig. 25 depicts the shape parameters of the diffuser and Table 8 summarizes their descriptions.

In parametric study based design, the parameters to be determined for designing the diffuser included the diffuser inlet diameter (D_{in}), catch-cylinder length (L_{cs}), converging half-angle (α), ratio of diffuser throat axial length to the diameter (L/D_{t2}), ratio of the diffuser throat area to the nozzle throat area (A_{t2}/A_{t1}), and diffuser diverging half-angle (β). Diffuser inlet diameter and catch-cylinder length were determined by researcher's insight without parametric study.

In surrogate model based design and sensitivity analysis, additional parameters were considered. Shape parameters considered were the separation length (L_{sep}), the diffuser inlet diameter (D_{in}), catch-cylinder length (L_{cs}), Converging half-angle (α), ratio of diffuser throat axial length to the diameter (L/D_{t2}), ratio of the diffuser throat area to the nozzle throat area (A_{t2}/A_{t1}), the diffuser diverging half-angle (β), and the diffuser inlet diameter (D_{in}).

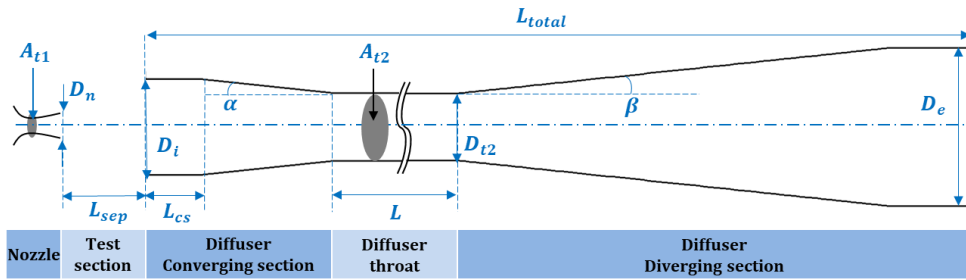


Fig. 25. Shape parameters of the diffuser

Table 8. Description of each design parameter
(PBD: Parametric study based design, SBD: Surrogate model based design)

Diffuser parts	Parameters	Description
Test section	D_n	(Fixed) Nozzle exit diameter
	L_{sep}	Nozzle–diffuser separation distance - Fixed in PBD - Variable in SBD
	Blockage	Test model frontal area to the nozzle exit area ratio
Diffuser converging section	D_i	Diffuser inlet diameter - Researcher’s decisive value in PBD - Variable in SBD
	L_{cs}	Catch-cylinder length - Researcher’s decisive value in PBD - Variable in SBD
	α	Converging half-angle of catch-cone
Diffuser throat	D_{t2}	Diffuser throat diameter
	L/D_{t2}	Diffuser throat axial length–diameter ratio
	A_{t2}/A_{t1}	Diffuser throat area to nozzle throat area ratio (AR)
Diffuser diverging section	β	Diffuser diverging half-angle
	D_e	Diffuser exit diameter - Fixed in PBD - Variable in SBD

5.3. Design Objectives and Constraints

Design objectives of the study was designing HWT diffuser shapes satisfying below:

- (1) Operable under hypersonic nozzle exit conditions with Mach number 7
- (2) Possible to test large blockage models (On–design point with test model with blockage ratio of 40 %)
- (3) Achieving the highest possible efficiency

Considering the manufacturing and experimental environments, certain parameters were under the constraints:

- (1) Nozzle configuration fixed with exit diameter (D_n) of 0.468 m
- (2) The exit diameter (D_e) cannot exceed 4 m considering heat exchanger located after the diffuser.
- (3) The total length of the diffuser (L_{total}) cannot exceed 20 m.

5.4. Baseline Configuration and its Performance

5.4.1. Baseline Configuration of Diffuser

A baseline shape was determined as a benchmark for comparing diffuser performance throughout subsequent design studies. In previous literature, each parameter was determined by arithmetic mean of existing diffuser shapes or through empirical formulas and rules of thumb. However, as previously mentioned, this method has a high risk of deriving an inoperable diffuser shape.

Therefore, prior to determination of baseline configuration, several design variables were adjusted to appropriate values. (1) The diffuser inlet diameter was adjusted to 1.3 m so that all the refracted flow from the blockage model could be sucked without using the arithmetic mean of the values of the existing shapes. (2) If the existing rules of thumb (normal shock method) is used to determine diffuser throat area, the diffuser throat area must be determined to an excessively low value. This is because it is usually used for a general supersonic wind tunnel, not for HWT, and this method does not consider the influence of a test model. Therefore, for the diffuser throat area, the median value of the parameter range from design space feasibility study, which will be dealt with in later chapter. (3) The diameter of the diffuser exit was fixed to 1 m. The value derived from the arithmetic mean of the existing shapes is 3.3m which result in the diffuser length inefficiently long. As will be explained later, since the diffuser exit diameter has little effect on the operability and efficiency of a diffuser, it is judged that this adjustment has little effect on the overall conclusion.

Table 9 presents the design parameters of baseline diffuser and the resulting pressure recovery performance. The shape first determined in the manner described above is the baseline A. Baseline A was inoperable despite the pre-adjusted excessively inappropriate values. Referring to Fig. 26, due to the excessively high converging angle in the Baseline A, the flow refracted from the model generated a strong shock wave with a high shock wave angle at the converging

section of the diffuser. A strong adverse pressure gradient appeared across this shock wave. Due to this adverse pressure gradient, flow was not effectively sucked into the diffuser, the mass flow accumulated and the test section pressure increased, rendering inoperable test state.

Baseline B was derived by alleviating the excessively high converging angle, which caused the problem of inoperability in Baseline A. In Baseline B, the magnitude of the adverse pressure gradient was also relieved due to the reduced converging angle, and the flow was successfully sucked into the diffuser throat. Therefore, the baseline shape of this study was determined as Baseline B, and performance comparison was performed with various diffuser shapes to follow based on this baseline configuration.

Table 9. Design parameters and pressure recovery performance of baseline diffuser

Parameters \ Baseline		A	B
Test section	$D_n [m]$	0.396	0.396
	$L_{sep} [m]$	0.855	0.855
	Blockage [%]	40	40
Diffuser converging section	$D_i [m]$	1.3	1.3
	$L_{cs} [m]$	None	None
	$\alpha [deg.]$	9	5
Diffuser throat	$D_{t2} [m]$	0.873	0.873
	L/D_{t2}	15	15
	A_{t2}/A_{t1}	700	700
Diffuser diverging section	$\beta [deg.]$	3	3
	$D_e [m]$	1.0	1.0
Pressure recovery	$p_{b,max} [Pa]$	Inoperable	4,000
	$\eta [\%]$	Inoperable	11.8

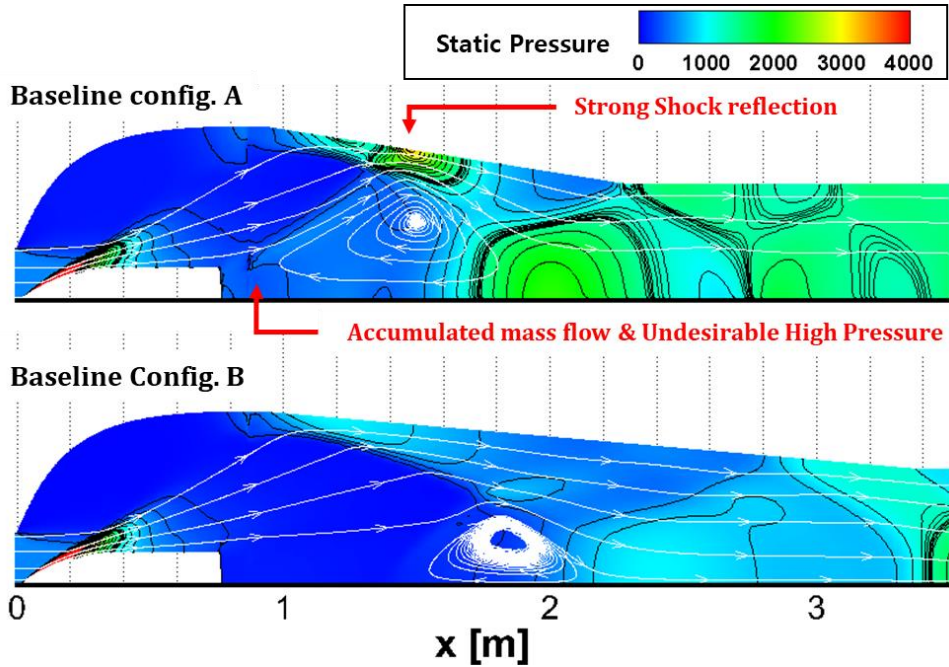


Fig. 26. Pressure distribution of the test section and initial part of the diffuser of baseline configuration A and B

5.4.2. Performance Analysis of Baseline Diffuser

The operable back-pressure range of the baseline configuration was evaluated. This performance evaluation process is necessary to determine the specifications of other parts, such as vacuum facilities and heat exchangers. Fig. 27 illustrates the pressure distributions at different back-pressure. Figs. 28 and 29 illustrate the average static pressure and average Mach number along the axial direction with different back-pressures, respectively. The terminal shock moved forward with the increasing back-pressure, and the maximum operable back-pressure was 4,000 Pa.

Although, the baseline diffuser was able to stably generate Mach 7 flow in the test section under various back-pressure conditions, these shapes were derived by adjusting some design variables to appropriate values by the researcher's know-how and insight. In addition, the maximum back pressure of 4,000 Pa and the efficiency of 11.8% are not satisfactory performance. Moreover, considering other flow disturbances in an actual test environment, the actual

operating back-pressure must be less than 4,000 Pa. The present study intended to maximize the performance through designing the shape of the diffuser through design studies based on parametric studies or design studies based on surrogate model and sensitivity analysis to be followed.

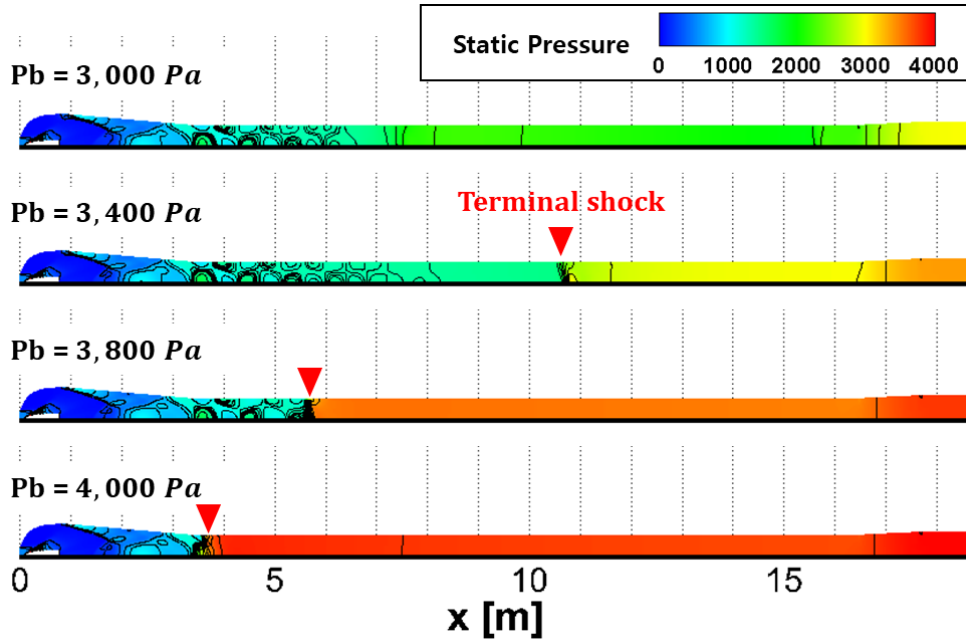


Fig. 27. Pressure distribution and terminal shock location of baseline configuration B with different back-pressures

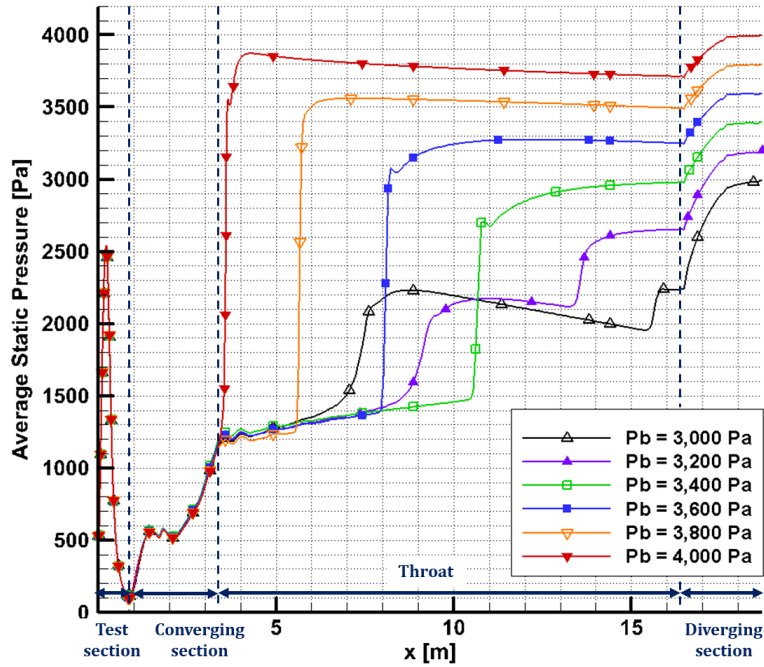


Fig. 28. Average static pressure along the axis of baseline configuration B with different back-pressures

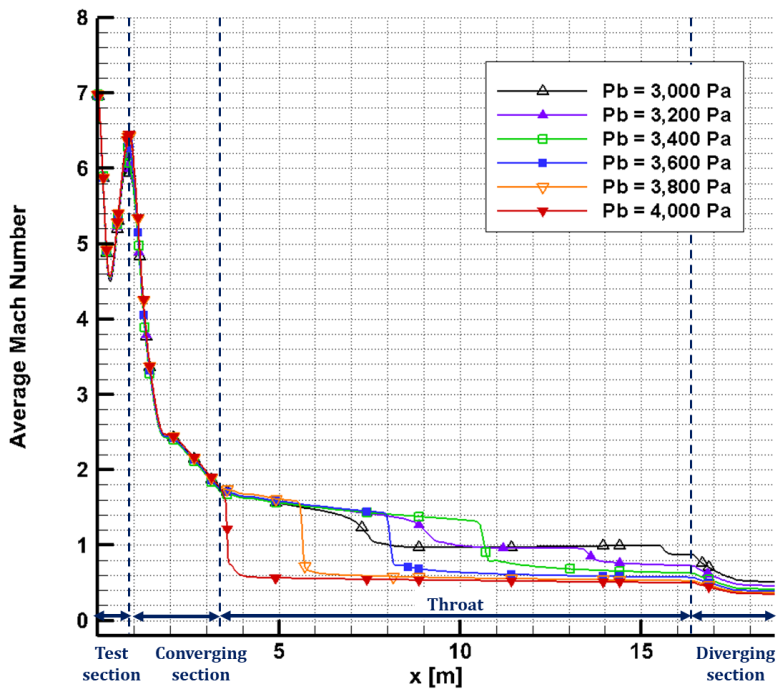


Fig. 29. Average Mach number along the axis of baseline configuration B with different back-pressures

CHAPTER 6

PARAMETRIC STUDY BASED DESIGN

6.1. Overview

In this chapter, parametric study-based design was used to determine diffuser shape variables. This chapter deals with conventional design methods and their limitations, and appropriate design variables were determined through a parametric study.

The study investigated the pressure recovery considering the blockage ratio of the test model. Subsequently, the shape parameters of the diffuser were varied considering the influence of the shape of each part, namely the diffuser converging section, throat, and diverging section, on the pressure recovery of the diffuser. Through this process, the diffuser capable of efficient testing with a large blockage model was derived, and the performance of the designed diffuser was evaluated and compared to the baseline configuration from conventional design.

The design considerations obtained from this chapter can be summarized as follows.

(1) Most of the total pressure loss occurred in the hypersonic / supersonic region and terminal shock wave, whereas the total pressure loss in the subsonic region was marginal. Thus, designing the diffuser shape in the hypersonic / supersonic region is highly important to improve the pressure recovery of the diffuser.

(2) A high degree of total pressure loss occurred when a large blockage model existed in the wind tunnel. This loss must be considered in the design stage and flow analysis should be performed including the blockage model. [*Section 6.3*]

(3) In the diffuser converging section, a shock wave generated at a high Mach number resulted in severe total pressure loss. Adjusting the shock wave intensity while changing the convergent angle can help prevent a drastic total pressure loss. Additionally, reducing the shock wave angle by placing a catch-cylinder with a constant-diameter duct at the entrance of the diffuser improved the pressure recovery significantly. [*Section 6.4*]

(4) Determination of the appropriate cross-sectional area of the diffuser throat was deemed extremely essential. Based on the characteristics of the flow inside the HWT with a high Mach number and viscous effects along with the influence of the blockage model, the cross-sectional area of the diffuser throat must be appropriately sized. An extremely small diffuser throat area may cause choking in the diffuser throat, whereas an extensively large area can increase the required pressure ratio during wind tunnel operation. Thus, a trade-off between these two factors must be considered when determining the cross-sectional area of the diffuser throat. [*Section 6.5*]

(5) The axial length of the diffuser throat should be capable of containing a shock train. However, the axial length of the diffuser throat beyond this level caused marginal effect on the pressure recovery of the diffuser. [*Section 6.6*]

6.2. Calculation Setup

6.2.1. Computational Domain

Analysis domain includes test section, dummy test model with large blockage ratio, and diffuser. (Fig. 30) Nozzles are not included for efficient calculations. The inclusion of a nozzle did not affect the prediction of maximum operable back-pressure and operability. Structured grids for various shapes were created based on the Fine grid in grid convergence study in previous chapter. Depending on the shape, grids were added in proportion to the size of a configuration. The number of grid points was approximately 100,000–150,000, and the value of y^+ was less than one.

6.2.2. Boundary Conditions

Fig. 30 illustrates the computational domain and the applied boundary conditions. An inflow condition was applied to the nozzle exit located at the far left of the domain. Table 10 lists the total pressure, P_0 , total temperature, T_0 , at the reservoir, and inflow static pressure, P , static temperature, T , Mach number, and mass flow rate, \dot{m} at the nozzle exit. These inflow values were derived by averaging the flow values at the nozzle exit in the flow analysis including nozzle in *Section 4*. The reservoir condition is identical to that of the NASA Langley 13 MW class HWT (Table 10) (Witte et al., 2004). Details are the same as in the previous *Section 4.3*. Note that this condition is representative of a HWT to simulate the high-speed flight of objects in earth's atmosphere but not representative atmospheric re-entry, characterized by much higher temperatures and lower pressure.

Considering the cooling system of a HWT, a constant temperature boundary condition of 300 K was applied to the wall of the diffuser and test section. Additionally, an adiabatic boundary condition and a constant pressure condition were applied to the walls of the model and the diffuser exit, respectively. The study controlled

the pressure ratio of the wind tunnel by varying the back–pressure under identical inflow conditions. At the beginning of the flow analysis, the starting of the HWT was simulated by lowering the back–pressure sufficiently, and the back–pressure was gradually increased by 200–300 Pa to verify the operable maximum back–pressure and efficiency of the diffuser. The iterations continued until the mass flow imbalance between the inlet and exit of the diffuser was less than 1%.

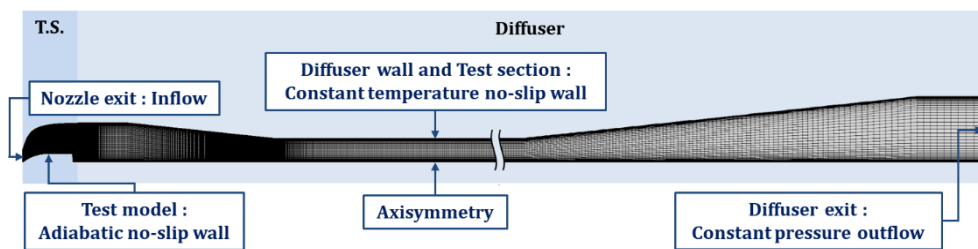


Fig. 30. Computational domain and boundary conditions

Table 10. Flow properties at the reservoir and nozzle exit

Reservoir	P_0	28.6 bar
	T_0	2216 K
Mach Number		7.0
Nozzle exit	P	530 Pa
	T	240 K
	\dot{m}	2.04 kg/s

6.3. Effect of a Blockage Model

Typically, flow analysis for diffuser design is conducted without including a test model. For the diffuser designed through this design procedure, the subsequent analysis including a test model is conducted to verify the feasibility of the wind tunnel test. However, the flow and performance of a diffuser are affected by the presence of a test model (HANUS et al., 1991; Pope & Goin, 1965) and the size of the test section (Büscher et al., 1995). Therefore, a design procedure without considering a test model can cause unexpected problems, such as low diffuser efficiency, spillage, and unstating problems, when performing a real test with a model. Thus, the analysis for diffuser design was performed along with a test model, which aided in designing an efficient diffuser in the actual test environment.

The present study adopted the ogive cylinder test model, typically used to research the flow in all regions, including the hypersonic region (Heinrich et al., 1964). The model has a fineness ratio (i.e., model length to diameter ratio) of 4.5 and a 2.5 caliber tangent nose (i.e., the model nose is part of a circle with a radius of 2.5 times the model diameter). In this study, blockage ratios of 0, 10, 20, and 40 were considered, and the on-design point was determined as blockage 40%, which is the largest size recommended for successful wind tunnel tests (Czysz, 1963). Diffuser inlet (L_{sep}) was fixed as 1 m; this comprises the maximum space for a model of 0.71 m and a free space of 0.3 m for the model support system. This test scenario can occur when a relatively large model test is required with limited resources. Additionally, a large blockage model is suitable for a conservative design. Through this conservative design, it will be possible to stably perform tests at a general level of blockage ratio of around 10%. At this level, the flow ejected from the nozzle enters the inside of the diffuser without much deflection. In particular, the higher the Mach number, the smaller the shock wave angle, so it is judged that the risk of inoperability due to model variation would be small.

The study verified the influence of the model and its blockage ratio based on the flow analysis using different blockages of the model. Fig. 31 illustrates the pressure distribution of the test section and the initial part of the diffuser. Fig. 31 (a) depicts the result without a test model, and Fig. 31 (b), (c), and (d) indicates the results with 10%, 20%, and 40% blockage test models, respectively. The other shape parameters and flow conditions were identical. In Fig. 31 (a), a sharply defined oblique shock was generated with a relatively low shock wave angle. Conversely, in Figs. 31 (b), (c), and (d), additional oblique shock waves were generated because of the model, and the flow was deflected away from the axis. Additionally, the blockage of the model and the oblique shock wave angle increased, generating a broad shock wave. These differences were prominent because the diffuser was primarily designed by changing the diffuser shape to adjust the shock wave intensity and shock angle.

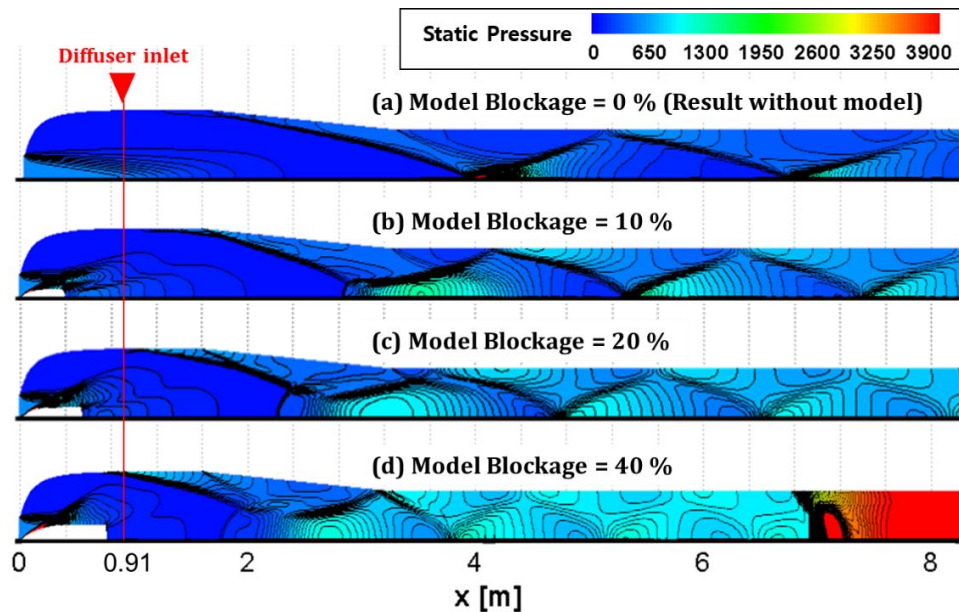


Fig. 31. Pressure distribution of the test section and initial part of the diffuser with different model blockage ratios

As the test section and diffuser inlet exhibited a high Mach

number distribution, the model influenced the total pressure loss significantly. Fig. 32 illustrates the average total pressures along the axial direction in the cases of Fig. 31. Unlike the case where the model was absent in the test section, a drastic loss was observed in the total pressure when the model was present. When the blockage ratios were 10, 20, and 40%, total pressure losses of 62, 78, and 86% occurred in the test section, respectively. Herein, the result was obtained by applying the same back-pressure of 5,000 Pa. In the absence of the model or the existence of a small blockage ratio, the total pressure was sufficiently high before the terminal shock. This indicates that a diffuser with a small blockage ratio can be operated even at a higher backpressure value.

Thus, the study verified that the blockage test model results in a rapid loss of total pressure, and the reduction in total pressure affects the diffuser efficiency adversely. In other words, the maximum operable back-pressure is lowered. Furthermore, this total pressure loss requires a larger cross-sectional area of the diffuser throat to pass the flow with lower total pressure; therefore, the test model must be considered when determining the diffuser throat area.

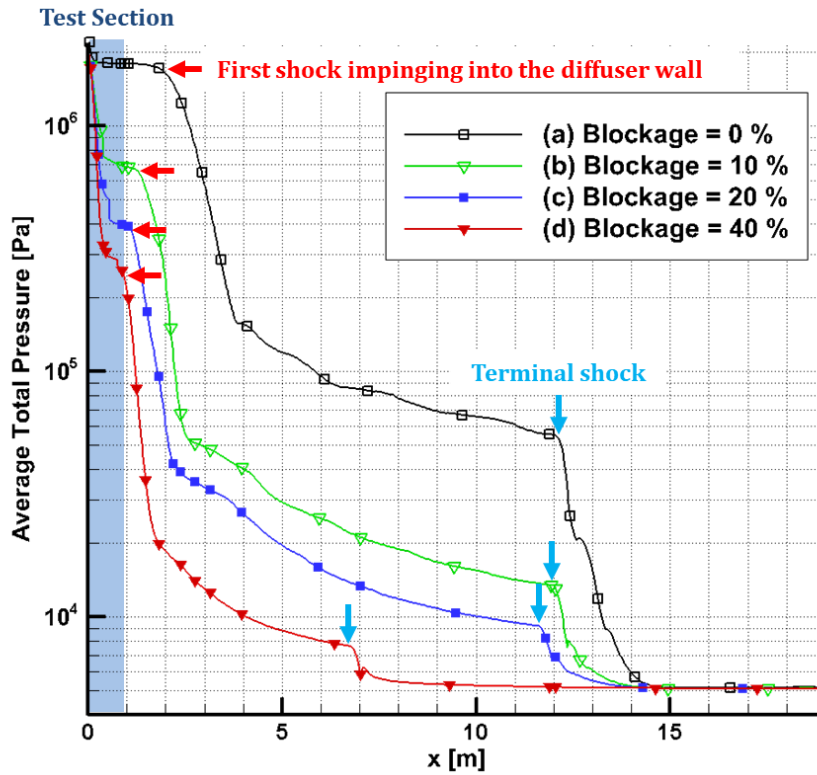


Fig. 32. Average total pressure along the axial direction with different blockage ratios

6.4. Diffuser Converging Section

The diffuser converging section is located after the test section to capture the flow ejected from the nozzle and deflected by the model. This prevents spillage of the flow and pressure rise in the test section, which can cause unfavorable effects on the nozzle flow.

The flow analysis performed based on the fixed test section size and the 40% blockage model determined that the diffuser inlet diameter must be 1.2 m to capture the deflected flow stably. Both the test section and diffuser inlet should be small as a large diffuser size can result in a higher Mach number of the flow. Shock waves generated by the flow with a high Mach number cause severe total pressure loss.

A parametric study was performed based on the determined diffuser inlet diameter with different converging half-angles of 15, 8, and 6 degrees. Furthermore, an additional shape with a constant-diameter duct, referred to as a catch-cylinder, was placed before initiating the convergence. Table 11 describes the diffuser shape parameters and the pressure recovery result of the parametric study, where all shape parameters are identical except for those of the converging section. If the converging half-angle was 8 or more, the wind tunnel could not be operated. As the converging half-angle was reduced to 6 degrees and the catch cylinder was added, the diffuser efficiency increased remarkably.

Table 11. Diffuser shape parameters and pressure recovery in parametric study for converging section

Parameters \ CASE		C1	C2	C3	C4
Test section	D_n [m]	0.396	0.396	0.396	0.396
	L_{sep} [m]	1.0	1.0	1.0	1.0
	Blockage [%]	40	40	40	40
Converging section	D_i [m]	1.2	1.2	1.2	1.2
	L_{cs} [m]	None	<i>None</i>	<i>None</i>	0.7
	α [deg.]	15	8	6	6
Throat	D_{t2} [m]	0.760	0.760	0.760	0.760
	L/D_{t2}	10.8	10.8	10.8	10.8
	A_{t2}/A_{t1}	530	530	530	530
Diverging section	β [deg.]	6	6	6	6
	D_e [m]	2.0	2.0	2.0	2.0
Pressure recovery	$p_{b,max}$ [Pa]	n/a	n/a	5,000	5,800
	η [%]	n/a	n/a	14.8	17.2

Fig. 33 illustrates the pressure distributions of representative cases in the parametric study. Especially, Fig. 33 (a) shows Case C1 for a converging half-angle of 15 degrees. The results confirmed that flow deflected by the large blockage model generated the strong oblique shock to the converging diffuser wall. Moreover, the test section pressure was higher than that of other cases. In this state, a severe loss of total pressure occurred prior to the diffuser throat and the whole mass flow ejected from the nozzle was unable to flow through the cross-sectional area of the diffuser throat. The initial shock wave was unable to be swallowed into the diffuser throat, which resulted in pressure increase in the test section. This phenomenon also occurred when the converging half-angle was 8 degrees. Thus, a larger diffuser throat cross-sectional area is required to operate the wind tunnel successfully as lowering the backpressure is insufficient.

As seen in Fig. 33 (b), the non-operational problem of higher half-angles was not present, and the maximum operable back-

pressure was 5,000 Pa, when the converging half-angle was 6 degrees. Fig 33 (c) and (d) shows the results for Case C4 with catch-cylinder with the back-pressure values of 5,000 Pa and 5,500 Pa, respectively.

The catch-cylinder was designed because previous results indicated that mitigating the first strong shock wave generated in the diffuser wall could have a strong implication in solving the inoperability problem and increasing efficiency. The catch-cylinder was placed where the flow deflected from the test model hit the diffuser wall to mitigate the intensity of the oblique shock wave generated at that position. The results verified that the diffuser could operate stably even at back-pressure of 5,500 Pa owing to the reduction of the total pressure loss by the catch-cylinder.

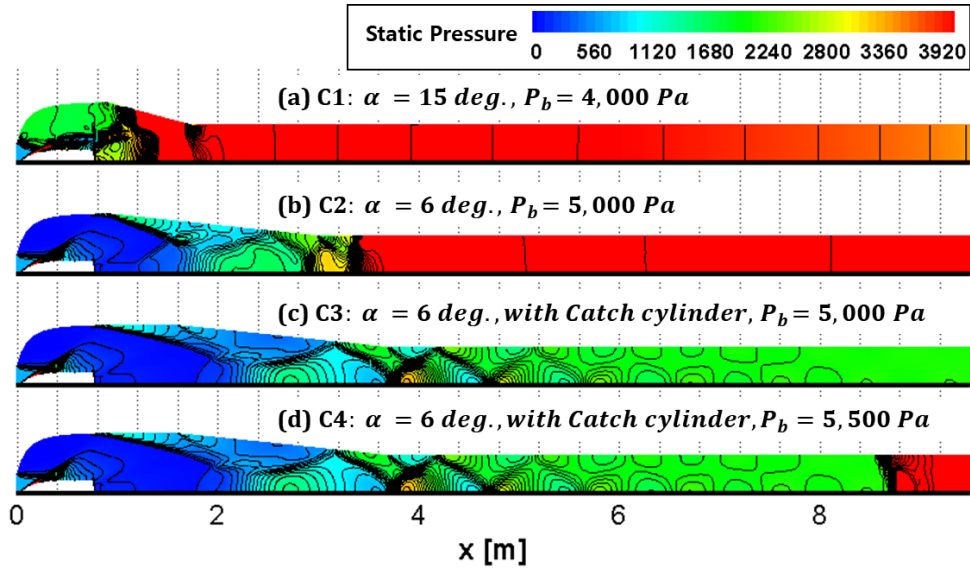


Fig. 33. Pressure distribution of the initial part of the diffuser with different converging shapes and back-pressures

Fig. 34 illustrates the variations in the average total pressure along the axial direction of the result of Fig. 33. Except for the inoperable case with 15 degrees of convergence, the total pressure trends were identical until the first oblique shock was generated at approximately $x = 1 \text{ m}$ on the diffuser wall. Results (a) and (b) in Fig. 34 verify that severe total pressure losses occurred owing to the

first oblique shock generated from the diffuser wall. Results (c) and (d) in Fig. 34 represent the outcome of using catch-cylinders. Herein, the total pressure loss reduced significantly and the HWT was operated even at higher backpressure values than those of other cases.

The results indicate that the diffuser converging section exhibits a high Mach number distribution and a severe total pressure loss owing to the oblique shock wave. Hence, reducing the total pressure loss in this section seems to be the key to increasing diffuser efficiency. Additionally, placing the catch-cylinder in the appropriate location where the first oblique shock wave occurs on the wall of the diffuser can improve the diffuser efficiency significantly. Thus, the derived diffuser shape was determined by adding a catch-cylinder to a 6° converging half-angle. The aforementioned consideration is considered important, so it would be valuable to test it experimentally. In addition, it would be valuable to verify this for other flow conditions, including higher temperature conditions, and for more diverse geometries.

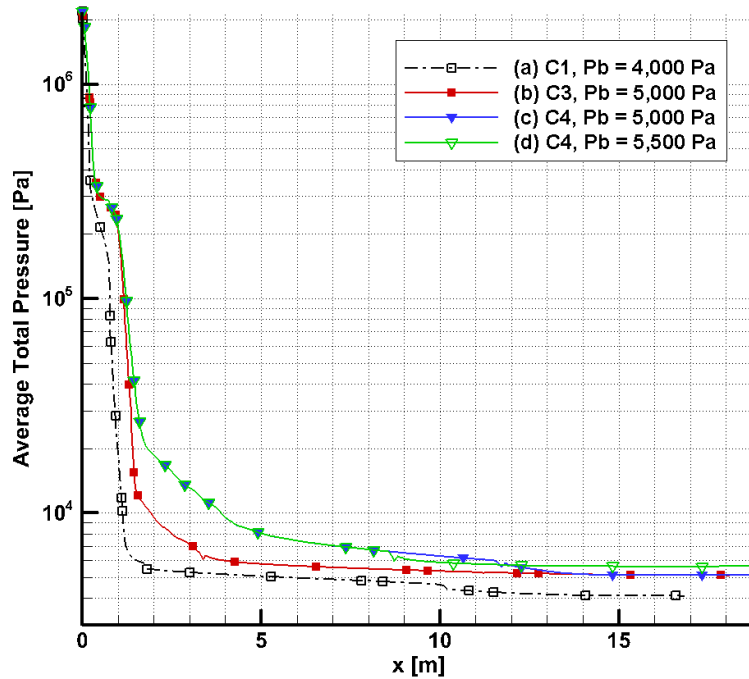


Fig. 34. Average total pressure along the axial direction for different converging shapes and back-pressures

6.5. Cross Sectional Area of the Diffuser Throat

Several studies have briefly reported the importance of the cross-sectional area of the diffuser throat (J. Anderson, 2011; Monnerie, 1967; R.S Pugazenthi & Andy C. McIntosh, 2011). The study conducted a parametric study to analyze the effect of the diffuser throat area to nozzle throat area ratio (AR) on the efficiency of the diffuser and the starting of the hypersonic wind tunnel.

In a HWT, the diffuser throat is secondary to the nozzle throat and must pass all the flow ejected from the nozzle. The flow inside the wind tunnel can be simplified to a quasi-one-dimensional flow (J. Anderson, 2011), and the mass flow rate inside the wind tunnel can be expressed using Eq. (78). Herein, A^* denotes the cross-sectional area under sonic conditions and is the minimum cross-sectional area required for a fixed mass flow rate under a specific total flow condition. T_0 denotes the total temperature, P_0 represents the total pressure, \dot{m} indicates the mass flow rate, γ denotes the specific heat ratio, and R represents the specific gas constant.

$$\dot{m} = A^* \frac{P_0}{\sqrt{T_0}} \sqrt{\frac{\gamma}{R} \left(\frac{2}{\gamma + 1} \right)^{\frac{\gamma+1}{\gamma-1}}} \quad (78)$$

As indicated in Eq. (78), the mass flow rate is proportional to A^* and P_0 . In a well-operated steady state HWT, A^* becomes the cross-sectional area of the nozzle throat. As the flow passing through the nozzle and diffuser loses the total pressure owing to shock waves and friction, the cross-sectional area of the diffuser throat must be larger than that of the nozzle throat; otherwise, the diffuser may choke and not pass the mass flow rate ejected from the nozzle completely (J. Anderson, 2011). The ratio of the cross-sectional area of the diffuser throat to the nozzle throat area can be expressed using Eq. (79). Herein, subscripts 1 and 2 denote the states in the nozzle and diffuser, respectively, whereas A_t represent the throat area. The change in total temperature is marginal in

comparison with that of the total pressure; therefore, it can be approximated using the ratio of the total pressure.

$$\frac{A_{t2}}{A_{t1}} \geq \frac{P_{01}}{P_{02}} \frac{\sqrt{T_{02}}}{\sqrt{T_{01}}} \approx \frac{P_{01}}{P_{02}} \quad (79)$$

In the design stage, Eq. (79) is a prerequisite for determining the cross-sectional area of the diffuser throat. Typically, the value of A_{t2} is estimated using the normal shock wave relation (J. Anderson, 2011; R.S Pugazenthi & Andy C. McIntosh, 2011) as the total pressure ratio on the right-hand side of the equation remains unknown until the actual operation of the HWT. In this estimation, the total pressure ratio is assumed to be equal to the ratio of total pressure across a normal shock at the diffuser inlet Mach number, as indicated in Eq. (80), where M_1 denotes the inlet Mach number and s represents the entropy.

$$\frac{p_{02}}{p_{01}} = e^{-(s_2-s_1)/R},$$

$$\frac{s_2 - s_1}{R} = \frac{1}{\gamma - 1} \ln \left[\frac{2\gamma M_1^2}{\gamma + 1} - \frac{\gamma - 1}{\gamma + 1} \right] + \frac{\gamma}{\gamma - 1} \ln \left[\frac{2 + (\gamma - 1)M_1^2}{(\gamma + 1)M_1^2} \right] \quad (80)$$

However, this estimation is typically used in a supersonic environment. In a real hypersonic environment where the values of the total temperature are high, and the values of the specific heat ratio change, there is no guarantee that extension is possible. Furthermore, the flow inside the hypersonic wind tunnel exhibits a high Mach number and a severe viscous effect. Thus, the estimation using the normal shock wave relation may underestimate the minimum cross-sectional area (R.S Pugazenthi & Andy C. McIntosh, 2011). Additionally, the total pressure loss increased when the model was installed and a larger diffuser throat area was required. Even if we used a conservative value for a specific heat ratio of 1.3 and a nozzle exit Mach number of 7, the minimum cross-sectional area of the diffuser throat predicted using the normal shock wave relation

was 164 times that of the nozzle throat. However, the flow analysis with the 40% blockage model performed using computational methods indicated that the diffuser did not choke when the throat area was more than 445 times the nozzle throat cross-sectional area. Thus, we concluded that applying the normal shock wave relation to a HWT diffuser with a large blockage model can be extremely risky.

Table 12 lists the diffuser shape parameters and the pressure recovery in the parametric study for the diffuser throat area, where all shape parameters are identical except for those of the diffuser throat. Case A1 with an AR of 400 was inoperable, and the diffuser efficiency tended to decrease as AR increased.

Table 12. Diffuser shape parameters and pressure recovery in the parametric study for the diffuser throat area

Parameters \ CASE		A1	A2	A3	A4	A5
Test section	D_n [m]	0.396	0.396	0.396	0.396	0.396
	L_{sep} [m]	1.0	1.0	1.0	1.0	1.0
	Blockage [%]	40	40	40	40	40
Converging section	D_i [m]	1.2	1.2	1.2	1.2	1.2
	L_{cs} [m]	0.7	0.7	0.7	0.7	0.7
	α [deg.]	6	6	6	6	6
Throat	D_{t2} [m]	0.660	0.696	0.730	0.760	0.800
	L/D_{t2}	11.0	11.0	11.0	11.0	11.0
	A_{t2}/A_{t1}	400	445	489	530	588
Diverging section	β [deg.]	6	6	6	6	6
	D_e [m]	2.0	2.0	2.0	2.0	2.0
Pressure recovery	$p_{b,max}$ [Pa]	n/a	6,500	6,300	5,800	5,500
	η [%]	n/a	19.3	18.7	17.2	16.6

Fig. 35 depicts the intermediate result of A1 with AR of 400. Although the AR is substantially larger than the predicted value using the normal shock wave relation, the diffuser cannot pass the whole flow ejected from the nozzle. In this case, a steady solution with Mach 7 flow in the test section was not obtained despite decreasing the

value of the backpressure sufficiently. To solve this problem, it was necessary to increase the AR or to reduce the total pressure loss that occurs before the flow reaches the diffuser throat.

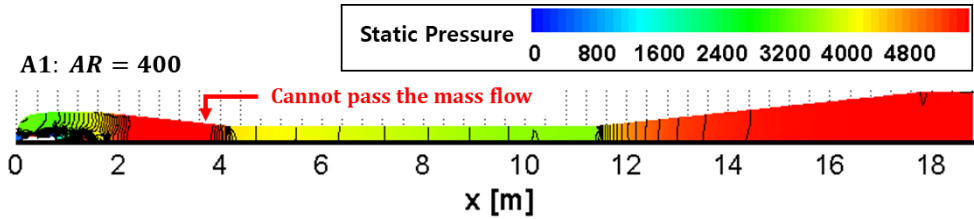


Fig. 35. Intermediate result of pressure distribution with area ratio (AR) of 400 at a back-pressure of 5,500 Pa

Fig. 36 illustrates the pressure distribution and terminal shock location of the diffuser for different values of AR under a backpressure value of 5,500 Pa. Fig. 36 (a), (b), (c), and (d) depicts the results when the values of AR are 445, 489, 530, and 590, respectively. The terminal shock was located upstream and the diffuser shows lower efficiency as AR increases. This can be attributed to the expansion of the flow owing to the larger cross-sectional area, which directly prevented the compression of the flow and generated shock waves at a higher Mach number. Moreover, the total pressure loss of the terminal shock occurring in a larger duct of the diffuser throat was severe, and a lower backpressure value (higher pressure ratio) was required to maintain the terminal shock wave swallowed into the diffuser throat. Fig. 37 illustrates the average Mach number along the axial direction of diffusers with different values of AR at a back-pressure of 5,500 Pa. As indicated in the figure, the higher the AR, the higher the Mach number is distributed, and the terminal shock wave occurs at the higher Mach number. Fig. 38 depicts the average total pressure along the axial direction of the diffuser with different values of AR at a back-pressure of 5,500 Pa. As the AR increased, the total pressure loss occurring in the terminal shock increased, which generated the terminal shock wave further upstream.

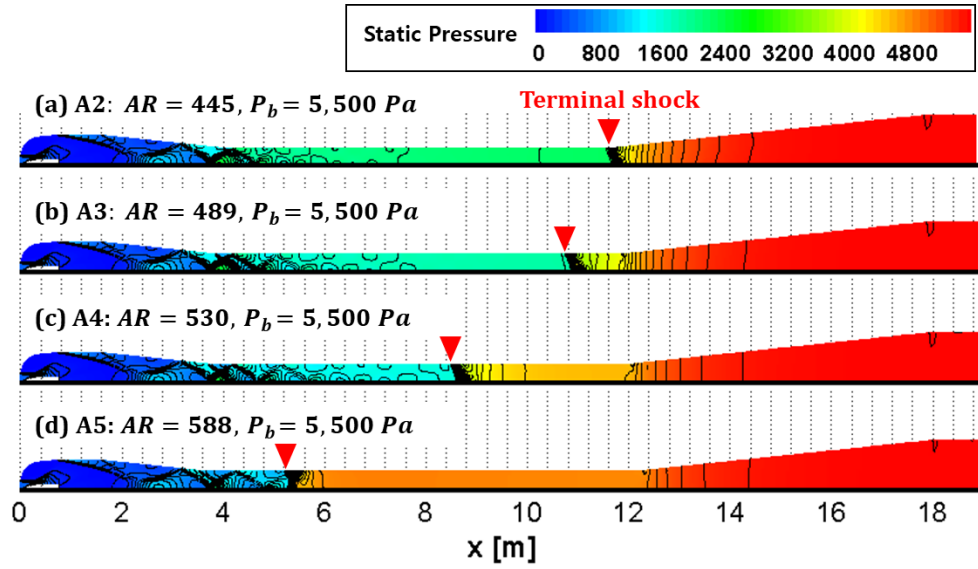


Fig. 36. Pressure distribution and terminal shock location with different values of area ratio (AR) at a back-pressure of 5,500 Pa

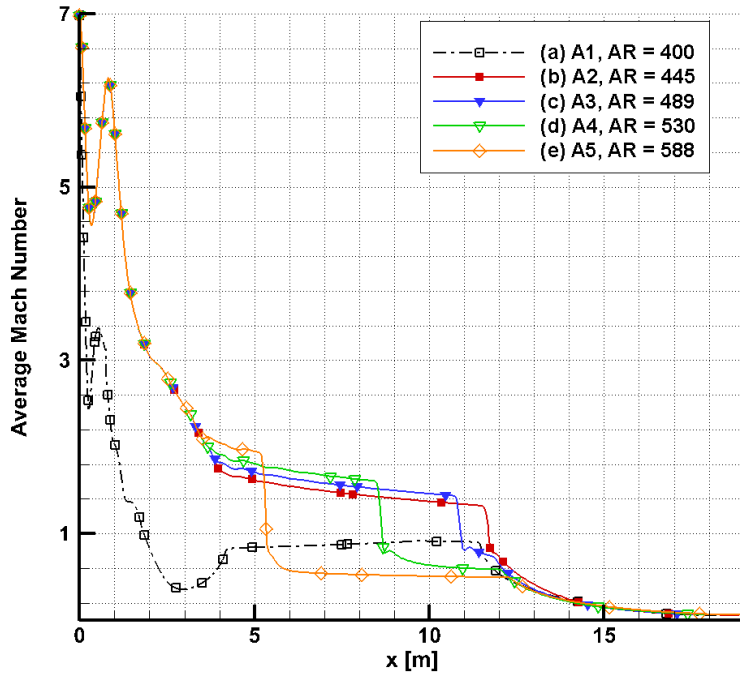


Fig. 37. Average Mach number along the axial direction for different values of throat area ratio (AR) at a back-pressure of 5,500 Pa

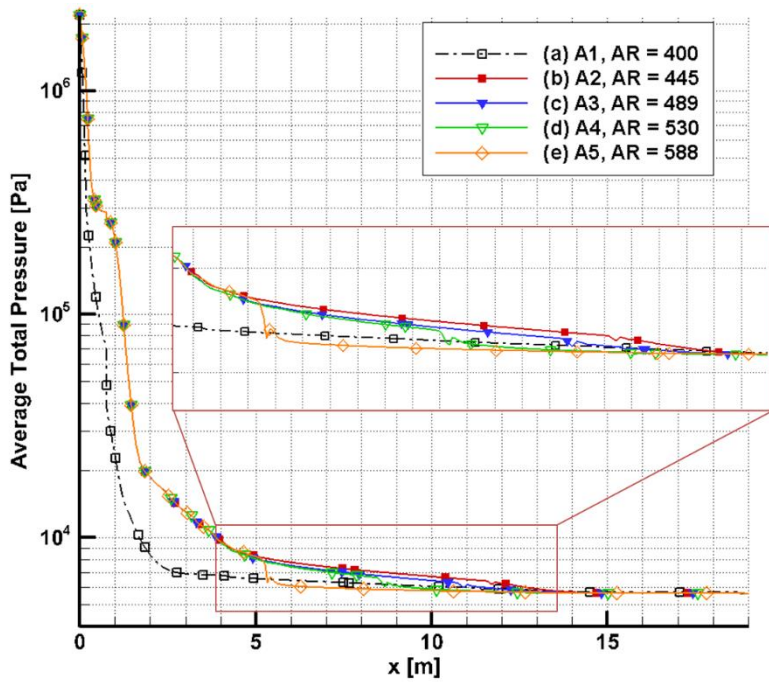


Fig. 38. Average total pressure along the axial direction for different values of area ratio (AR) at a back-pressure of 5,500 Pa

The aforementioned results indicate that reducing the AR to a level where the diffuser choke does not occur affects the diffuser efficiency positively. However, when a diffuser is designed with a low AR for high efficiency, there is a risk of choking if the model size is increased or the flow conditions are changed. Conversely, if the AR is designed to be large to reduce the risk of choking, the efficiency of the diffuser reduces considerably. Therefore, the purpose of the HWT design must be considered before determining the AR. In this study, AR was determined as 489, considering the safety margin to prevent choking while producing as high efficiency as possible. Additionally, the optimal AR prediction through numerical analysis still has accuracy limitations in the design stage, and the optimal AR, based on the current knowledge, should be confirmed experimentally. Therefore, a HWT, able to easily and low-cost replace the diffuser, would be helpful in a subsequent optimization phase.

6.6. Axial Length of the Diffuser Throat

In the diffuser throat, a series of shock waves (shock train) occurs compressing the flow. The axial length of the diffuser throat is required to contain this entire shock train (R.S Pugazenthi & Andy C. McIntosh, 2011). The length of a shock train can be algebraically expressed as a function of the Mach number, pressure ratio, Reynolds number, and momentum boundary layer thickness of a duct (Waltrup & Billig, 1973). However, estimating these values at the design stage is challenging. In this case, a numerical method can be used to predict the shock train length and determine the desired axial length of a diffuser.

To investigate the effect of the axial length of the diffuser throat on the pressure recovery, a parametric study was performed considering L/D_{t2} values of 7, 11, 13, and 17. Table 13 lists the diffuser shape parameters and the pressure recovery in the parametric study for diffuser throat length, where L/D_{t2} was adjusted by varying the axial length of the diffuser throat and maintaining the diffuser throat diameter and the other design parameters constant. Despite the large difference in L/D_{t2} by more than twice, the diffuser efficiency difference due to the length of diffuser throat was insignificant.

Table 13. Diffuser shape parameters and pressure recovery for the parametric study of throat length

Parameters \ CASE		L1	L2	L3	L4
Test section	D_n [m]	0.396	0.396	0.396	0.396
	L_{sep} [m]	1.0	1.0	1.0	1.0
	Blockage [%]	40	40	40	40
Converging section	D_i [m]	1.2	1.2	1.2	1.2
	L_{cs} [m]	0.7	0.7	0.7	0.7
	α [deg.]	6	6	6	6
Throat	D_{t2} [m]	0.730	0.730	0.730	0.730
	L/D_{t2}	7.0	11.0	13.0	17.0
	A_{t2}/A_{t1}	489	489	489	489
Diverging section	β [deg.]	6	6	6	6
	D_e [m]	2.0	2.0	2.0	2.0
Pressure recovery	$p_{b,max}$ [Pa]	6,300	6,300	6,300	6,000
	η [%]	18.7	18.7	18.7	17.8

Fig. 39 illustrates the pressure distribution and terminal shock location for each value of L/D_{t2} with a backpressure of 5,500 Pa. Fig. 40 depicts the average total pressure along the axial direction for these cases. When $L/D_{t2} = 7$, the shock train was not entirely developed owing to the insufficient axial length of the diffuser throat. This resulted in a stronger terminal shock. However, when the backpressure was further increased, and the terminal shock moved upstream further, the terminal shock wave position was formed similar to the case with a higher L/D_{t2} . When L/D_{t2} was 11 and 13, the shock train developed completely. In these two cases, the positions of the terminal shock waves are nearly identical. When the diffuser throat contained the shock train, the variation in the axial length did not affect the flow structure and pressure recovery significantly. When the axial length of the diffuser throat was increased further ($L/D_{t2} = 17$), little changes observed in the terminal shock pushed it forward. As the backpressure was gradually increased, the terminal shock moved forward gradually, and Case L4

reached the inoperable state at the lowest backpressure among the four cases even though presenting a small difference. The reason can be the additional total pressure loss due to the friction and heat transfer in the extended subsonic region.

It was not possible to confirm the optimal value of L/D through this parametric study. However, when the axial length of the diffuser throat was beyond the shock train length, the effect of the change in throat length was insignificant. This is because most of the total pressure loss occurred in the hypersonic / supersonic region (Fig. 40) owing to shock waves, regardless of the shape in which the subsonic region was distributed. In contrast, it was confirmed that the unnecessarily long throat length of the diffuser caused secondary total pressure loss and decreased diffuser efficiency.

Therefore, the diffuser throat length was determined to be sufficiently long to contain the shock train. In addition, the length was determined not to be beyond the terminal shock based on the operating backpressure. This can prevent secondary losses that occur in the subsonic region and reduce unnecessary construction and operational costs of the hypersonic wind tunnel.

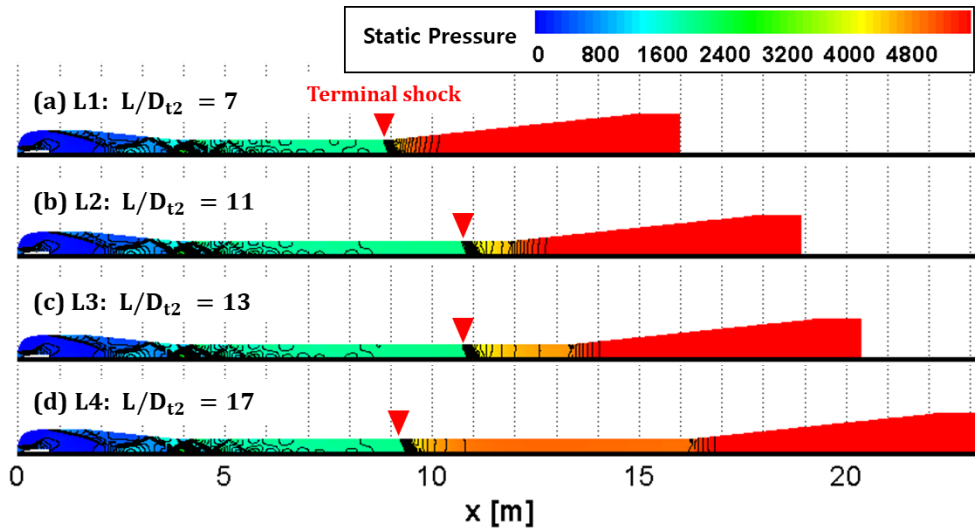


Fig. 39. Pressure distribution and terminal shock location with different values of L/D_{t2} at a backpressure of 5,500 Pa

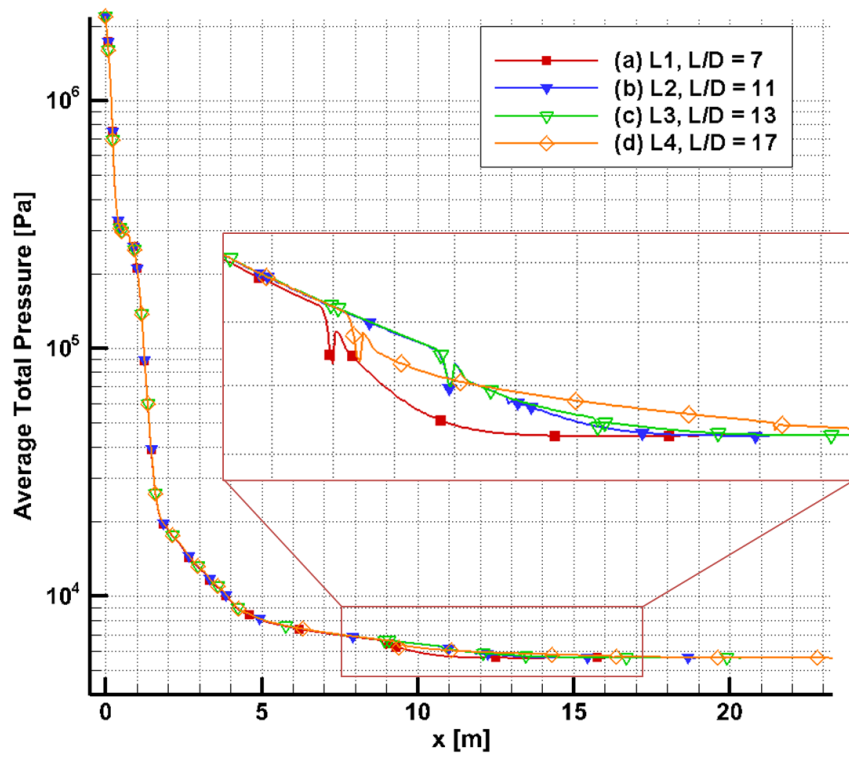


Fig. 40. Average total pressure along the axial direction with different values of L/D_{t2}

6.7. Diffuser Diverging Section

The diffuser diverging section is a divergent conical duct following the diffuser throat. It is referred to as the subsonic diffuser. In this section, the flow decelerates and the compression progresses with the increasing cross-sectional area of the duct. Typically, the design of the diffuser diverging section relies on the conditions required at the diffuser exit (flow velocity, pressure, and temperature), the occurrence of the flow separation, and the diffuser length constraint. Although increasing the angle of divergence can reduce the length of the diffuser and minimize expenses, flow separation may occur at the diffuser exit.

Table 14 lists the diffuser shape parameters and the pressure recovery in the parametric study for diverging half-angle, considering β values of 15, 10, and 6 degrees. The diffuser efficiency difference due to diverging half-angle was insignificant.

Table 14. Diffuser shape parameters and pressure recovery in the parametric study for diverging half-angle

Parameters \ CASE		D1	D2	D3
Test section	$D_n [m]$	0.396	0.396	0.396
	$L_{sep} [m]$	1.0	1.0	1.0
	Blockage [%]	40	40	40
Converging section	$D_i [m]$	1.2	1.2	1.2
	$L_{cs} [m]$	0.7	0.7	0.7
	$\alpha [deg.]$	6	6	6
Throat	$D_{t2} [m]$	0.730	0.730	0.730
	L/D_{t2}	11.0	11.0	11.0
	A_{t2}/A_{t1}	489	489	489
Diverging section	$\beta [deg.]$	15	10	6
	$D_e [m]$	2.0	2.0	2.0
Pressure recovery	$p_{b,max} [Pa]$	6,300	6,300	6,300
	$\eta [\%]$	18.7	18.7	18.7

Fig. 41 depicts the streamlines and axial velocity distributions in the diverging section at different diverging half-angles at a backpressure of 5,000 Pa. Based on the design constraint described in *Section 2.1*, the diameter of the diffuser exit was maintained constant at 2 m, resulting in different total lengths for each diverging half-angle. As illustrated in Fig. 41 (a), an excessively large diverging half-angle results in a rapid change in the cross-sectional area and a high adverse pressure gradient. This causes flow separation near the diffuser wall. The streamlines in the result indicate that recirculation occurred over a reasonably wide range, which resulted in a non-uniform velocity distribution at the diffuser exit and reduced the effective cross-sectional area through which the flow could pass. This affected the pressure recovery of the diffuser (Yang et al., 2020) and the performance of the heat exchanger installed after the diffuser adversely.

Nevertheless, the shape of the diffuser diverging section exhibited a relatively marginal effect on the pressure recovery performance of the diffuser. Moreover, the change in shape in the subsonic region hardly affected the pressure recovery as stated in *Section 3.5*. Therefore, the diverging half-angle of the diffuser was determined to avoid the occurrence of flow separation.

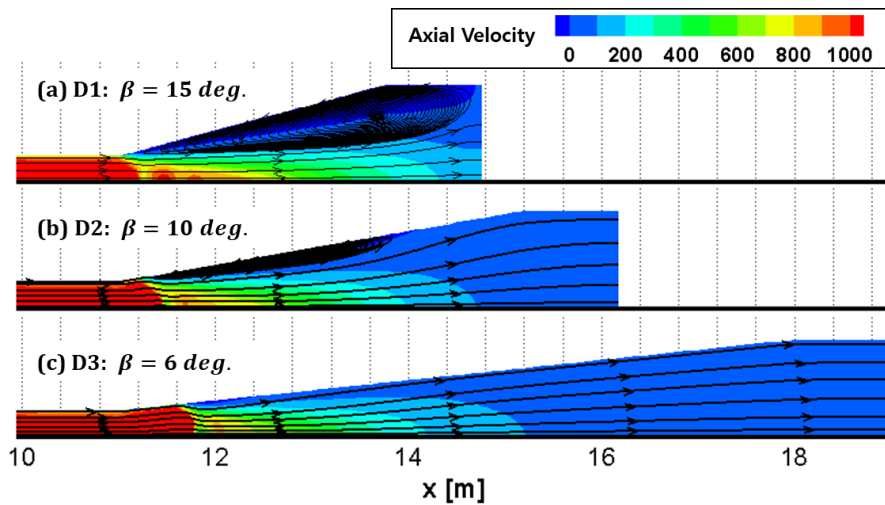


Fig. 41. Streamline and axial velocity distribution in the diffuser diverging section with different diverging half-angles

6.8. Diffuser Shape Derived from Parametric Study

Table 15 presents the determined design parameters and the resulting pressure recovery performance. The designed diffuser was able to stably generate Mach 7 flow in the test section under various backpressure conditions. The operable backpressure range of the diffuser was estimated, which was necessary to determine the specifications of other parts, such as vacuum facilities and heat exchangers. Figs. 42 and 43 illustrate the average static pressure and average Mach number along the axial direction with different backpressures, respectively. The terminal shock moved forward with the increasing backpressure, and the maximum operable backpressure was approximately 6,300 Pa. When the backpressure increased to 6,500 Pa, a terminal shock wave generated in the test section rendered the test inoperable. Considering other flow disturbances in an actual test environment, we determined that the diffuser can operate stably and efficiently at a backpressure of 5,500 Pa.

The designed hypersonic wind tunnel diffuser exhibited a maximum efficiency of 18.7%, with the large blockage test model included. The diffuser efficiency without a test model in previous studies (Brune et al., 2019; R.S Pugazenthil & Andy C. McIntosh, 2011; Savino et al., 1999) was approximately 20–40%. Although direct comparison of efficiency was difficult due to different flow conditions and sizes of the hypersonic wind tunnels, the designed diffuser exhibited a high efficiency even with the large blockage model.

Table 15 shows design variables and performance of HWT diffuser determined via conventional and parametric study based design procedures. The design based on the parametric study brought about a 60% increase in the efficiency of the diffuser compared to the baseline design.

Table 15. Design variables and performance of HWT diffuser determined via conventional and parametric study-based design procedures

Parameters \ Design		Baseline	Parametric study base
Test section	$D_n [m]$	0.396	0.396
	$L_{sep} [m]$	0.855	1.0
	Blockage [%]	40	40
Converging section	$D_i [m]$	1.3	1.2
	$L_{cs} [m]$	None	0.7
	$\alpha [deg.]$	5	6
Throat	$D_{t2} [m]$	0.873	0.730
	L/D_{t2}	15.0	11.0
	A_{t2}/A_{t1}	700	489
Diverging section	$\beta [deg.]$	3	10
	$D_e [m]$	1.0	2.0
Operability		O	O
Pressure recovery	$p_{b,max} [Pa]$	4,000	6,300
	$\eta [\%]$	11.8	18.7
	<i>Improvement</i> [%]	-	57.5

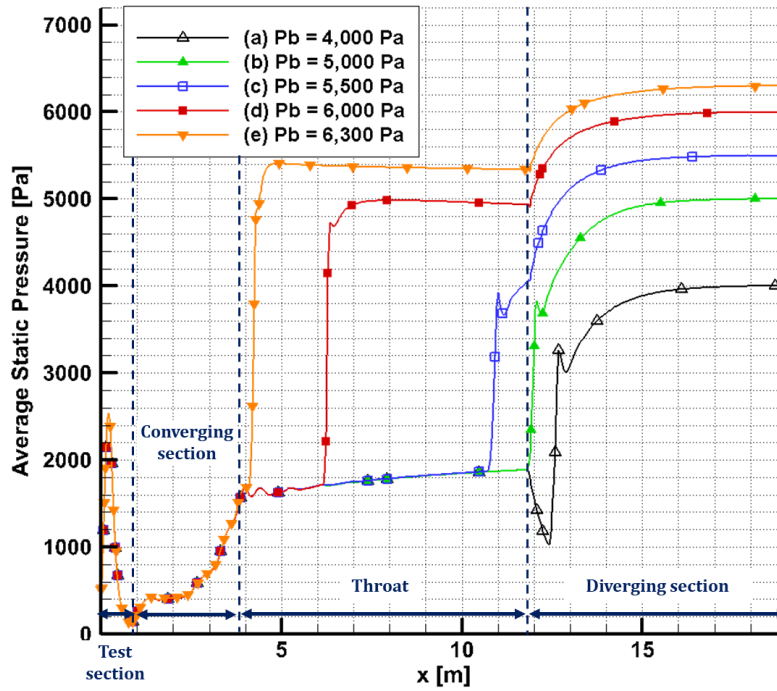


Fig. 42. Average static pressure along the axis for the designed diffuser with different backpressures

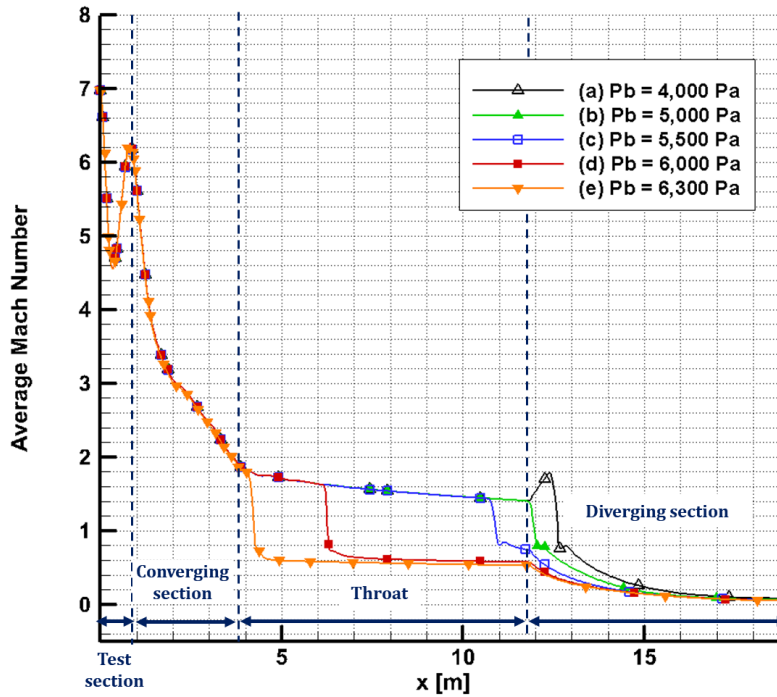


Fig. 43. Average Mach number along the axis for the designed diffuser with different backpressures

CHAPTER 7

SURROGATE MODEL BASED DESIGN

7.1. Overview

In this chapter, the surrogate model based HWT diffuser design study was conducted. This study tried to resolve the problem that parametric study based diffuser design method requires excessive time and human resource, and relies on the insights or know-how of researchers. First, the study established a framework that can systematically analyze the diffuser design space. Using this framework, the surrogate model for the performance of the HWT diffuser was constructed, and the design space was explored. The HWT diffuser with high performance was designed based on the surrogate model. The main conclusions of this chapter are as follows.

(1) An appropriate design space was determined through a design space feasibility study, and through this, it was confirmed that the conventional design process that simply refers to an existing shape or uses an empirical formula is highly risky.

(2) The surrogate model for the operability and efficiency of the HWT diffuser, which has both accuracy and convergence, was derived.

(3) Through the design space exploration study using the surrogate model, it was confirmed that the diffuser inlet diameter is a highly important variable along with the variables emphasized in the

previous *Chapter 6*.

(4) The HWT diffuser was designed using a surrogate model and showed considerable high efficiency than the diffuser shapes from conventional and parametric study based methods.

7.2. Framework

The framework constructed is shown in Fig. 44. First, shape design variables and ranges of a HWT diffuser were determined to make design space considering design constraints. Experimental points to be analyzed were sampled in the design space. After that, framework automatically generated geometry and high-quality mesh for each sample point calculation. Subsequently, numerical flow analyses were conducted and resulted in maximum operable back-pressure, or maximum efficiency, of each HWT diffuser shapes. Using these data, surrogate model was created and validated. If the reliability of the surrogate model does not meet criteria, the surrogate model is repeatedly updated to meet the criteria by infilling the samples. After creating a surrogate model, the diffuser performance could be predicted immediately, so the efficient design of diffuser was possible. Later, sensitivity analysis was performed using the surrogate model.

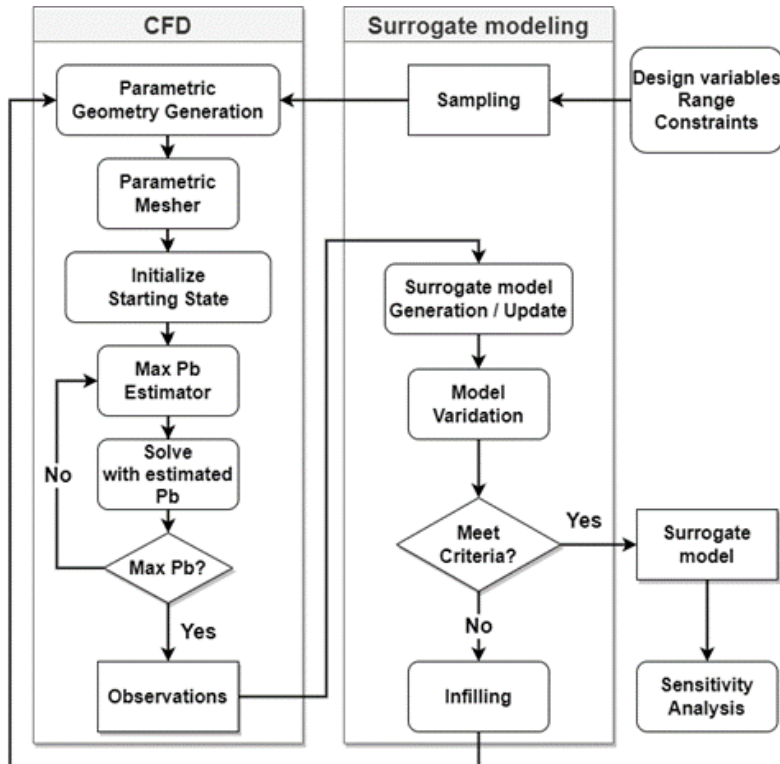


Fig. 44. Flow-chart and framework of the study

7.3. Kriging Model

7.3.1. Design Space Feasibility Study

In order to effectively solve a design problem, it is essential to properly set up a design space. In the case of the HWT diffuser design problem, since there were not enough previous studies to use as a reference, the design space was determined through a design space feasibility study to select an appropriate design space.

As described in previous chapters, simply referencing the existing shapes or using empirical formulas was highly risky. Therefore, a certain range was set based on the diffuser configuration designed from the parametric study. Through this, the preliminary design space was determined. Afterwards, sampling and flow analysis were performed in this preliminary design space. Through these sampling flow analysis results, the feasibility of the preliminary design space was assessed. The design variable range in which only inoperable shapes exist for each design variable was excluded from the design space, and the design variable range showing high performance was included.

Fig. 45 shows whether the sampled diffuser shape was operable or not according to inlet diameter (x-axis). Green symbol indicates operable diffuser shape and red symbol indicates inoperable shape. Since the design requirements and constraints of the study were quite severe, it can be confirmed that many of sampled shape were inoperable. The preliminary design space is marked with a blue background. It seems that the HWT cannot be operated in the area where the length of the diffuser inlet diameter exceeds 1.6 m. Therefore, the subsequent design space was adjusted to have a diffuser inlet diameter of 1.6 m or less.

Range adjustment was performed in the same way for other variables, and the final design space was determined as shown in Table 16. A kriging model was constructed in the resulting design space.

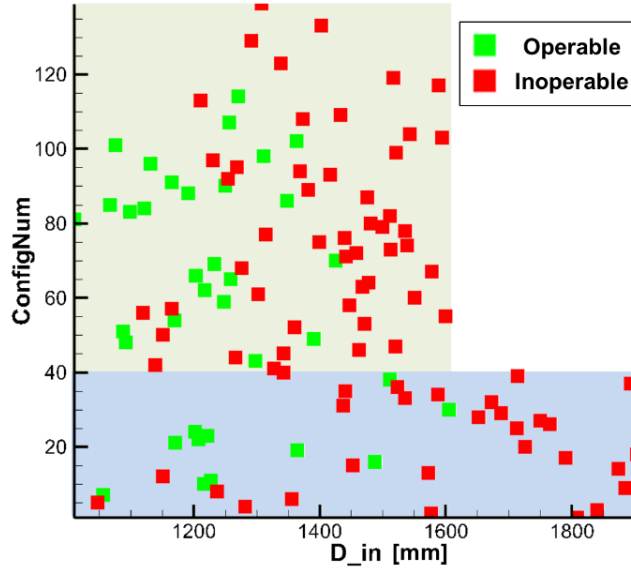


Fig. 45. Operability of the Sampled configurations of the HWT diffuser

Table 16. Design space determined

Design Var.	Min	Max
L_{sep} [m]	0.0	0.3
Blockage [%]	40 (Constant)	
D_i [m]	1.0	2.0
L_{cs} [m]	0.0	1.5
α [deg.]	2	15
A_{t2}/A_{t1}	400	1000
L/D_{t2}	5	20
β [deg.]	2	15
D_e [m]	1.0	4.0

Through this determined design space, it was clearly confirmed how risky the conventional diffuser design method can be. Fig. 46 illustrates the shape variables of the existing HWT diffusers and the shape variables calculated by the conventional design method, together with the design variable range derived from the design space feasibility study in this section. Existing shape variables are distributed over a fairly wide range, and there are many shape variable values that deviate significantly from the current design space.

The reason why the variable range derived in the design space

feasibility study is different from the conventional design can be explained as follows. The operating conditions of the existing diffusers was different from those of this study. And, the test model was included in this study. In addition, it is difficult to say that the existing diffuser shape variables were derived through sophisticated design studies or optimized values. Especially, it is highly probable that the ratio of the throat area would be derived as a very inappropriate value through the conventional method. In addition, the converging angle of the diffuser, which should have a small angle, is often distributed as a fairly large value in conventional design. And the diffuser diverging angle is clustered to an excessively small value, which will increase the total length of the diffuser and the construction cost without little gain of efficiency.

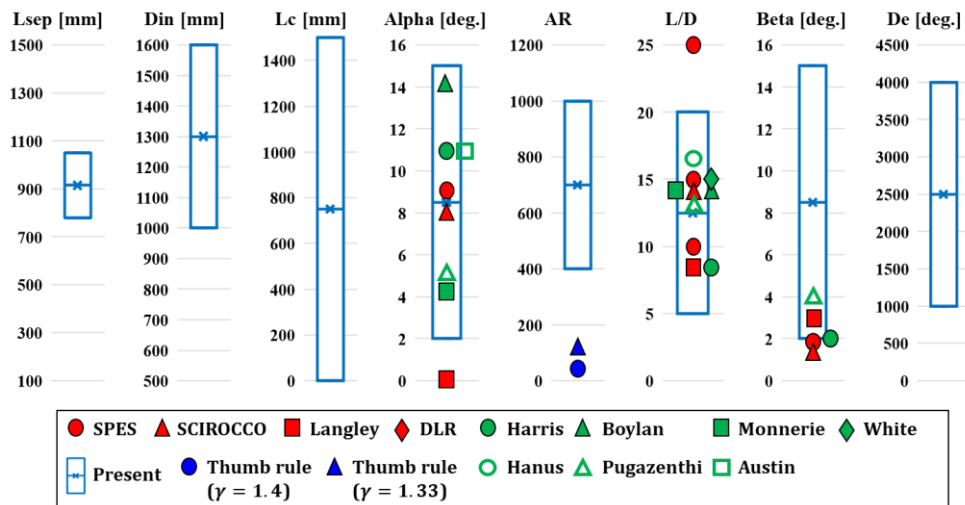


Fig. 46. The shape variables of the existing HWT diffusers and the shape variables calculated by the conventional design method, together with the design variable range of present study

7.3.2. Generation of Kriging Model

Using the framework, the kriging model was constructed for operability and maximum operable back-pressure according to design variables, respectively. There were a total of 720 sampling

analyses performed in this study, of which 213 were operable shapes, and the rest were inoperable shapes. For the kriging model of operability, all sampling analysis results were used. The value of operability was set to 1 for operable shapes, and operability was set to 0 for inoperable shapes, and then the kriging model was constructed.

The kriging model for the maximum operable back-pressure of the diffuser was constructed using only the results of the operable configuration. Infilling was repeated until the convergence of the kriging model was confirmed, and the accuracy criteria of the kriging model was fulfilled. Details are described in the next section. Finally, a total of 213 sample data were used.

Table. 17 shows the derived kriging coefficient. Theoretically, it represents the coefficient of each term of variables in the distance function. Since the Gaussian distance function was used for the distance function, according to the definition of the function, the larger the coefficient value, the greater the influence, and the stronger the influence is reflected especially on closely located samples. Conversely, coefficient values of variables with little influence becomes close to zero. In this way, the effect of each design variable on the performance variable can be roughly confirmed through the value of the kriging coefficient.

Table 17. Coefficients for the constructed kriging model for operability and maximum operable back-pressure

Kriging Coefficient	Related Variable	Operability	Max. Pb
θ_1	L_{sep}	0.47	0.30
θ_2	D_{in}	2.91	98.71
θ_3	L_{cs}	13.56	10.36
θ_4	α	3.74	6.93
θ_5	AR	4.24	27.99
θ_6	L/D	0.15	4.20
θ_7	β	0.07	0.12
θ_8	D_{exit}	0.01	0.00

7.3.3. Reliability Assessment of Kriging Model

In this study, the kriging model was used as the surrogate model, and the performance of the diffuser was predicted and the design was performed through this kriging model. In addition, the kriging model was used in the exploration study for the entire design space. Therefore, the reliability of the kriging model was highly important throughout the study.

Fig. 47 shows the LOOCV result of the constructed kriging model for maximum operable back-pressure. Overall, it can be seen that the predicted value of the kriging model followed the actual CFD value. In the most ideal case, the verification point is located on the line of $y = x$ (kriging prediction=CFD calculation), and the determination coefficient, a metric that quantifies the goodness-of-fit of the line of each verification point, was calculated. Fig. 48 shows that the determination coefficient converged appropriately at the 96% level as the number of samples increases.

The prediction error was also evaluated through NRMSE and MAE. First, it was confirmed that NRMSE converges at about 5% level (Fig. 49), and this represents the overall error of the kriging model was 5%. In the case of MAE, it was confirmed that it converged with an error of about 200 Pa (Fig. 50). In the flow analysis to find the maximum back-pressure, the back-pressure was increased step by step. Considering that the back-pressure was not continuously increased for practical reason, and increased in units of 200 Pa, it can be seen that the inherent error with this training sample was 199.9 Pa. Considering this, MAE 200 Pa was judged to be acceptable.

Comprehensively, the reliability of the kriging model was judged to be sufficient, and subsequent studies were conducted based on this kriging model.

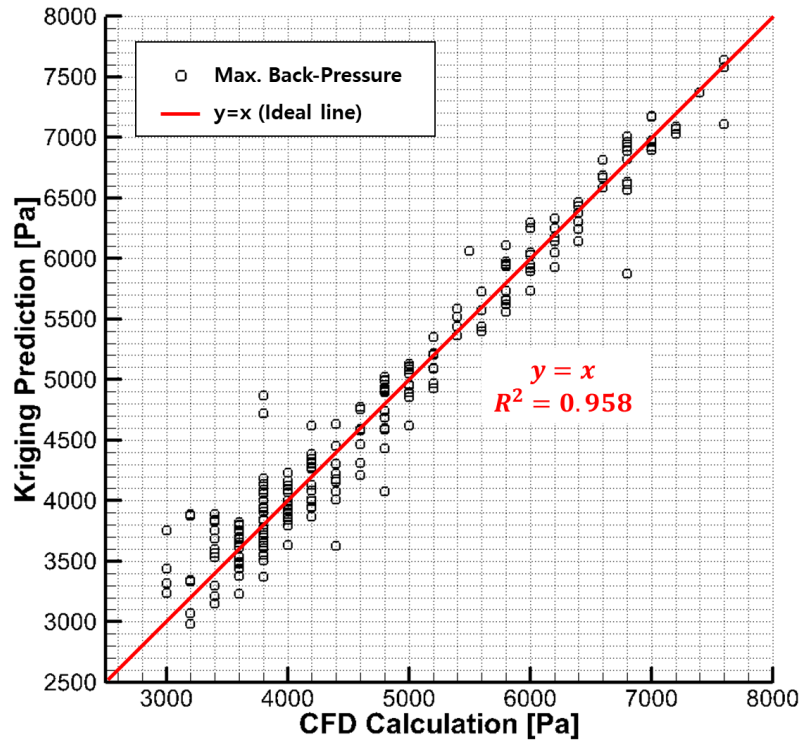


Fig. 47. LOOCV result of the constructed kriging model for maximum operable back-pressure

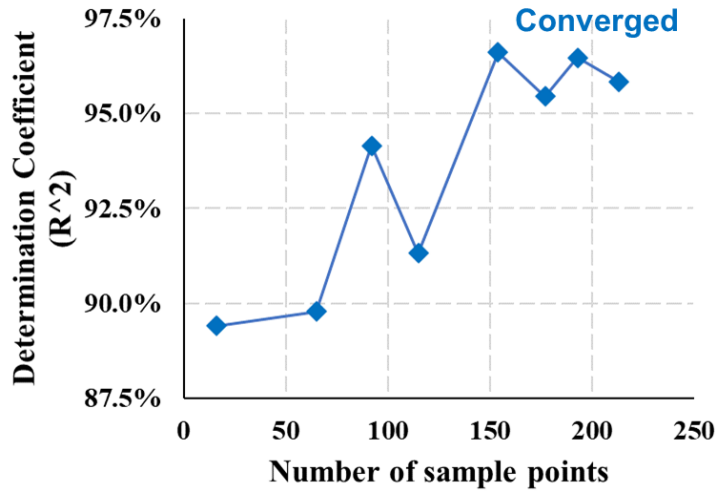


Fig. 48. Convergence history of determination coefficient of linear regression between kriging prediction and CFD calculation in LOOCV

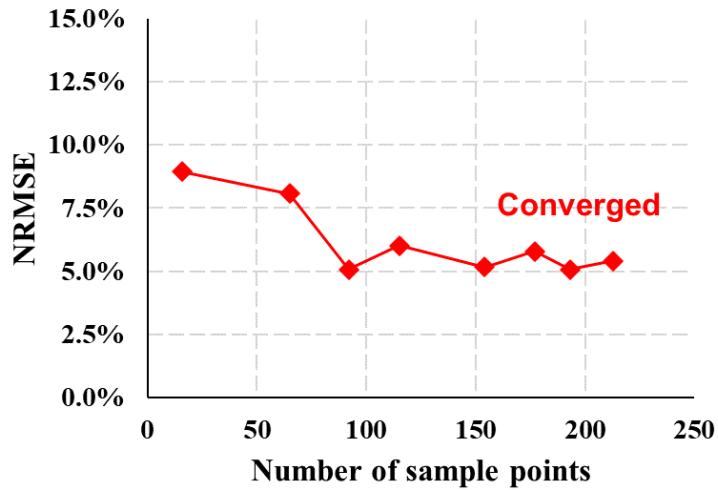


Fig. 49. Convergence history of NRMSE between kriging prediction and CFD calculation in LOOCV

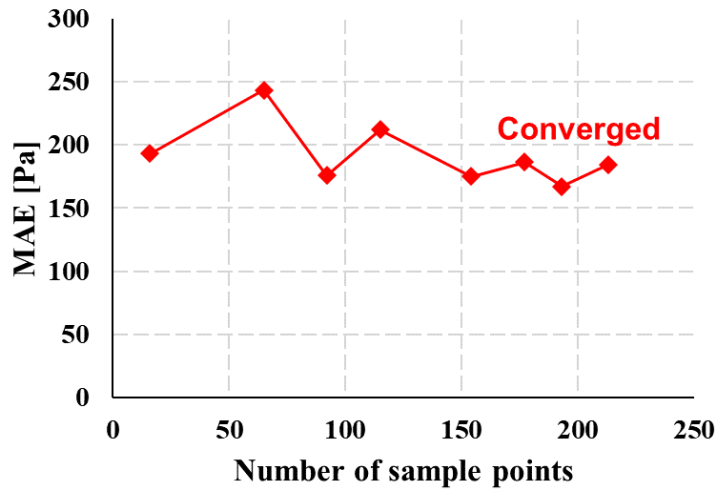


Fig. 50. Convergence history of MAE between kriging prediction and CFD calculation in LOOCV

7.3.4. Kriging Response Surface and Design Space Exploration

This section visualized the maximum operable back-pressure of the HWT diffuser in the entire design space based on the established kriging model. Through this, it was possible to confirm the diffuser performance distribution in the entire design space, rather than exploring only a part of the entire design space as in parametric study based design. This exploration not only helped to understand the design space more comprehensively, but it could also prevent the design shape from being the local optimum shape that can occur in parametric study based design.

Kriging response surface is a function that places a design variable to an x- and y-axis as independent variables and a maximum operable back-pressure as a z-axis dependent variable. Other design variables not selected as independent variables were fixed as the median value of the design space range. Since throat area ratio, AR , is one of the most influential variables in diffuser performance, AR was always selected as an independent variable, and the remaining one independent variable was selected one by one as Eq. (81). Through this, the degree of change in maximum operable back-pressure according to the change in AR and the degree of change in maximum operable back-pressure according to change in the other independent variable can be clearly identified.

$$\begin{aligned} z_{xy} = z(x, y_i) \mid \mathbf{dv}_{\sim x, y} = \text{median value of range,} \\ x = AR, y_i = dv_i, \mathbf{dv} = [L_{sep}, D_{in}, L_{cs}, \dots] \end{aligned} \quad (81)$$

Figs. 51–58 show the visualized kriging response surfaces (left) and the slice results (right) of the surface. Overall, it can be seen that AR was influential when compared with other variables, and it can be seen that D_{in} , D_{in} , and D_{in} were also influential. It can be confirmed that the other variables had little influence compared to the previous variables, and in particular, L/D , β , and D_{ext} had very marginal influence.

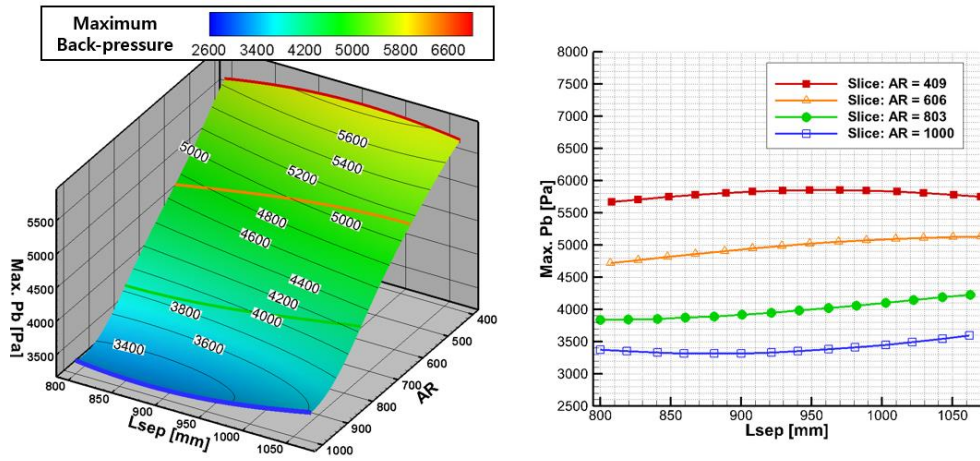


Fig. 51. Kriging response surface (left) and slice chart (right) for maximum back-pressure according to design variables AR and L_{sep}

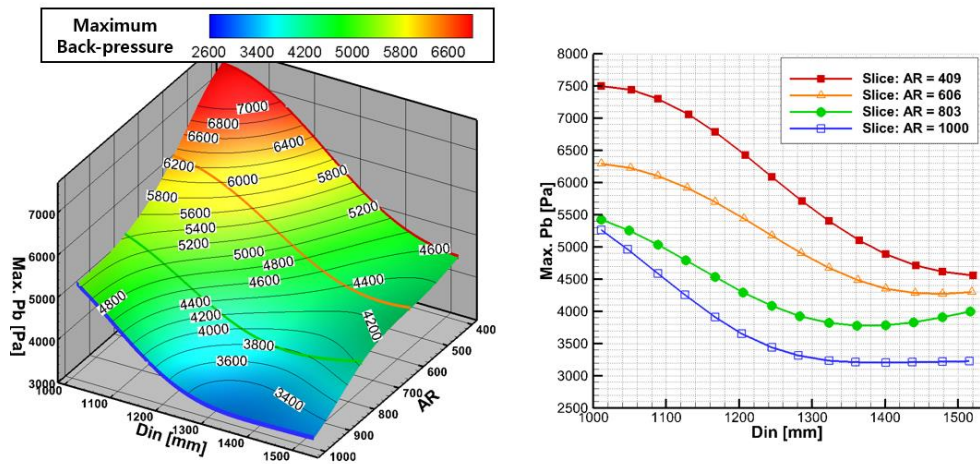


Fig. 52. Kriging response surface (left) and slice chart (right) for maximum back-pressure according to design variables AR and D_{in}

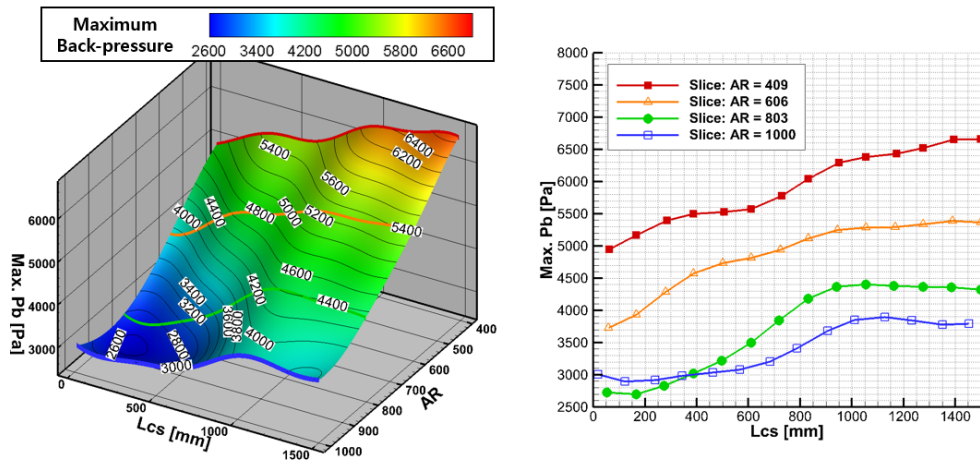


Fig. 53. Kriging response surface (left) and slice chart (right) for maximum back-pressure according to design variables AR and L_{cs}

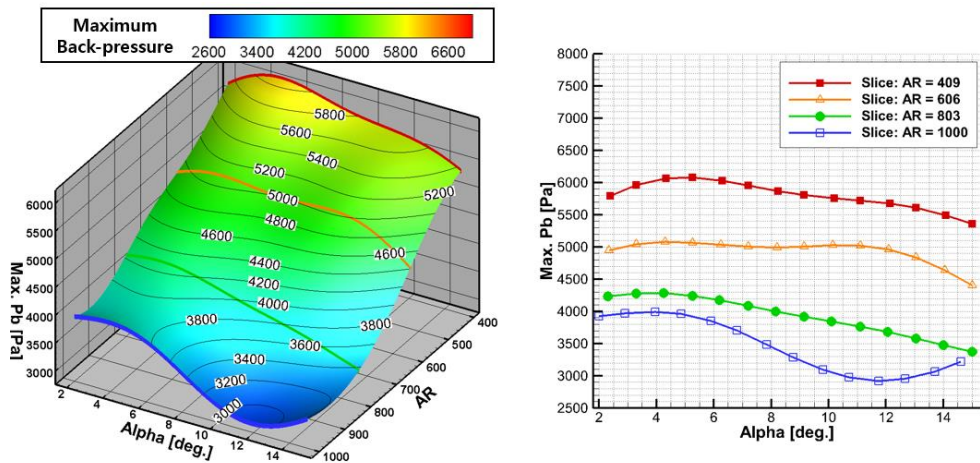


Fig. 54. Kriging response surface (left) and slice chart (right) for maximum back-pressure according to design variables AR and α

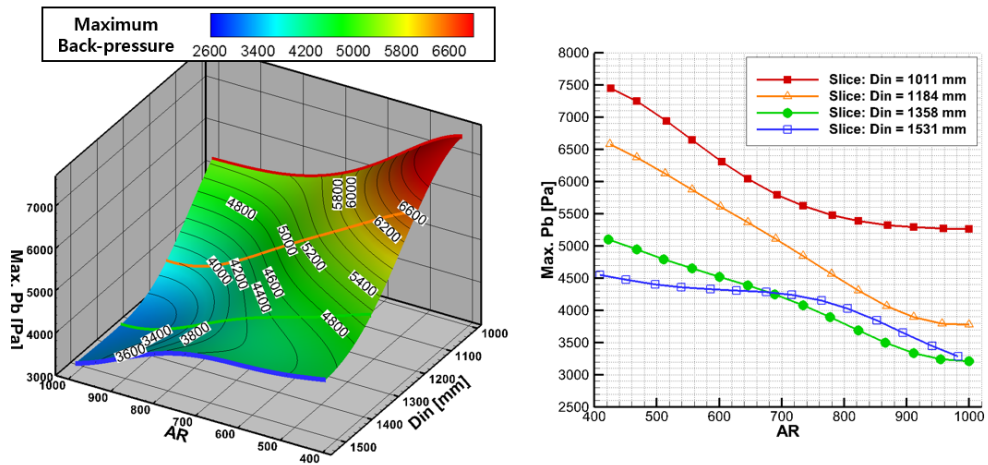


Fig. 55. Kriging response surface (left) and slice chart (right) for maximum back-pressure according to design variables D_{in} and AR

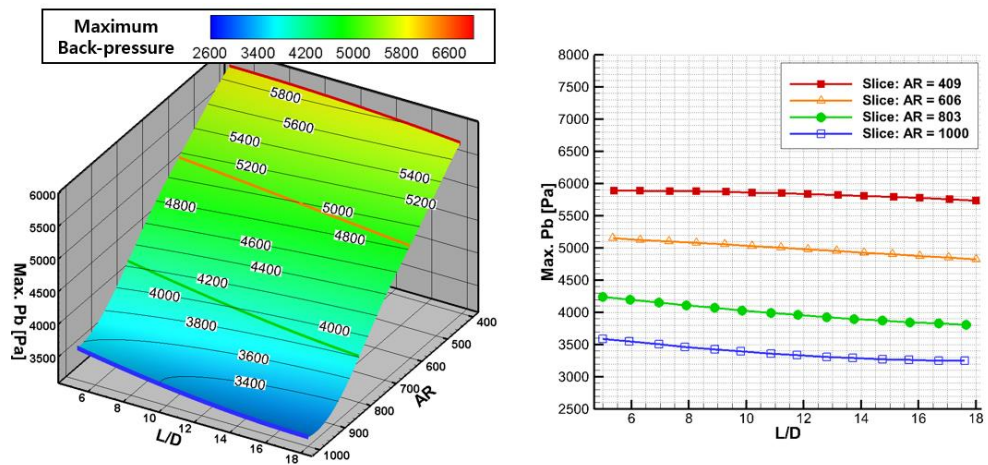


Fig. 56. Kriging response surface (left) and slice chart (right) for maximum back-pressure according to design variables AR and L/D

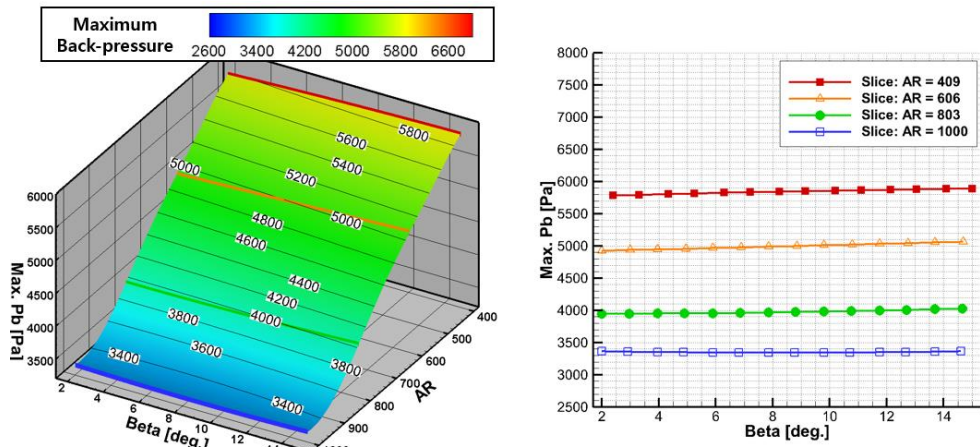


Fig. 57. Kriging response surface (left) and slice chart (right) for maximum back-pressure according to design variables AR and β

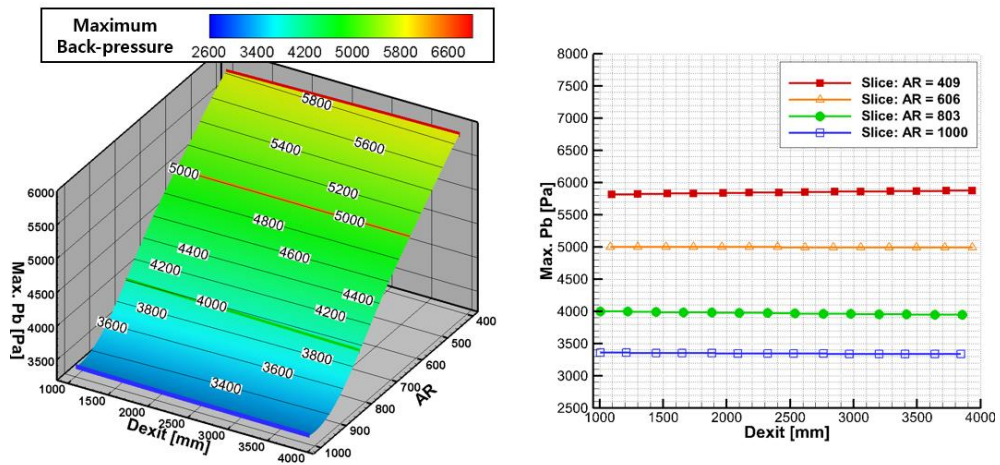


Fig. 58. Kriging response surface (left) and slice chart (right) for maximum back-pressure according to design variables AR and D_{exit}

7.3.5. HWT Diffuser Design using Kriging Model

Based on the sampling analysis data and the established kriging model, the shape of the HWT diffuser was determined and performance evaluation was performed. Safety factor was considered to determine diffuser throat area to be about 10% larger, which is similar way to determine throat area in parametric study based design. Operability and operable maximum back-pressure were derived, and performance comparison between the previously designed baseline shape and the parametric study based shape was also performed.

Table 18 shows design variables and performance of HWT diffuser determined via various design procedures. Although the design based on the parametric study brought about a 60% increase in the efficiency of the diffuser compared to the baseline design, the design based on surrogate model showed a significant further increase in efficiency. Ultimately, it was a 90% increase in efficiency compared to the baseline shape, and a 20% increase in efficiency even compared to the parametric study based design. Considering that much less time and resources were required to perform such a good design than the parametric study based design, the usefulness of the surrogate model based design framework constructed in this study can be confirmed once again.

Table 18. Design variables and performance of HWT diffusers determined via various design procedures

Parameters \ Design		Baseline	Parametric study base	Kriging model base
Test section	$D_n [m]$	0.396	0.396	0.396
	$L_{sep} [m]$	0.855	1.0	0.811
	Blockage [%]	40	40	40
Converging section	$D_i [m]$	1.3	1.2	1.064
	$L_{cs} [m]$	None	0.7	0.926
	$\alpha [deg.]$	5	6	6
Throat	$D_{t2} [m]$	0.873	0.730	0.730
	L/D_{t2}	15.0	11.0	9.0
	A_{t2}/A_{t1}	700	489	453
Diverging section	$\beta [deg.]$	3	10	8
	$D_e [m]$	1.0	2.0	1.483
Operability		O	O	O
Pressure recovery	$p_{b,max} [Pa]$	4,000	6,300	7,600
	η [%]	11.8	18.7	22.6
	<i>Improvement</i> [%]	-	57.5	90.0

Fig. 59 illustrates the pressure distributions at different back-pressure. Figs. 60 and 61 illustrate the average static pressure and average Mach number along the axial direction with different backpressures, respectively. The terminal shock moved forward with the increasing backpressure, and the maximum operable backpressure was 7,600 Pa.

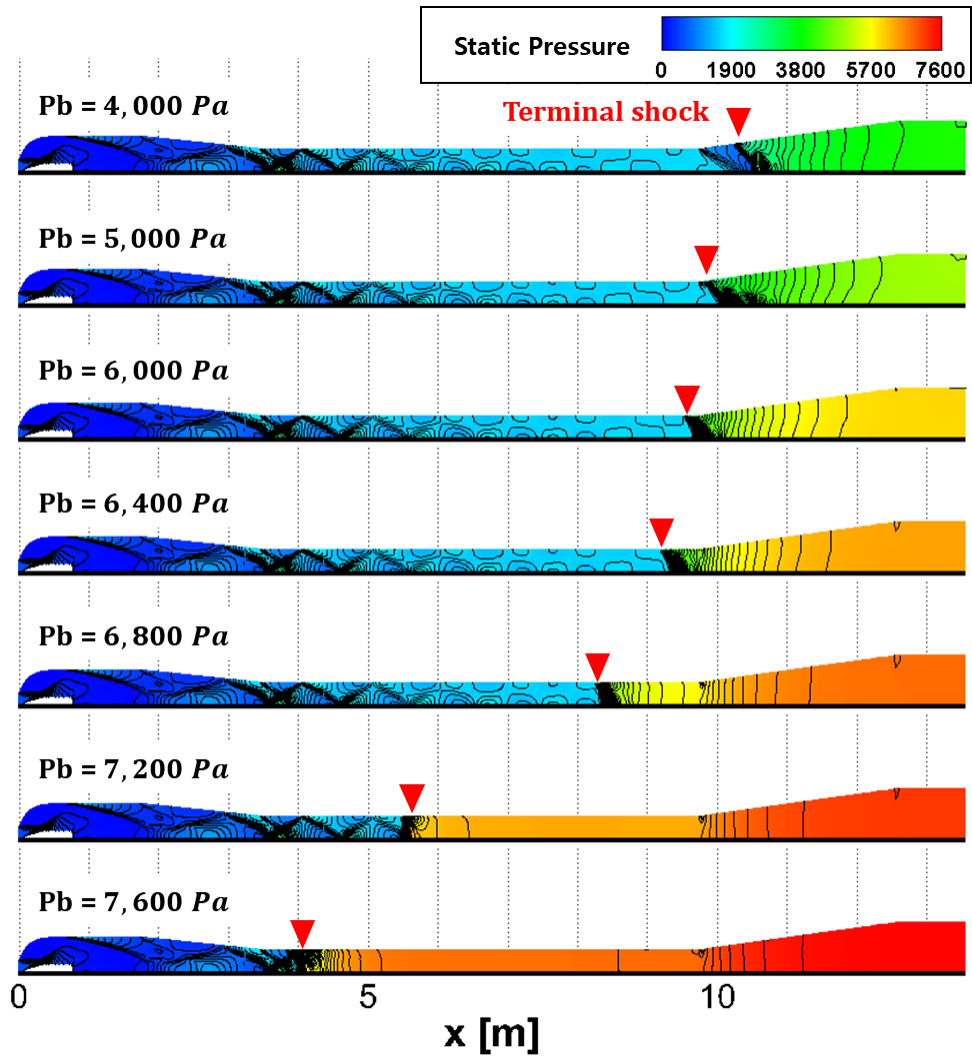


Fig. 59. Pressure distribution and terminal shock location of diffuser from surrogate model with different back-pressures

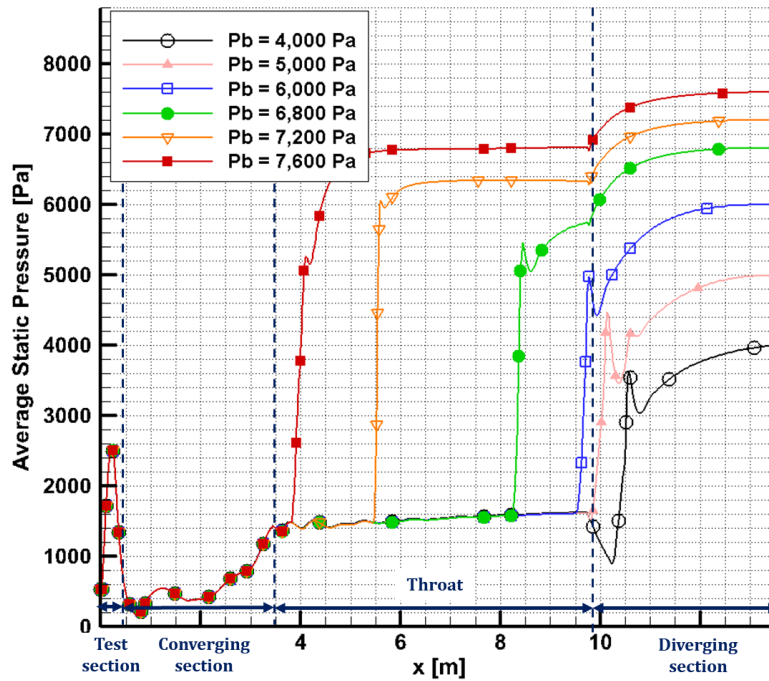


Fig. 60. Average static pressure along the axis for the designed diffuser from surrogate model with different back-pressures

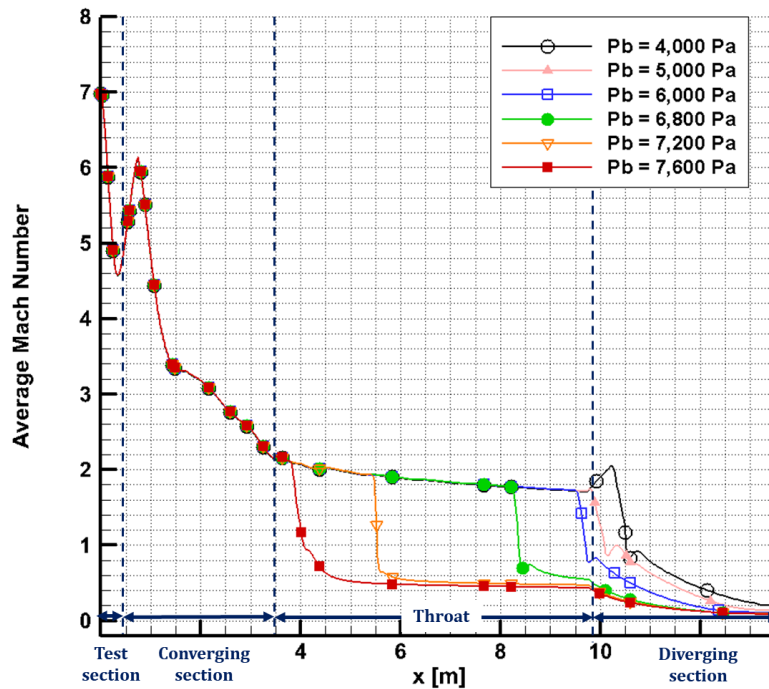


Fig. 61. Average Mach number along the axis for the designed diffuser from surrogate model with different back-pressures

7.4. Design considering Off–design Condition

7.4.1. Motivation

The designs before in the study aimed to design a high efficiency diffuser under challenging specific condition where Mach 7 hypersonic flow and the large blockage model were present. (On–design point) This design focused on enabling the most efficient and stable test in the state where the flow condition and the test model were determined.

However, in general, HWT can control various inflow conditions by replacing or modifying the nozzle. Therefore, it may sometimes be more appropriate to design by considering the on–design point and the off–design point, simultaneously. Therefore, in this section, considering off–design as well as the on–design condition, the HWT diffuser was designed to secure the operability and high efficiency in a wide flow range. Through the framework developed in this study, it was possible to derive a diffuser shape that showed high performance under different flow conditions without excessive time and human resources.

7.4.2. On–design and Off–design Condition

The operating conditions of NASA Langley's AHSTF referenced in this study ranged from Mach number 4.7 to 8. Reservoir conditions for generating each Mach number are all different, and the nozzle throat area for Mach number 6, 7, and 8 flow conditions is different from the nozzle throat area for Mach number 4.7, 5, and 5.5. That is, a nozzle or reservoir condition generating a low Mach number such as Mach number 4.7 is greatly different from a condition generating a high Mach number such as Mach number 7. Table 19 shows the reservoir condition for each Mach number of AHSTF, and shows the nozzle throat area and nozzle exit flow conditions calculated based on the reservoir conditions. Isentropic process was assumed for the calculation of nozzle throat and nozzle exit variables, the special gas

constant was $287.06 \text{ J/kg} \cdot \text{K}$, and the specific heat ratio was 1.363.

Table 19. Reservoir conditions and calculated nozzle exit flow variables of NASA Langley AHSTF according to inflow Mach number

	Reservoir		Nozzle			
Mach Number	P_0 [atm]	T_0 [K]	A^* [m ²]	D_{ne} [m]	P_{ne} [Pa]	T_{ne} [K]
4.7	13.6	1,123	0.003	0.301	3,249	224
5.0	13.1	1,251	0.003	0.342	2,148	226
5.5	11.2	1,468	0.003	0.423	1,012	226
6.0	35.1	1,655	0.00083	0.271	1,811	220
7.0	28.6	2,216	0.00083	0.390	531	224
8.0	23.0	2,879	0.00083	0.540	171	228

For testing in a wide operating range, an HWT diffuser that is highly efficient not only in the high Mach number of Mach 7, but also in the flow conditions of low Mach number of Mach 4.7 (different nozzle and reservoir condition) would be required. In the case of Mach number 4.7, the lowest Mach number, the flow conditions at the nozzle exit are greatly different. And, even if the blockage ratio of the model is the same, the shock wave angle generated from the model will become larger. This may result in an additional constraint that the inlet diameter of the diffuser must be larger.

Therefore, the lowest Mach number condition, Mach number 4.7 was selected as the off-design condition and the design was performed. In the case of the performance change at the extreme condition of opposite side, Mach number 8, the trend was almost similar to that of Mach number 7, and there was only a difference in the degree of lowering the efficiency. Therefore, it was judged that the Mach number 7 condition could sufficiently represent the Mach number 8 condition, and the Mach number 8 condition was excluded from the design.

7.4.3. Design Objectives

The performance objective function, $PF(\mathbf{x})$, which can evaluate the performance of the HWT diffuser, was constructed as Eq. (82). The design objective was to maximize the performance objective function under the constraints of Eq. (83).

Maximize

$$PF(\mathbf{x}) = NPB_{M7}(\mathbf{x}) + \alpha \times NPB_{M4.7}(\mathbf{x}) - \beta \times NSIZE(\mathbf{x}), \quad (82)$$

$$\alpha = 0.5, \beta = 0.5$$

Subject to

$$OPER_{M7}(\mathbf{x}) \geq 1, OPER_{M4.7}(\mathbf{x}) \geq 1, L_{total} \leq 20 \text{ m} \quad (83)$$

$NPB_{M7}(\mathbf{x})$ is the normalized maximum operable back-pressure to the maximum value of the maximum operable back-pressures of various shapes under the condition of Mach number 7. $NPB_{M4.7}(\mathbf{x})$ is the normalized maximum operable back-pressure to the maximum value of the maximum operable back-pressures of various shapes under the condition of Mach number 4.7. However, the weighting (α) of 0.5 was applied to the off-design condition, so that the relative importance was reflected differently. $NSIZE(\mathbf{x})$ represents the occupying area of the test section and diffuser of the HWT and is obtained by multiplying the total length of the test section-diffuser and the maximum diameter of the diffuser. The weighting (β) of 0.5 was applied to this term because it would be less important than the maximum back-pressure in the on-design condition. These weights would be changed, or additional terms would be added to the performance objective function to suit the other purpose or condition of the design. In the case of constraint, $OPER(\mathbf{x})$ is a function that indicates the operability at each Mach number, and the value is set to 1 for operable shapes and set to 0 for inoperable shapes.

In order to find the optimal point of the problem defined above, the maximum value of the performance objective function was derived based on the surrogate models. Since the performance value of the surrogate model can be obtained immediately, the maximum

operable back–pressure for the entire design space was predicted, and the global maximum value was derived. If the operability of a shape predicted from the surrogate model was less than 1, it was judged that the risk of inoperability was high, and the shape was excluded from the design. The previous constraint that the total length of the diffuser should be less than 20 m was applied in the same way.

7.4.4. Optimization Procedure

In this section, the procedure for finding the optimal shape is explained step by step. The surrogate models for Mach 4.7 were constructed, and the performance function value of Eq. (82) was calculated by combining the model with the already constructed surrogate model of Mach 7. Excluding the inoperable shapes, the diffuser shape with the highest performance function value was derived, and its reliability was confirmed through actual CFD analysis.

► Construction of Surrogate Model for Mach 4.7 Condition

In the same way as the surrogate model created at Mach number 7, the kriging models that can efficiently predict the performance of the diffuser at Mach number 4.7 were generated. CFD analyses were performed on a total of 400 sampled diffuser shapes to generate the surrogate model. The surrogate model for maximum back–pressure was created based on 96 operable shapes among total 400 shapes, and the surrogate model was created for operability using all 400 samples. As in the case of Mach number 7, the operability of operable shape was assigned to 1, and the inoperable shape was assigned 0.

► Predict Performance Function using Surrogate Models

Performance function values were predicted using the constructed surrogate models. The maximum back–pressure was normalized to the predicted maximum value to calculate the $NPB(\mathbf{x})$ s. When the prediction value for operability, $OPER(\mathbf{x})$, was less than 1,

the performance function value was set to 0, and shapes that may be unstable in operation were filtered out. $NSIZE(\mathbf{x})$ was calculated through shape parameters.

► Random Sampling based Optimum Point Searching

Since the number of cases was too large to consider all cases with full factorial, the optimal point was found by repeating the LHS and predicting the performance function value at the sample point. Sampling was performed six times in unit of 20,000 samples, resulting in a total of 120,000 samples. As the sampling proceeded, the sampling domain was reduced to a design space with high performance. The sampling was terminated at the 6th sampling where the maximum value did not change compare to 5th sampling.

Since filtering was performed under quite conservative constraints in terms of operability ($OPER(\mathbf{x}) \geq 1$), only 1,644 sampled shapes out of 120,000 samples were predicted to be able to operate stably in both flow conditions while satisfying the design constraints. In Fig. 62, many of samples were filtered out as being unable to operate in one or both flow conditions. Through Figs. 62–65, it can be confirmed that the performance at Mach number 7.0 was compromised by about 30% considering Mach number 4.7 test. For 1,644 operable shapes, 9 shapes were selected in order of highest performance function value as candidates for the final design.

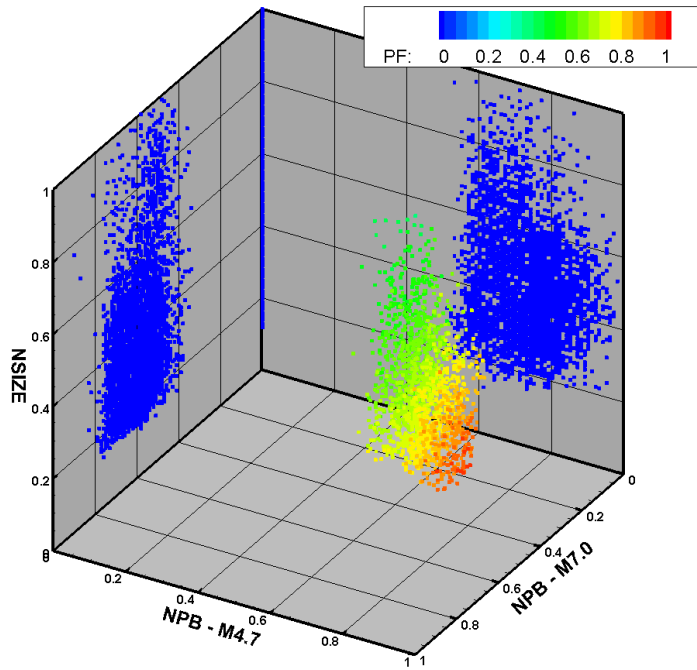


Fig. 62. Distribution of predicted performance function values according to terms constituting the performance function (blue symbol represent inoperable designs)

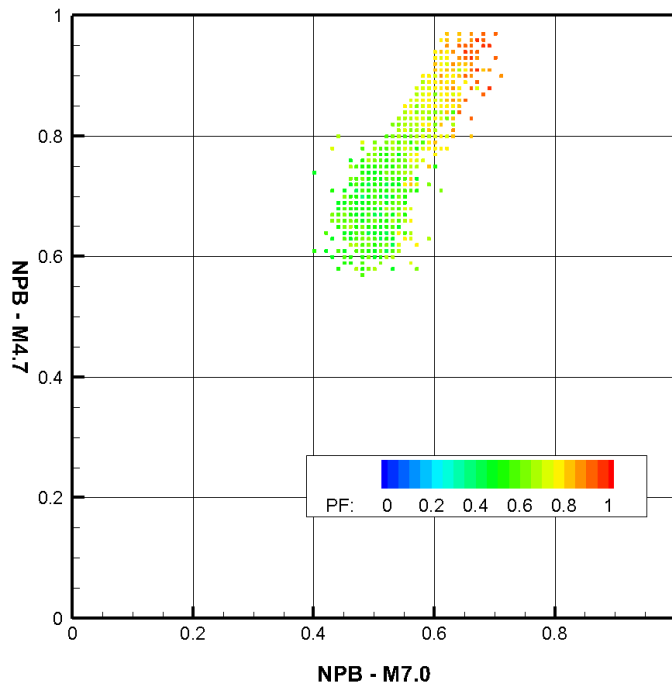


Fig. 63. Distribution of predicted performance function according to NPBs

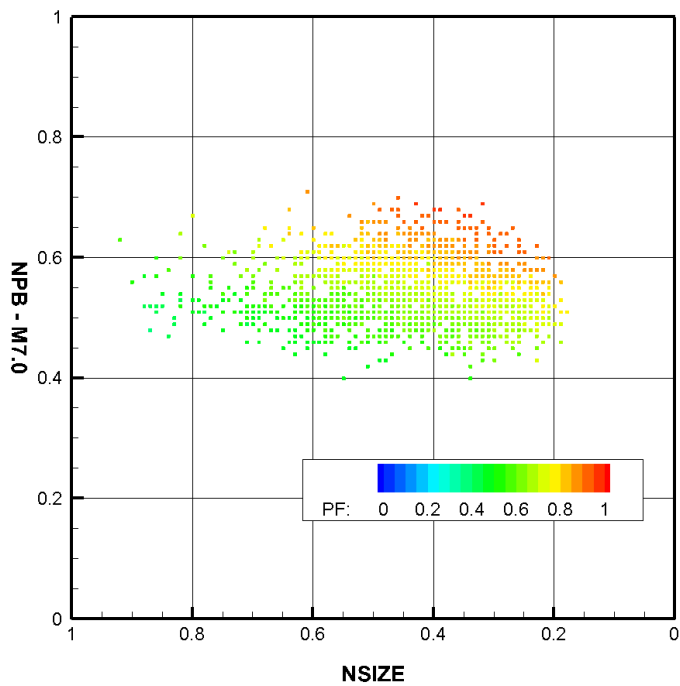


Fig. 64. Distribution of predicted performance fuction according to NPB7.0 and NSIZE

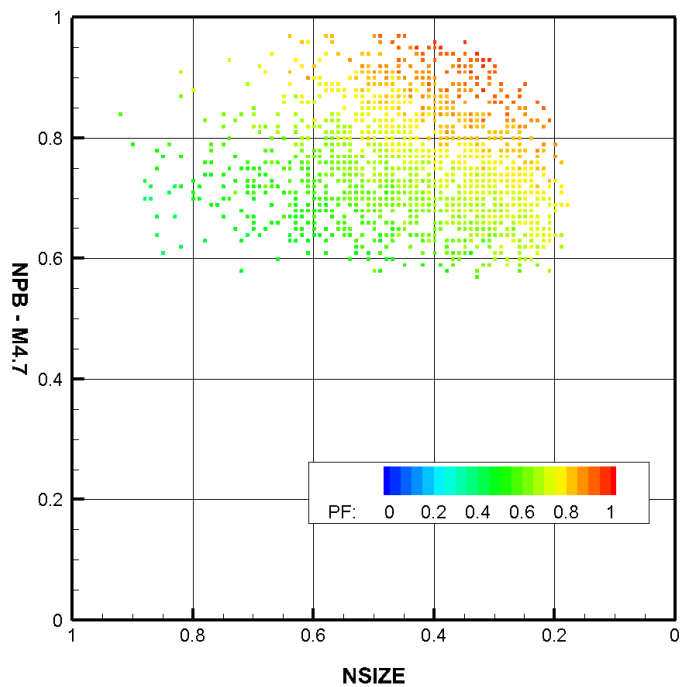


Fig. 65. Distribution of predicted performance fuction according to NPB7.0 and NSIZE

► CFD Calculations for Candidates with High Performance

CFD analyses were performed for 9 shapes in the order of the highest performance function value predicted based on the surrogate models. Table 20 shows the predicted values and CFD analysis values for the maximum back-pressure for these cases. Considering that the back-pressure increment in the CFD analysis was 200–250 Pa, it was judge that the predicted value agreed well with the CFD analysis value. Among these candidates, Config 1 with the highest performance function value in both surrogate model prediction and CFD analysis was determined as the final design shape.

Table 20. Predicted values and CFD analysis values for the maximum backpressure for design candidates

Config.	Mach 4.7		Mach 7.0		NSIZE
	CFD	Surrogate	CFD	Surrogate	
1	8,600	8,330	5,200	5,192	0.32
2	8,600	9,019	5,200	5,042	0.35
3	8,800	9,059	5,400	5,178	0.40
4	8,600	8,971	5,200	5,164	0.39
5	8,400	8,657	5,200	5,010	0.32
6	8,400	8,804	5,200	4,967	0.32
7	8,400	8,580	5,200	5,098	0.34
8	8,400	8,771	5,000	4,885	0.31
9	8,400	8,894	5,000	4,924	0.33

7.4.5. HWT Diffuser Design considering Off-design Condition

Table 21 shows design variables and performance of HWT diffuser determined via various design methods. Considering the off-design condition, the derived diffuser shape in this section was able to test in a wide range of flow conditions. However, it compromised the on-design performance about 30%.

Table 21. Design variables and performance of HWT diffusers

Parameters \ Design		Parametric study base	Surrogate model base	Off-design considering Design
Test section	$L_{sep} [m]$	1.0	0.811	0.899
	Blockage [%]	40	40	40
Converging section	$D_i [m]$	1.2	1.064	1.328
	$L_{cs} [m]$	0.7	0.926	1.5
	$\alpha [deg.]$	6	6	5
Throat	$D_{t2} [m]$	0.730	0.730	0.825
	L/D_{t2}	11.0	9.0	8.0
	A_{t2}/A_{t1}	489	453	625
Diverging section	$\beta [deg.]$	10	8	12
	$D_e [m]$	2.0	1.483	1.707
Operability	Mach 4.7	X	X	0
	Mach 7.0	O	O	0
Maximum backpressure	Mach 4.7	n/a	n/a	8,600 Pa
	Mach 7.0	6,300 Pa	7,600 Pa	5,200 Pa

7.4.6. Summary of Derived Diffuser Shapes

Fig. 66 shows configurations of designed diffusers and NASA AHSTF diffuser. The coordinates were rescaled x to y ratio to be 20 % for clarity. The front of the HWT diffuser of AHSTF is simply composed of a cylindrical shape with a large diameter. Although this configuration may be capable of stable testing in various conditions, this would have considerably low efficiency, resulting in high operating costs.

In the parametric study based design (PBD in Fig. 66), the shape of each part was adjusted to reduce the total pressure loss as much as possible while minimizing the risk of inoperability due to the large blockage model. The shape was adjusted to reduce the shock wave angle in the converging section, and the duct size was determined to be small as possible. These adjustments were further optimized through surrogate model based design (SBD in Fig. 66).

Considering the off-design condition of Mach number 4.7 (OBD in Fig. 66), the wave angle of the shock wave generated from the model increased, and thus the inlet diameter of the diffuser was increased to capture all the refracted flows. Since the total pressure loss increased as the inlet diameter of the diffuser increased, the throat area of the diffuser should be increased to pass the whole flow with lowered total pressure. Since the size of the wind tunnel was also considered in the performance function, the size of the subsonic diffuser was significantly reduced, resulting in a compact diffuser shape.

It is noted that the nozzle of AHSFT has a rectangular cross section rather than an axisymmetric shape as the present study, so the flow value and profile at the nozzle exit will be quite different. However, even considering the difference from this, the diffuser shape derived in the study is significantly different from the diffuser shape of AHSTF and is judged to be more efficient.

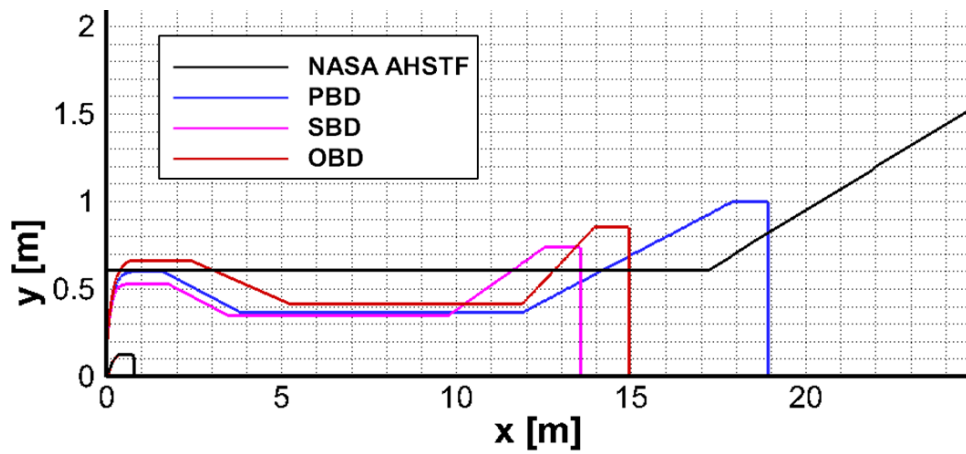


Fig. 66. Configurations of designed diffusers and NASA AHSTF (rescaled x to y ratio to be 20 % for clarity)

CHAPTER 8

SENSITIVITY ANALYSIS

8.1. Overview

Sensitivity analysis (SA) was performed through the sampling flow analysis results and the kriging models constructed. The sensitivity analysis in this section corresponds to the global sensitivity analysis. Whereas the parametric study only investigates near a specific point in the design space and in a specific direction, global sensitivity analysis examines how each design variable affects the objective function throughout the entire design space. In addition, sensitivity analysis can quantitatively evaluate the influence of each design variable and rank the importance of design variables.

In sensitivity analysis, the effect of the change of each shape variable on the operability and the maximum operable back-pressure of the diffuser (the maximum efficiency) were investigated. The input variables are shape parameters of HWT diffuser and output variables are HWT operability and maximum operable back-pressure. Correlation coefficients between each shape variable and objective functions were investigated, and the relationships between the two variables were visually confirmed through scatterplots. The magnitude of influence (sensitivity index) of each design variables was confirmed by analysis of variance, where the variance of operability and maximum operable back-pressure was decomposed into each variance contributions of each variable.

The main conclusions of this chapter were as follows:

(1) At least 1,000 observations were required for convergence of variance based sensitivity indices, which showed that the surrogate model was essential for efficient indices calculation.

(2) The design variables with the greatest influence on operability were diffuser inlet diameter, diffuser throat area ratio, catch-cylinder length, and diffuser converging angle in that order.

(3) The design variables with the greatest influence on efficiency were diffuser throat area ratio, diffuser inlet diameter, catch-cylinder length, and diffuser converging angle in that order.

(4) The relationship between the throat area ratio and maximum operable back-pressure was considered to be a fairly linear.

8.2. Deduction of Sensitivity Indices

8.2.1. Calculation of Sobol' Indices

Sensitivity indices based on variance decomposition can be applied to a variety of models, including nonlinear and multidimensional models. And it has many advantages, including the ability to quantitatively analyze not only the influence of a variable alone, but also the interaction effect between variables with high reliability. However, there is a critical disadvantage that computational cost is too high to calculate these indices. Therefore, in this study, the predicted values of the kriging model were used to calculate these sensitivity indices. The values required to obtain sensitivity indices were derived with the previously constructed kriging model with high reliability.

Table 22 shows the calculated sensitivity indices. It was calculated using Sobol's method, and it shows the effect of each variable on the operability and efficiency (maximum operable back-pressure) of the HWT diffuser. Total sensitivity indices and first order sensitivity indices can be confirmed. All sensitivity indices are normalized values to make it easier to identify relative contributions of variables. A detailed description of these indices values is described in a later section.

Table 22. Normalized variance decomposition based sensitivity indices (Sobol' indices) for operability and maximum operable back-pressure (ST: total sensitivity index, S1: first order sensitivity index)

Sensitivity Indices Variable	Operability		Max. Pb	
	ST	S1	ST	S1
L_{sep}	0.00	0.00	0.02	0.00
D_{in}	0.34	0.46	0.26	0.28
L_{cs}	0.19	0.17	0.19	0.13
α	0.17	0.15	0.08	0.02
AR	0.23	0.22	0.44	0.58
L/D	0.06	0.00	0.01	0.00

β	0.00	0.00	0.00	0.00
D_{exit}	0.00	0.00	0.00	0.00

8.2.2. Convergence of Variance based Sensitivity Indices

Sobol' sensitivity index is calculated from the objective function values distributed in the design space (samples). And, in the study, objective function values were predicted value from the kriging models. In this method, the value of indices may vary depending on how densely sampling is performed in the design space. Therefore, while increasing the sampling level, the value of index was calculated and convergence was confirmed. In this study, Sobol sequencing was used as the sampling method, and $n(2m + 2)$ kriging predictions are required. Here, m corresponding to the number of variables was 8, and n was increased to a power of 2 to confirm convergence.

Figs. 67 and 68 show the convergence history of total and first order Sobol' indices for HWT diffuser operability, respectively. The number of samples is expressed on a logarithmic scale. The value of indices varies depending on the number of samples used for calculation, and the rank of each sensitivity value does not change when the number of samples was 1024 or more. Finally, the convergence was determined when the number of samples reached 8192, and the indices was determined with the value at this time.

Similarly, Figs. 69 and 70 are convergence history of total and first order Sobol' indices for HWT diffuser maximum operable back-pressure, respectively. The rank of each sensitivity value did not change until the number of samples used for calculation was 16 or more. When the number of samples reached 4096, it was determined as a converged state, and the indices value was determined with the value at this time. The reason that the indices for maximum operable back-pressure converge more quickly seems to be because the distribution of operability values takes a discontinuous value with 0 (inoperable) or 1 (operable), and uncertainty increases owing to this characteristics.

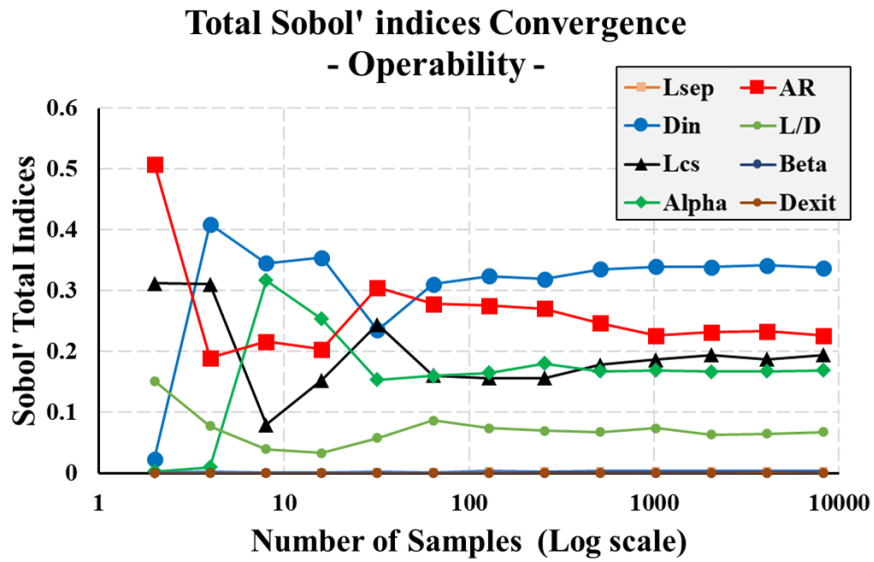


Fig. 67. Convergence history of total Sobol' indices for HWT diffuser operability

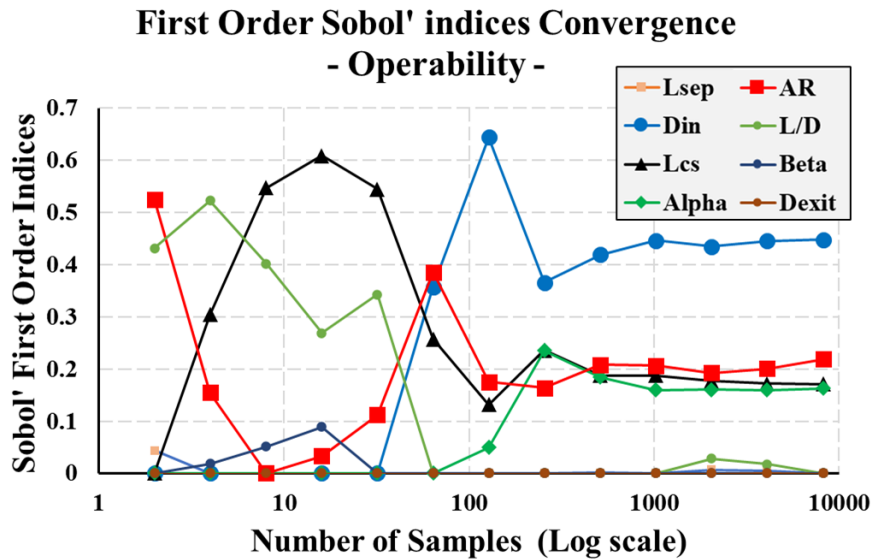


Fig. 68. Convergence history of first order Sobol' indices for HWT diffuser operability

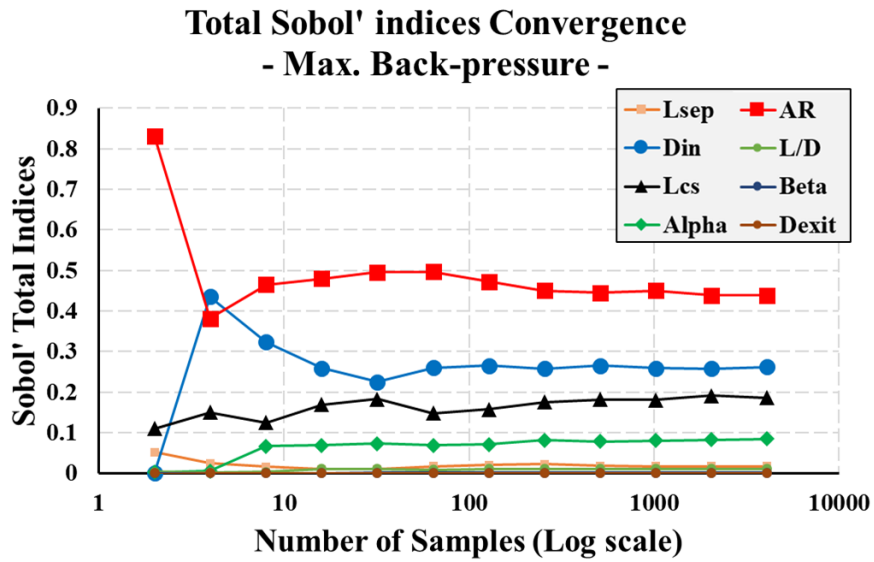


Fig. 69. Convergence history of total Sobol' indices for HWT diffuser maximum operable back-pressure

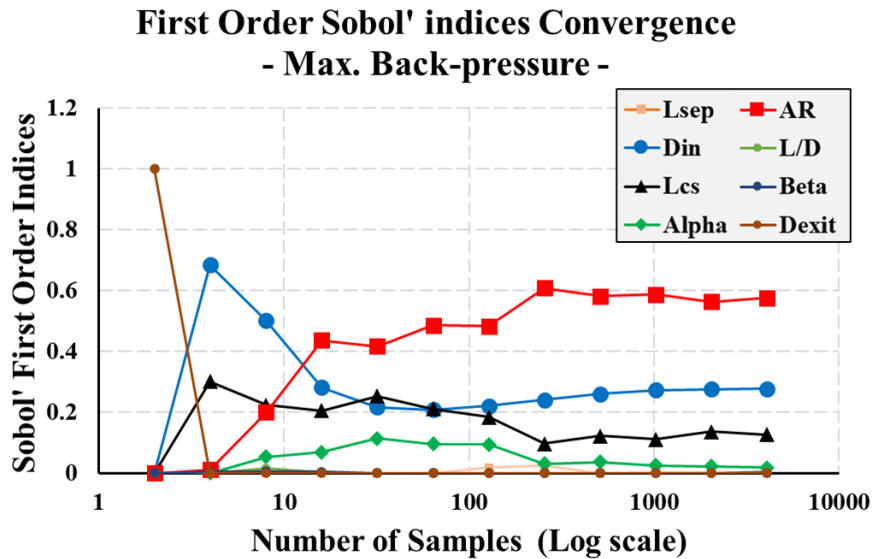


Fig. 70. Convergence history of first order Sobol' indices for HWT diffuser maximum operable back-pressure

8.3. SA for HWT Diffuser Performance

8.3.1. Procedure of SA

To investigate the influence of each design variables (operability and maximum operable back-pressure) on performance variables, at first, the correlation coefficient between each design variable and the performance variable was observed. This value was calculated based on the linear regression theory introduced previous *Section 3.4.2*. The sign of each coefficient shows whether the performance variables varied to same direction or in opposite direction when the design variables change. A positive sign means the same direction, and a negative sign means the opposite direction. The absolute value shows how linear the relationship between the two variables is. Since this value does not explain the magnitude of the influence of the design variable, only values of +1 (positive relationship, linear), -1 (negative relationship, linear), and 0 (no linearity) were meaningfully used.

As mentioned above, since the correlation coefficient is based the linear regression theory, the magnitude of a correlation coefficient does not indicate the magnitude of influence of each design variables on the performance variables. Therefore, the magnitude of influence of each design variables was confirmed by variance based sensitivity indices, where the variance of operability and maximum operable back-pressure were decomposed into each variance contributions of each variable. Here, indices quantify the influence of each design variable on the variance of the performance variables. Therefore, the effect of each design variable on the HWT diffuser performance was comprehensively confirmed by checking the direction based on linear regression and checking the magnitude of the influence through variance based sensitivity indices.

Additionally, the relationship between the maximum operable back-pressure and each design variable was visualized through scatterplots. Through this, the degree of linearity and the degree of dispersion could be qualitatively confirmed.

8.3.2. SA for Operability of HWT Diffuser

The operability of HWT has been considered as a very important issue when designing a diffuser. Fig. 71 shows the linear correlation coefficient between shape design variables and operability. Fig. 72 shows the relative contribution of each design variables to variance of operability. Through the Figs. 71 and 72, it can be confirmed that the effect of each design variable on operability could be identified. In summary, the design variables with the greatest influence were (1) diffuser inlet diameter, (2) diffuser throat area ratio, (3) catch-cylinder length, and (4) diffuser converging angle in that order. The diffuser length had a relatively small effect, and the diffuser diverging angle and diffuser exit diameter had a marginal effect.

The larger the diffuser inlet diameter, D_{in} , the greater the risk of inoperability. This is because the larger the space after the nozzle, the larger the flow expands, which corresponds to a strong shock wave at a high Mach number, rendering a severe total pressure loss.

Next, the larger the throat ratio, AR , the higher the operability. This seems because all the flow ejected from the nozzle could pass through the diffuser throat due to the larger duct size even with significantly lowered total pressure.

Increase in the diffuser converging angle, α , increases the risk of inoperability because a strong shock wave will be generated. This strong shock wave not only causes total pressure loss, but also creates a strong adverse pressure gradient at the inlet of the diffuser, which impedes the flow of the air.

In parametric study based design, the catch-cylinder was introduced to alleviate the strength of the strong shock wave. From sensitivity analysis, the longer the catch-cylinder length, L_{cs} , the better the operability was. However, it was confirmed through the parametric study and the surrogate model that this catch-cylinder should exist at an appropriate location and with an appropriate length, but this trend could not be captured in the sensitivity analysis. This

seems to be a weakness of global sensitivity analysis. Although sensitivity analysis can effectively show the overall sensitivity, it was confirmed that detailed design matters may require the researcher's insight or comprehensive parametric study.

The results of this sensitivity analysis showed trends consistent with the results of the parametric study of the previous chapter. However, it was possible to deal with the diffuser inlet diameter, D_{in} , which could not be dealt with in the parametric study, and it was confirmed that this design variable was highly important for operability. In addition, rather than focusing on a specific point in the design space, trends could be confirmed throughout the design space, and the degree of influence could be quantitatively evaluated.

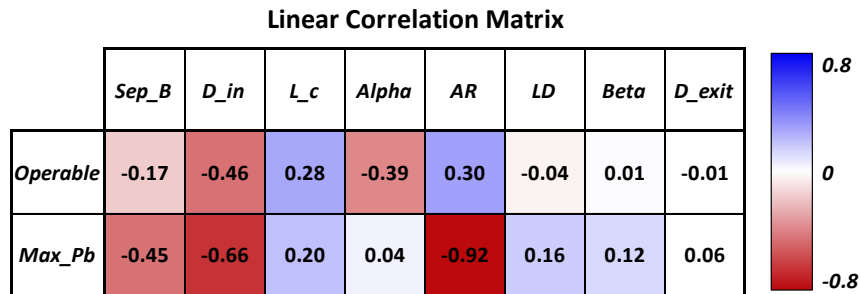


Fig. 71. Correlation coefficient between shape design variables and operability / maximum operable back-pressure

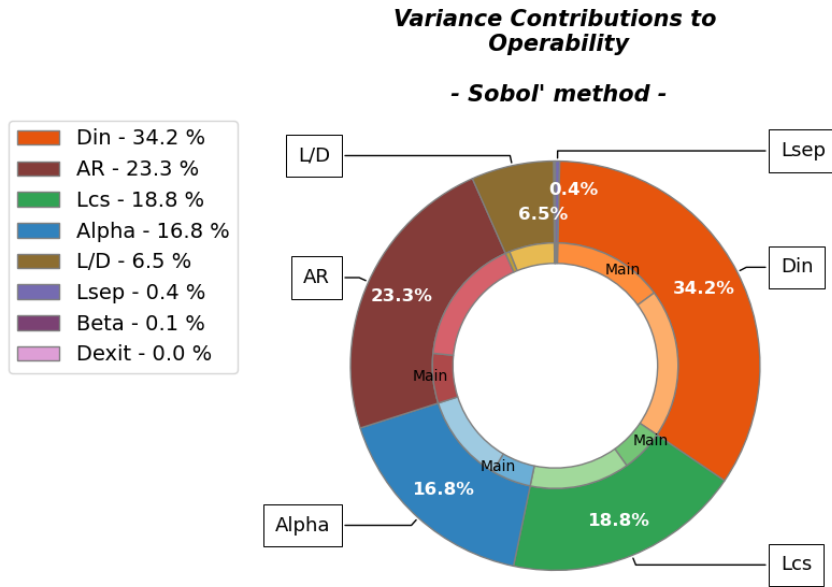


Fig. 72. Relative contribution of each variable on the variance of operability from variance based sensitivity analysis

8.3.3. SA for Efficiency of HWT Diffuser

It is important to improve the efficiency of a HWT diffuser because excessive resources required to generate high pressure ratio usually considered as a critical problem for the construction and operation of HWT. Fig. 73 shows the linear correlation coefficient between shape design variables and maximum operable back-pressure. Fig. 74 shows the relative contribution of each design variables to variance of maximum operable back-pressure. Through the Figs. 73 and 74, it can be confirmed that the effect of each design variable on efficiency could be identified. In summary, the design variables with the greatest influence were (1) diffuser throat area ratio, (2) diffuser inlet diameter, (3) catch-cylinder length, and (4) diffuser converging angle in that order. The diffuser length had a relatively small effect, and the diffuser diverging angle and diffuser exit diameter had a marginal effect.

Overall, the correlation for maximum operable back-pressure shows a mostly inverse trend with the operability of HWT. That is, an efficient diffuser shape can be considered as a configuration of

high risk of inoperability.

The larger the throat ratio, the smaller the maximum operable back-pressure. This was because the large diffuser throat area itself resulted in adverse effect on compression of the flow, and it resulted in strong shock wave at high Mach numbers.

Next, as the diffuser inlet diameter increased, the diffuser efficiency decreased significantly. It was confirmed that reducing the diffuser inlet diameter as much as possible significantly improved not only the operability but also the diffuser efficiency.

The longer the catch-cylinder length, the better the operability was. Because, the catch-cylinder could alleviate the strength of the strong shock wave at the forepart of the diffuser. As the shock wave intensity decreased, the total pressure loss decreased, which had a positive effect on the diffuser efficiency.

Conversely, increase in the diffuser converging angle decreased the efficiency of the diffuser. This is because, as the converging angle increases, the wave angle of the initially generated shock wave increases, resulting in severe total pressure loss.

The results of this sensitivity analysis showed trends consistent with the results of the parametric study of the previous chapter. However, the diffuser inlet diameter, which could not be dealt with in the parametric study, was highly important for diffuser efficiency.

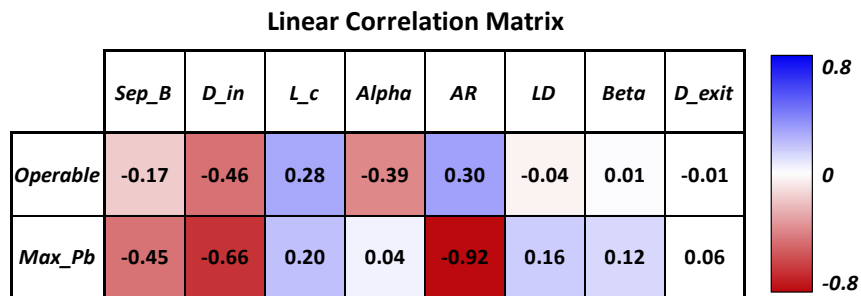


Fig. 73. Correlation coefficient between shape design variables and operability / maximum operable back-pressure (identical figure to Fig. 71)

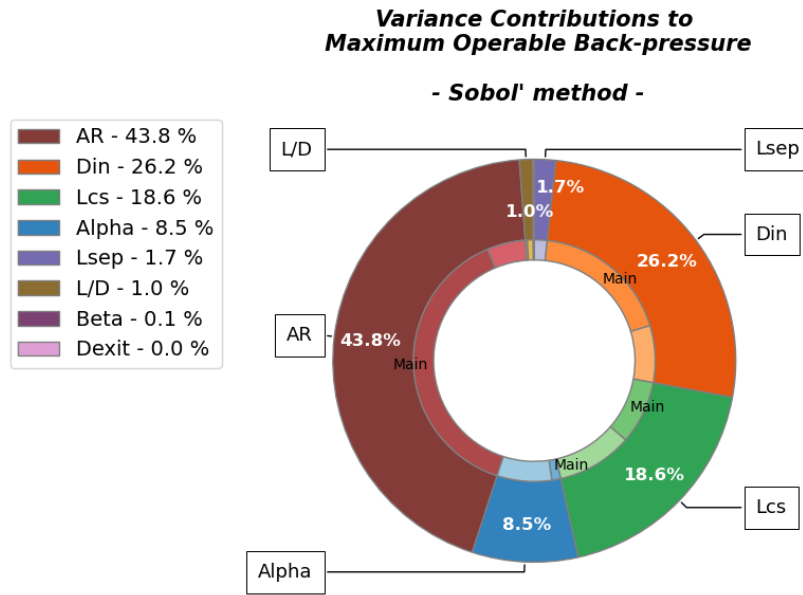


Fig. 74. Relative contribution of each variable on the variance of maximum operable back-pressure from variance based sensitivity analysis

Figs. 75–82 shows the scatterplots between shape design variables and maximum operable back–pressure. Through this, the degree of linearity and the degree of variance were additionally confirmed qualitatively. Except for the throat area ratio, it could not be said to have linear relation. The relationship between the throat area ratio and maximum operable back–pressure was fairly linear with a determination coefficient of 0.85. This seems to be one of the important findings that were difficult to confirm in the parametric study. Based on this linear relation, it would be possible that several flow calculations with the several diffuser throat area can be used to predict diffuser efficiency of various diffuser throat area via linearly interpolation.

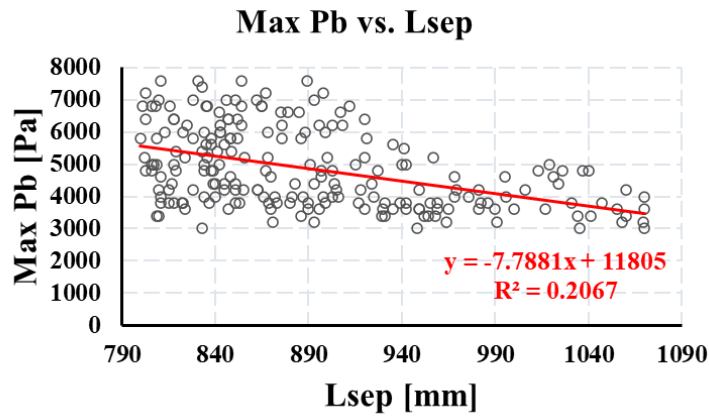


Fig. 75. Scatterplot between separation length and maximum operable back-pressure

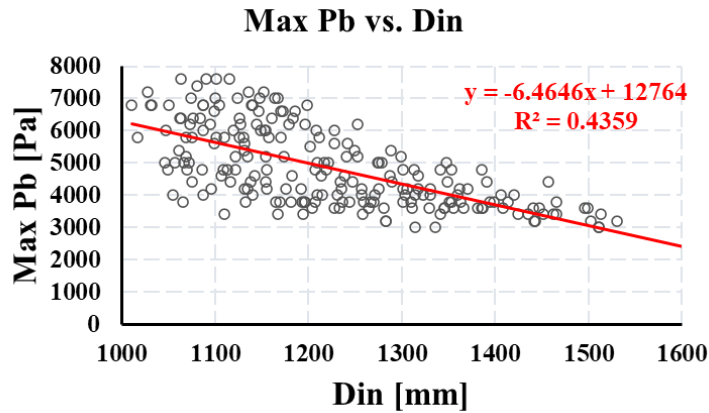


Fig. 76 Scatterplot between inlet diameter and maximum operable back-pressure

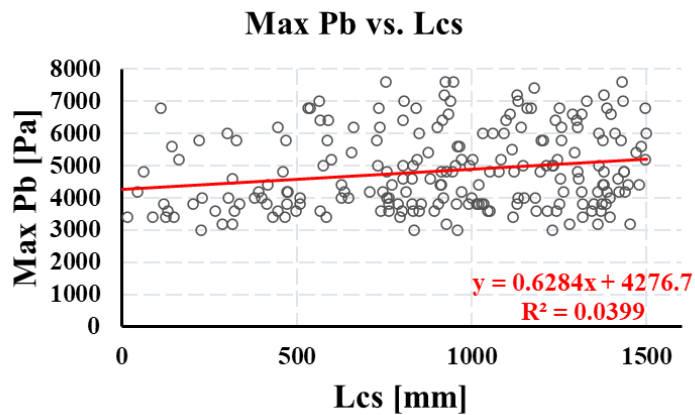


Fig. 77 Scatterplot between catch-cylinder length and maximum operable back-pressure

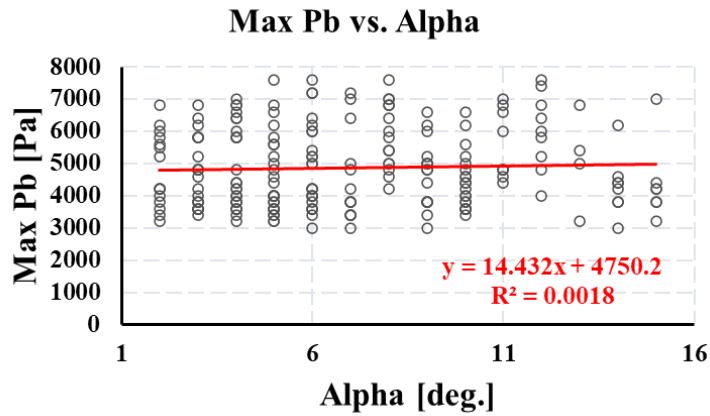


Fig. 78 Scatterplot between converging angle and maximum operable back-pressure

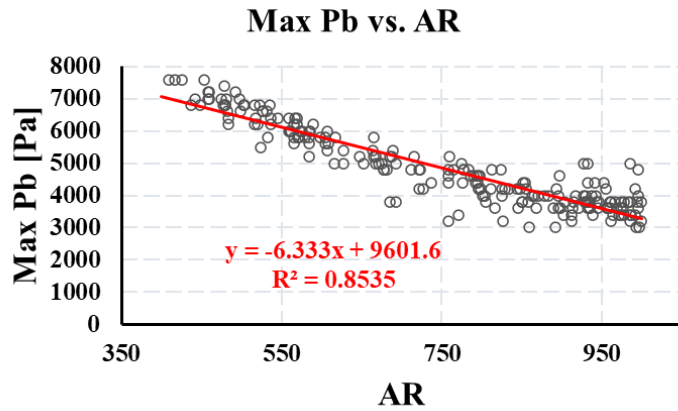


Fig. 79 Scatterplot between throat area ratio and maximum operable back-pressure

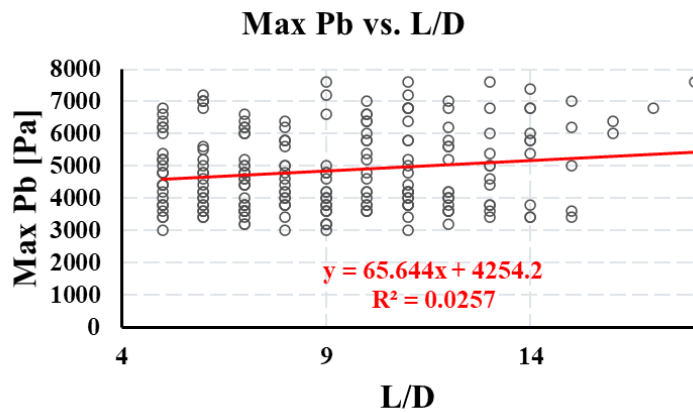


Fig. 80 Scatterplot between the length to diameter ratio of diffuser throat and maximum operable back-pressure

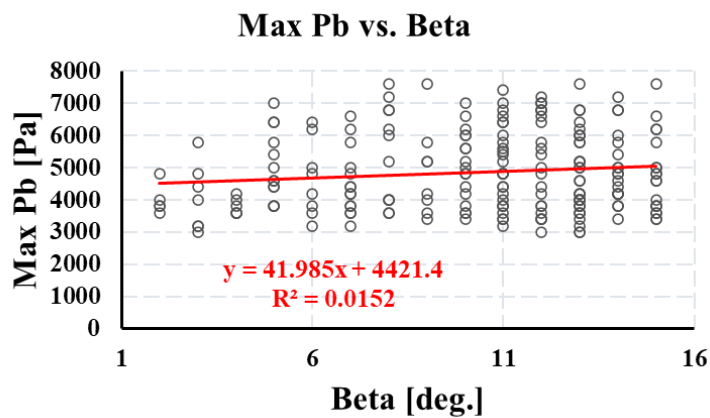


Fig. 81 Scatterplot between diverging angle and maximum operable back-pressure

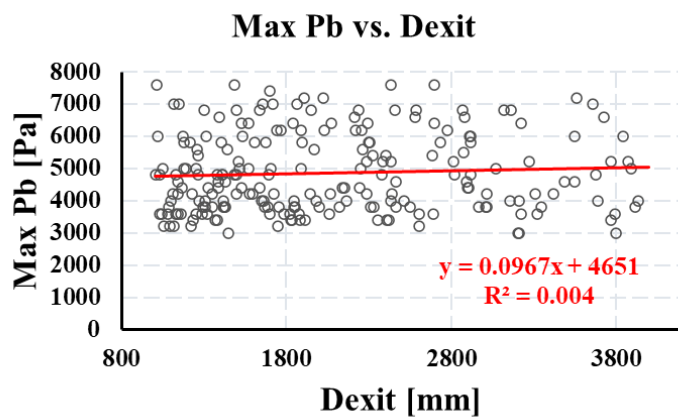


Fig. 82 Scatterplot between exit diameter and maximum operable back-pressure

CHAPTER 9

CONCLUSION

9.1. Summary

This study aimed to design an efficient HWT diffuser that enables HWT testing with the large blockage model with limited resources. The conventional consensus required a larger HWT for the test of the large blockage model, which will cause an exponential increase in cost. Therefore, through comprehensive diffuser design research, it was possible to design the diffuser shape that can test the large blockage model.

For this objectives, the conventional design was not suitable, because the conventional diffuser design has a high risk of deriving an inoperable or highly inefficient diffuser shape. Furthermore, this method relies on the insights or know-how of researchers.

Before design study, the fundamental characteristics of the HWT were analyzed through numerical analysis, and an innovative observation variable useful for effective diffuser design were newly proposed. Efficient HWT diffuser was designed by using a design method that was more sophisticated than the conventional method. The first method was parametric study based design, and the second method was surrogate model based design. The study primarily focused on the operability of diffuser, and reducing total pressure loss, in other words, improving the efficiency of the diffuser. Thereby this study relieved the required pressure ratio and designing the

HWT diffuser for a large-sized model test under restrictive conditions.

In the parametric study based design, a parametric study was performed through numerical analysis for each design variable. The effect of each design variable on the diffuser efficiency was investigated. By repeating these parametric studies, the diffuser shape was adjusted to enable a stable wind tunnel test with higher efficiency, and the efficient diffuser shape that satisfied the requirements was derived.

Surrogate model based design was also conducted to compensate for the weakness of parametric study based design in time and resource consumption, where parametric studies must be repeatedly performed until the design requirements is fulfilled. First, the design framework was established and consists of a LHS based analysis point sampler, an automated flow analysis and diffuser efficiency evaluation module, a kriging surrogate model generation module, and a sensitivity analysis module. The diffuser performance according to the shape of the diffuser can be immediately predicted by the surrogate model, so it can be effectively used for diffuser design and sensitivity analysis without excessive flow analysis. Subsequently, as a further study assuming a more general situation, a diffuser with high efficiency not only in the on-design Mach 7 flow condition but also in the off-design Mach 4.7 flow condition (that is, to cover a wide range of flow condition and achieve high efficiency) was derived.

Through each design method, useful design considerations for designing a HWT diffuser with high performance were derived, and the performance comparison of the diffuser shape derived through each design was performed. Although the design based on the parametric study brought about a 60% increase in the efficiency of the diffuser compared to the baseline design, the design based on surrogate model showed a significant further increase in efficiency. Ultimately, it was a 90% increase in efficiency compared to the baseline shape, and a 20% increase in efficiency even compared to the parametric study based design. Considering that much less time and resources were required to perform the surrogate model based

design than the parametric study based design, the usefulness of the surrogate model based design framework constructed in this study can be confirmed.

This high level of improvements was judged to be the evidence that the conventional design of HWT diffuser has focused on simply sizing rather than optimization. It was confirmed that the design objectives that were previously considered impossible or would cost excessively could be effectively resolved by designing the diffuser appropriately.

9.2. Design Considerations for HWT diffuser design

The design considerations obtained from the study can be summarized as follows.

(1) In order to analyze the diffuser, the mass flow rate weighted average total pressure was proposed as an important observation variable. This observation variable was an important finding that makes it possible to clearly explain the cause of the superiority and inferiority of the efficiency of the various diffuser shapes during design.

(2) Most of the total pressure loss occurred in the hypersonic / supersonic region and terminal shock wave, whereas the total pressure loss in the subsonic region was marginal. Thus, designing the diffuser shape in the hypersonic / supersonic region was highly important to improve the pressure recovery of the diffuser.

(3) high degree of total pressure loss occurred when a large blockage model existed in the wind tunnel. This loss must be considered in the design stage and flow analysis should be performed including the blockage model.

(4) In the diffuser converging section, shock wave generated at a high Mach number resulted in severe total pressure loss. Adjusting the shock wave intensity while changing the convergent angle can help prevent a drastic total pressure loss. Additionally, reducing the shock wave angle by placing a catch-cylinder with a constant-diameter duct at the entrance of the diffuser improved the pressure recovery significantly.

(5) Determination of the appropriate cross-sectional area of the diffuser throat was deemed extremely essential. Based on the characteristics of the flow inside the HWT with a high Mach number and viscous effects along with the influence of the blockage model, the cross-sectional area of the diffuser throat must be appropriately sized. An extremely small diffuser throat area may cause choking in the diffuser throat, whereas an extensively large area can increase the required pressure ratio during wind tunnel operation. Thus, a

trade-off between these two factors must be considered when determining the cross-sectional area of the diffuser throat.

(6) The design space feasibility study showed that the conventional design process that simply refers to an existing shape or uses an empirical formula would be highly risky.

(7) Through the design space exploration study using the surrogate model, it was confirmed that the diffuser inlet diameter was also a highly important variable.

(8) The design variables with the greatest influence on operability were diffuser inlet diameter, diffuser throat area ratio, catch-cylinder length, and diffuser converging angle in that order. And, influence of other variables was marginal.

(9) The design variables with the greatest influence on efficiency were diffuser throat area ratio, diffuser inlet diameter, catch-cylinder length, and diffuser converging angle in that order. And, influence of other variables was marginal.

(10) The relationship between the throat area ratio and maximum operable back-pressure was considered to be a fairly linear. This finding is judged to be highly useful when performance prediction with a small number of simulations is required.

9.3. Limitations and Future Works

The limitations of the study and follow-up studies are described in several items.

► Concerning the Scale of HWT and Massflow Rate

The present study deals with the 13 MW class large scale HWT. However, due to practical reasons such as cost and space required for construction and operation, there would be many cases in which a smaller scale wind tunnel should be constructed. For example, if sufficient space cannot be secured for constructing a HWT, the scale of the HWT will inevitably be reduced. If the resource of generating the mass flow rate of gas is insufficient, by reducing the mass flow rate, it is possible to reduce the required capacity and cost of gas tank, heater, and vacuum facility. Therefore, this section briefly discussed the influence of small scale and low mass flow rate of HWT. It is hoped that this section would help design small-scale HWTs in follow-up studies.

Since the most important similarity variable in HWT is the Mach number, the Mach number is fixed (that is, the nozzle-to-exit area ratio is fixed) and develop the discussion. Mass flow rate is as shown in Eq. (84), and as can be seen from Eq. (88), the reduction of the mass flow rate can be achieved by changing three variables. Assuming that only one variable is changed, the effect of the reduction of the reservoir pressure, the increase of the reservoir temperature, and the nozzle size (i.e., HWT scale) reduction is discussed in the aspects of (1) flow characteristics, (2) air modeling, and (3) wind tunnel construction and operation, respectively.

$$\dot{m} = \rho VA \quad (84)$$

$$\rho = \frac{p}{RT} \quad (85)$$

$$V = M\sqrt{\gamma RT} \quad (86)$$

$$A \propto L^2 \quad (87)$$

$$\dot{m} \propto \sqrt{\frac{\gamma}{R}} M \frac{pL^2}{\sqrt{T}} \quad (88)$$

First, in terms of the flow characteristics, it would be valuable to discuss the change of the Reynolds number, which is a major similarity variable along with the Mach number. The Reynolds number can be expressed in terms of pressure, temperature, and characteristic length as Eq. (89). As can be seen from the equation, when the pressure is lowered rendering a small mass flow rate, the Reynolds number decreases and the viscous effect will be increase. Increasing the temperature also causes a decrease in the Reynolds number, and decreasing the wind tunnel scale also decreases the Reynolds number. Therefore, when the scale or mass flow rate of HWT is lowered, it is judged that it is necessary to confirm whether the increased viscosity effect can greatly change the test result.

$$Re = \frac{\rho VL}{\mu} = \sqrt{\frac{\gamma}{R\mu}} M \frac{pL}{\sqrt{T}} \quad (89)$$

In terms of the energy mode and chemical reaction of air molecules, decreasing pressure to lower the mass flow rate causes the chemical reaction to start at a lower temperature (J. D. Anderson, 2006). This is because the chemical reaction of air molecules at high temperature is a reaction where the number of molecules increases. Next, increasing the temperature to lower the mass flow rate increases the degree of chemical reactions. The size of the wind tunnel does not affect equilibrium state of the air. Therefore, if the mass flow rate is reduced, the effect of chemical reaction should be observed more carefully.

The importance of the nonequilibrium state varies depending on

the magnitude of the flow characteristic time and the chemical reaction characteristic time as shown in the following relations (J. D. Anderson, 2006).

$$\textit{Equilibrium: } \tau_f \gg \tau_c \quad (90)$$

$$\textit{Frozen: } \tau_f \ll \tau_c \quad (91)$$

$$\textit{Nonequilibrium: } \tau_f \approx \tau_c \quad (92)$$

The flow characteristic time, τ_f , is expressed as the ratio of the characteristic length to the flow velocity, and the chemical reaction characteristic time, τ_c , is representative time for chemical reaction to complete. This characteristic time decreases as the pressure and temperature increase. After all, since chemical reactions are caused by collisions between air molecules, it can be confirmed that the nonequilibrium becomes more important as the collisions between molecules slow down. Therefore, the nonequilibrium should be considered carefully when decreasing the mass flow rate. Importance of nonequilibrium will be increase when the pressure is sufficiently reduced and the scale of HWT is sufficiently decreased. Conversely, increased temperature makes the nonequilibrium important.

Finally, in the aspect of construction and operation of the wind tunnel, it is theoretically possible to reduce the required capacity of the air tank, vacuum tank, heater and dehumidifier by reducing the mass flow rate. This can be effective in terms of cost. However, in practice, it is judged that this approach is not accessible. Because the mass flow rate can be lowered by decreasing the pressure with the size and temperature of HWT fixed, but in this case, required back-pressure should be lowered rendering increased cost. It seems that the cost of lowering the back-pressure would be greater than the reduced cost by lowering the mass flow rate. Therefore, it seems that the general choice is to operate more economically at higher back-pressure without decreasing mass flow rate. Similarly, increasing temperature can decrease mass flow rate. However, since

the cost of increasing temperature is generally greater, it seems that the general choice is to operate more economically at lower temperature without decreasing mass flow rate.

The above discussion can also be confirmed through the reservoir and nozzle exit flow conditions of NASA Langley AHSTF in Table 23. It is noted that the various Mach number flow conditions have inflow temperature constantly controlled at the level of 220 K. This temperature seems to be sufficient to prevent condensation when the flow expands to higher Mach number in HWT. Practically, dehumidification of air has limited level. The maximum specifications of dehumidifiers are distributed to the extent of making the dew point of air at the level of -80 degrees Celsius. In addition, since increasing the air temperature will incur a relatively large cost, it seems that the temperature has been preferentially set to the minimum level at which condensation will not occur. Conversely, the mass flow rate is distributed over a rather wide range in Table 23. Therefore, in HWT, since the priority is to meet restrictive conditions such as the prevention of condensation or vacuum level achievement, mass flow rate seems to be determined as a dependent variable.

Table 23. Reservoir and nozzle exit flow conditions of NASA Langley AHSTF according to inflow Mach number (including mass flow rate)

	Reservoir		Nozzle			
Mach Number	P_0 [atm]	T_0 [K]	A^* [m ²]	\dot{m} [kg/s]	P_{n_e} [Pa]	T_{n_e} [K]
4.7	13.6	1,123	0.003	4.99	3,249	224
5.0	13.1	1,251	0.003	4.54	2,148	226
5.5	11.2	1,468	0.003	3.58	1,012	226
6.0	35.1	1,655	0.00083	2.91	1,811	220
7.0	28.6	2,216	0.00083	2.05	531	224
8.0	23.0	2,879	0.00083	1.43	171	228

Downscaling a HWT has the advantage of considerably reducing HWT construction and operating costs, as described in *Section 1.2.1*. However, as the HWT becomes smaller, it basically deviates from

the Reynolds number similarity more and increases the relative magnitude of measurement noise compared to the flow properties, thereby increasing the measurement error. In addition, in terms of test model, the difficulty of manufacturing the test model is increased because the size of the model must be downscaled considering blockage ratio and test section size.

In summary, the discussions in this section deal with changes in Reynolds number, equilibrium chemical reactions, nonequilibrium, required specifications of HWT components in a qualitative point of view. Therefore, it is judged that additional research would be necessary to quantitatively analyze how much the change of mass flow rate and scale affects each aspect, and whether the influence should be considered or not.

► Transient Characteristics in Starting Process

This study focused on confirming the operability of HWT and the maximum operable back-pressure that can be operated after the starting state. Additionally, the unsteady characteristics and transient starting procedure were briefly covered in *Sections 4.5.2~4.5.3*, but as a further study, it would be meaningful to conduct more research on the transient characteristics in starting process and the operational strategy for efficient and stable starting.

As mentioned in *Section 4.5.2*, it is known that the characteristic time of the back-pressure change will be several orders of magnitude larger than the characteristic flow time, so, the time-dependent starting procedures can be investigated based on the combination of steady calculations (Savino et al., 1999). In other words, the present study was conducted under the assumption that the flow change due to the transient change in back-pressure could be predicted identically by replacing it with a series of steady analyses.

However, the referenced literature does not provide detailed data on the difference between the unsteady calculation and the combination of steady calculations. And, it does not provide a detailed

condition or range where this assumption is valid. Therefore, it is also valuable to investigate the validity of this assumption by performing unsteady analysis and comparing it with a combination of steady-state analysis results.

In the starting procedure of a HWT, unsteady characteristics prevails. As the pressure ratio becomes increased before starting, the shock wave initially generated from the nozzle throat will move downstream and be swallowed into the diffuser throat, resulting in wind tunnel starting. In this transient process, a higher pressure ratio is required than in the operational steady state because the shock wave should be swallowed to the diffuser. This initial shock system is not similar to series of oblique shocks in operational state, and is close to the normal shock wave rendering severe total pressure loss. Therefore, it is judged that it is appropriate to distinguish the pressure ratio required for operation (after starting state) from the pressure ratio required for initially starting. More successful design will be possible if the pressure ratio required for starting is simultaneously considered in the design.

The starting pressure ratio is expected to be affected by the shape of the diffuser, and the initial flow conditions inside the HWT before starting (whether to start at a relatively high pressure in a duct or after making the duct pressure close to a vacuum). Additionally, the back-pressure control strategy (the lowering speed of back-pressure, the level of lowering back-pressure, etc.) could make difference. It is judged that it would be valuable to analyze these aspects and refer to them for design or operation strategy of HWT.

► Hot Wind Tunnel Design

The conditions of this study belong to the cold wind tunnel among the categories of HWT. Here, since the temperature was distributed at a maximum of about 2,500 K, the flow analysis was carried out assuming that the air was in an equilibrium state. However, in order to design all kinds of HWT diffusers including hot wind tunnels, it is

necessary to accurately analyze even higher temperature air. In these temperature distributions, other major effects not covered in the study, such as vibrational and chemical non-equilibrium, might appear.

► Flow Analysis of Higher Fidelity and Lower Fidelity

In this study, flow analysis was performed under the assumption of axis-symmetry. However, in a real environment, it is highly likely that the flow is not axisymmetric due to the non-symmetric model support and noise from various sources. Since the performance of the diffuser could vary depending on the structure of the shock wave formed inside the diffuser duct, if the symmetry is not assured, the performance may be different. To the best of author's knowledge, research on whether this symmetry is a factor that increases the diffuser performance has not been conducted until now. Therefore, it is judged that subsequent studies will also be valuable to evaluate these effects through 3D analysis. On the contrary, it is judged that it would be valuable to increase the efficiency of diffuser design through a study on a simplified model for more efficient and faster analysis of HWT such as a 1D analysis model.

► Extension of the Design Framework

It was confirmed that the design framework developed in this study was a quite valuable tool in designing the HWT Diffuser. It is expected that this framework will be effective in solving design problems in similar applications, and if only the flow analysis and grid generation modules are adjusted to the application, it is judged to be expandable to various applications.

BIBLIOGRAPHY

- Agostinelli, P. W., Trifoni, E., & Savino, R. (2019). Aerothermodynamic analyses and redesign of GHIBLI Plasma Wind Tunnel hypersonic diffuser. *Aerospace Science and Technology*, 87, 218–229. <https://doi.org/10.1016/j.ast.2019.02.023>
- Agostinelli, P. W., Turchi, A., le Quang, D., Masutti, D., Vigeveno, L., D'ambrosio, D., & Chazot, O. (2020). Investigation of hypersonic flow in the vki h3 wind tunnel: From facility characterization to boundary-layer interaction over low-temperature ablators. *23rd AIAA International Space Planes and Hypersonic Systems and Technologies Conference, 2020*. <https://doi.org/10.2514/6.2020-2445>
- Anderson, J. (2011). *Fundamentals of Aerodynamics*. McGraw hill.
- Anderson, J. D. (2006). *Hypersonic and High Temperature Gas Dynamics (AIAA Education)* (2nd Editio). American Institute of Aeronautics and Astronautics Inc, AIAA.
- Austin, R. F. (1966). *AN OPEN-JET WIND TUNNEL INVESTIGATION OF A FIXED-GEOMETRY DIFFUSER SYSTEM AT MACH NUMBERS 3.6 AND 7.0*.
- Borrelli, R., & Martucci, A. (2011). SCIROCCO Plasma Wind Tunnel: Synergy between Numerical and Experimental Activities for Tests on Aerospace Structures. *Wind Tunnels and Experimental Fluid Dynamics Research*. <https://doi.org/10.5772/21125>
- Brune, A. J., Hosder, S., Campbell, D., Gulli, S., & Maddalena, L. (2019). Numerical analysis of an actively cooled low-reynolds-number hypersonic diffuser. *Journal of Thermophysics and Heat Transfer*, 33(1), 32–48. <https://doi.org/10.2514/1.T5437>
- Büscher, M., Esser, B., Kindler, K., & List, V. (1995). Developments at the arc heated facility LBK of DLR. *Aerothermodynamics for Space Vehicles*, 367, 357.

- Choi, D., Baek, J. S., & Kim, K. H. (2021). Efficient diffuser design for plasma wind tunnels with a large blockage model. *Aerospace Science and Technology*, 119, 107206. <https://doi.org/10.1016/j.ast.2021.107206>
- Czysz, P. A. (1963). Correlation of wind tunnel blockage data. In *TECHNICAL DOCUMENTARY REPORT*. <https://doi.org/10.1007/BF00731082>
- Gardi, R., Vecchio, A. del, Marino, G., & Russo, G. (2011). Cira activities on UHTC 's: On-ground and in flight experimentations. *17th AIAA International Space Planes and Hypersonic Systems and Technologies Conference 2011, April*, 1–17. <https://doi.org/10.2514/6.2011-2303>
- Golberg, D. E. (1989). Genetic algorithms in search, optimization, and machine learning. *Addion Wesley*, 1989(102), 36.
- Gonzales, J., Suzuki, K., & Sakaue, H. (2021). Novel optical heating rate measurement in hypersonic flow using phenol formaldehyde luminescence. *Aerospace Science and Technology*, 115. <https://doi.org/10.1016/j.ast.2021.106837>
- Gupta, R. N., Lee, K.-P., Thompson, R. A., & Yos, J. M. (1991). Calculations and Curve Fits of Thermodynamic and Transport Properties for Equilibrium Air to 30000K. In *NASA Reference Publication 1260*.
- HANUS, G., MIKKELSEN, K., OLSTAD, S., & CARISTIA, S. (1991). Supersonic wind tunnel diffuser performance with high model blockageat moderate to low Reynolds numbers. *AIAA 27th Joint Propul. Conf.* <https://doi.org/10.2514/6.1991-2274>
- Hastings, W. K. (1970). Monte carlo sampling methods using Markov chains and their applications. *Biometrika*, 57(1), 97–109. <https://doi.org/10.1093/biomet/57.1.97>
- Heinrich, H. G., Hess, S. R., & Stumbris, G. (1964). Drag Coefficients of Several Bodies of Revolution At Transonic and Supersonic Velocity. *Asd-Tdr-63-663, September*, 53.
- I.M. Sobol. (2001). Global sensitivity indices for nonlinear mathematical models and their Monte Carlo estimates. *Mathematics and Computers in Simulation*, 55(103), 271–280. [https://doi.org/https://doi.org/10.1016/S0378-4754\(00\)00270-6](https://doi.org/https://doi.org/10.1016/S0378-4754(00)00270-6)
- Jones, W. P., & Launder, B. E. (1972). The prediction of

- laminarization with a two-equation model of turbulence. *International Journal of Heat and Mass Transfer*, 15(2), 301–314. [https://doi.org/10.1016/0017-9310\(72\)90076-2](https://doi.org/10.1016/0017-9310(72)90076-2)
- Kim, K. H., Kim, C., & Rho, O. H. (2001). Methods for the accurate computations of hypersonic flows. I. AUSMPW+ scheme. *Journal of Computational Physics*, 174(1), 38–80. <https://doi.org/10.1006/jcph.2001.6873>
- Kim, M., Lee, M., Kim, J.-S., Choi, C., Seo, J., Moon, S., & Hong, B. (2013). 0.4 MW 급 분절형 아크 히터를 이용한 초음속 플라즈마 풍동 특성 실험. *J. of The Korean Society for Aeronautical and Space Sciences*, 41(9), 700–707.
- Krige, D. G. (1951). A statistical approach to some basic mine valuation problems on the Witwatersrand, by D.G. Krige, published in the Journal, December 1951: introduction by the author. *Journal of The South African Institute of Mining and Metallurgy*, 52, 201–203.
- Ku, K., & Jeong, S. (2018). Building electric energy prediction modeling for BEMS using easily obtainable weather factors with Kriging model and data mining. *Building Simulation*, 11(4), 739–751. <https://doi.org/10.1007/s12273-018-0440-1>
- Lu, C., Feng, Y. W., Liem, R. P., & Fei, C. W. (2018). Improved Kriging with extremum response surface method for structural dynamic reliability and sensitivity analyses. *Aerospace Science and Technology*, 76, 164–175. <https://doi.org/10.1016/j.ast.2018.02.012>
- Madsen, J. I., Shyy, W., & Haftka, R. T. (2000). Response surface techniques for diffuser shape optimization. *AIAA Journal*, 38(9), 1512–1518. <https://doi.org/10.2514/2.1160>
- McKay, M. D., Beckman, R. J., & Conover, W. J. (2000). A comparison of three methods for selecting values of input variables in the analysis of output from a computer code. *Technometrics*, 42(1), 55–61. <https://doi.org/10.1080/00401706.2000.10485979>
- Model, M., & Calibration, B. (2021). *Meta Model Based Calibration and Sensitivity Studies of Computational Fluid Dynamics Simulation of Jet Pumps*. 1–11.
- Monnerie, B. (1967). Study of a family of diffusers for a low-Reynolds-number hypersonic wind tunnel. In *LA RECHERCHE AEROSPATIALE: Vol. NASA-TTF-* (Issue April 1967).

- Montgomery, D. C., Peck, E. A., & Vining, G. G. (2021). *Introduction to linear regression analysis*. John Wiley & Sons.
- Monti, R., Paterna, D., Savino, R., & Esposito, A. (2001). Low-Reynolds number supersonic diffuser for a plasma-heated wind tunnel. *Int. J. Therm. Sci*, *40*, 804–815.
- Noh, S., & Kim, K. H. (2019). Estimation of tungsten ablation test conditions using 150 kilowatt arc heater. *Journal of Thermophysics and Heat Transfer*, *33*(4), 1096–1111. <https://doi.org/10.2514/1.T5693>
- Pope, A., & Goin, K. L. (1965). *High-Speed Wind Tunnel Testing*. John Wiley & Sons.
- Purpura, C., Filippis, F. de, Graps, E., Trifoni, E., & Savino, R. (2007). The GIBLI plasma wind tunnel: Description of the new CIRA-PWT facility. *Acta Astronautica*, *61*(1–6), 331–340. <https://doi.org/10.1016/j.actaastro.2007.01.046>
- Rabadan Santana, E., & Weigand, B. (2021). Effect of the reaction mechanism on the numerical prediction of the performance of a scramjet combustor at cruise flight 8 Mach number. *Aerospace Science and Technology*, *112*. <https://doi.org/10.1016/j.ast.2021.106595>
- Raul, V., & Leifsson, L. (2021). Surrogate-based aerodynamic shape optimization for delaying airfoil dynamic stall using Kriging regression and infill criteria. *Aerospace Science and Technology*, *111*, 106555. <https://doi.org/10.1016/j.ast.2021.106555>
- Riehmer, J. C., Gülhan, A., Santana, E. R., & Weigand, B. (2014). Experimental and numerical investigations of a scramjet model tested in the H2K blow down wind tunnel at Mach 7. *AIAA AVIATION 2014 –19th AIAA International Space Planes and Hypersonic Systems and Technologies Conference*, June. <https://doi.org/10.2514/6.2014-2933>
- R.S Pugazenthi, & Andy C. McIntosh. (2011). *Design and Performance Analysis of a Supersonic Diffuser for Plasma Wind Tunnel*. <https://doi.org/doi.org/10.5281/zenodo.1330939>
- Saccone, G., Gardi, R., Alfano, D., Ferrigno, A., & del Vecchio, A. (2016). Laboratory, on-ground and in-flight investigation of ultra high temperature ceramic composite materials. *Aerospace Science and Technology*, *58*, 490–497. <https://doi.org/10.1016/j.ast.2016.09.004>

- Saltelli, A., Annoni, P., Azzini, I., Campolongo, F., Ratto, M., & Tarantola, S. (2010). Variance based sensitivity analysis of model output. Design and estimator for the total sensitivity index. *Computer Physics Communications*, 181(2), 259–270. <https://doi.org/10.1016/j.cpc.2009.09.018>
- Saravanan, R., Desikan, S. L. N., Francise, K. J., & Kalimuthu, R. (2021). Experimental investigation of start/unstart process during hypersonic intake at Mach 6 and its control. *Aerospace Science and Technology*, 113, 106688. <https://doi.org/10.1016/j.ast.2021.106688>
- Savino, R., Monti, R., & Esposito, A. (1999). Behaviour of hypersonic wind tunnels diffusers at low Reynolds nwaabers. *Aerospace Science and Technology*, 1, 11–19.
- Shams, T. A., Shah, S. I. A., & Ahmad, M. A. (2020). Capability Analysis of Global Hypersonic Wind Tunnel Facilities for Aerothermodynamic Investigations. *Proceedings of 2020 17th International Bhurban Conference on Applied Sciences and Technology, IBCAST 2020*, 481–501. <https://doi.org/10.1109/IBCAST47879.2020.9044523>
- Sol Baek, J., Choi, D., & Kim, K.–H. (2022). Numerical Investigation of Diffusers in Arc–Heated Wind Tunnel: Introducing a Novel and Efficient Hypersonic Diffuser. *Journal of Aerospace Engineering*, 35(5), 1–16. [https://doi.org/10.1061/\(asce\)as.1943-5525.0001469](https://doi.org/10.1061/(asce)as.1943-5525.0001469)
- Solomon, J. M. (2021). *The Design, Calibration, and Commissioning of a Benchmark Hypersonic Wind Tunnel* [Doctoral dissertation]. The University of North Carolina.
- Song, X., Zhang, J., Zhan, C., Xuan, Y., Ye, M., & Xu, C. (2015). Global sensitivity analysis in hydrological modeling: Review of concepts, methods, theoretical framework, and applications. *Journal of Hydrology*, 523(225), 739–757. <https://doi.org/10.1016/j.jhydrol.2015.02.013>
- Srinivasan, S., Tannehill, J. C., & Weilmuenster, K. J. (1181). *NASA Reference Simplified Curve Fits for the Thermodynamic Properties of Equilibrium Air*.
- Stein, M. (1987). Large sample properties of simulations using latin hypercube sampling. *Technometrics*, 29(2), 143–151. <https://doi.org/10.1080/00401706.1987.10488205>

- Sutherland, W. (1893). LII. The viscosity of gases and molecular force . *The London, Edinburgh, and Dublin Philosophical Magazine and Journal of Science*, 36(223), 507–531. <https://doi.org/10.1080/14786449308620508>
- Sweby, P. K. (1984). High Resolution Schemes Using Flux Limiters for Hyperbolic Conservation Laws. *SIAM Journal on Numerical Analysis*, 21(5), 995–1011. <https://doi.org/10.1137/0721062>
- van Griensven, A., Meixner, T., Grunwald, S., Bishop, T., Diluzio, M., & Srinivasan, R. (2006). A global sensitivity analysis tool for the parameters of multi-variable catchment models. *Journal of Hydrology*, 324(1–4), 10–23. <https://doi.org/10.1016/j.jhydrol.2005.09.008>
- Waltrup, P. J., & Billig, F. S. (1973). Structure of Shock Waves in Cylindrical Ducts. *AIAA Journal*, 11(10), 1404–1408. <https://doi.org/10.2514/3.50600>
- Wegener, P. P., & Lobb, R. K. (1953). An Experimental Study of a Hypersonic Wind-Tunnel Diffuser. *Journal of the Aeronautical Sciences*, 20(2), 105–110. <https://doi.org/10.2514/8.2549>
- Witte, D. W., Irby, R. G., Auslender, A. H., & Rock, K. E. (2004). *1998 Calibration of the Mach 4.7 and Mach 6 Arc-Heated Scramjet Test Facility Nozzles*. <http://www.sti.nasa.gov>
- Yang, J., Zhang, Y., Chen, H., & Fu, S. (2020). Flow separation control in a conical diffuser with a Karman-vortex generator. *Aerospace Science and Technology*, 106. <https://doi.org/10.1016/j.ast.2020.106076>
- Yoon, S., & Jameson, A. (1988). Lower-upper symmetric-gauss-seidel method for the euler and navier-stokes equations. *AIAA Journal*, 26(9), 1025–1026. <https://doi.org/10.2514/3.10007>

국문 초록

극초음속 및 고엔탈피 환경을 지상에서 모사하는 시험장치인 극초음속풍동 운용 시에는, 극초음속 영역에서의 과도한 전압력 손실로 인해 풍동 전후로 매우 높은 압력비가 요구된다. 따라서, 극초음속 유동을 효율적으로 압축하여 이러한 전압력 손실을 최소화하고 운용에 요구되는 높은 압력비를 완화시킬 수 있는, 즉 높은 효율을 가지는 디퓨저 설계가 매우 중요하다고 할 수 있다.

하지만, 극초음속풍동 디퓨저의 설계에 대한 연구는 충분히 이루어졌다고 보기 힘들며, 연구 내용에 대한 공개도 보안상의 이유로 제한적으로 이루어진다. 기존의 디퓨저 설계 방법론 역시도 지나치게 간략화 된 분석이나 경험 법칙에 의존하며, 실제 디퓨저 설계 시에는 단순히 기존 디퓨저 형상을 참조하거나 설계자의 노하우에 크게 의존하는 경우가 대부분이다. 이렇게 도출된 극초음속풍동 디퓨저는 운용 불가하거나 운용이 가능하더라도 매우 낮은 효율을 보일 위험이 매우 높다고 할 수 있다.

본 연구의 설계 목표는 한정된 자원으로, 높은 폐색율을 가지는 모델의 풍동 시험을 가능하게 하는 극초음속풍동 디퓨저를 설계하는데 있었다. 기존의 방식은 큰 크기의 모델 시험을 위해서는 그에 상응하는 대형 극초음속풍동을 구축하는 것이었으나, 이러한 방식은 풍동의 구축 및 운용 비용을 기하급수적으로 증가시킨다는 문제가 있었다. 따라서, 심도 깊은 설계 연구를 통해 풍동의 크기를 증가시키지 않고도 큰 크기의 모델 시험이 가능한 디퓨저를 설계하였다. 게다가 디퓨저 효율을 극대화하여 극초음속풍동 구축 및 운용 비용을 최소화하였다.

본 연구에서는 기존의 비효율적이고 위험성이 높은 설계 방법보다 발전된 형태의 설계 방법을 활용하여, 정교하고 효율적인 극초음속풍동 디퓨저의 설계를 수행하였다. 먼저 극초음속풍동에 대한 주요 특성을 수치해석을 통해 분석하였고, 이를 통해 효과적인 디퓨저 설계에 도움이 되는 혁신적인 관찰 값을 제시하였다. 이후 파라메트릭 스터디 기반의 설계 연구를 수행하였는데, 각 설계 변수가 디퓨저 효율에 미치는 영향을 분석하고, 큰 폐색율을 가지는 시험모델이 존재하는 조건에서도

성공적으로 시험이 가능한 극초음속풍동 디퓨저를 설계하였다.

하지만, 파라메트릭 스터디 기반의 설계 방법은 설계 요구조건을 충족할 때까지 반복적으로 파라메트릭 스터디를 수행해야하기 때문에, 시간과 자원 소요 차원에서 효율적이라고 보기 힘들다. 따라서, 이를 보완하기 위해, 대체 모델 기반의 설계 연구를 수행하였다. 먼저 디퓨저 설계 공간을 체계적이고 효율적으로 분석할 수 있는 프레임워크를 구축하였다. 프레임워크는 실험계획법 기반 해석점 샘플러, 자동화된 유동 해석 및 디퓨저 효율성 평가 모듈, 크리깅 대체 모델 생성 모듈, 민감도 분석 모듈로 구성된다. 구축된 프레임워크를 기반으로 대체 모델 중 하나인 크리깅 모델을 생성하고, 극초음속 풍동 디퓨저의 전체 설계 공간을 민감도 분석을 통해 정량적으로 분석하였다.

대체모델을 이용해서 파라메트릭 기반의 설계 방법보다 높은 효율을 가지는 극초음속풍동의 디퓨저 형상을 효과적으로 도출할 수 있었다. 추가로, 실제 풍동은 넓은 운용범위를 가진다는 것을 반영하였다. 온-디자인 조건인 마하 7 유동조건과 오프-디자인 조건인 마하수 4.7을 동시에 고려하여, 넓은 범위의 유동 조건에서도 높은 효율로 시험이 가능한 디퓨저 형상을 도출하였다.

마지막으로, 이러한 설계연구를 통해 도출된 극초음속풍동 디퓨저 설계 시 주요하게 고려해야 하는 사항을 제시하였다. 본 연구의 온-디자인 유동 조건은 저기조 전압력 28.6 bar, 전온도 2,216 K이며, 마하 7 노즐을 통해 2 kg/s의 극초음속유동을 생성하는 조건이다. 이는 13 MW급 이상의 대용량 극초음속 풍동에 준하는 조건이다. 극초음속풍동 디퓨저 관련 연구가 제한적인 환경에서 본 연구가 디퓨저 설계 시 유용한 자료가 되기를 기대한다.

키워드: 극초음속 풍동, 디퓨저, 설계, 전산 유체 역학, 대체 모델, 민감도 분석

학번: 2017-36984

성명: 최대산